

Determination of the strong coupling constant from multi-jet production with the ATLAS detector

Marc-André Dufour

Doctor of Philosophy

Physics Department

McGill University

Montréal, Québec

2012-02-07

Presented to the Faculties of McGill University in Partial Fulfillment of the Requirements for the Degree of Doctor of Philosophy

Copyright 2012
All rights reserved

DEDICATION

To my brother Bruno, thanks for opening the way and never leaving me behind.

ACKNOWLEDGEMENTS

Foremost, I would like to express my deep and sincere gratitude to my supervisor Dr. Brigitte Vachon for all the help she has given me over the years, be it answering physics questions, harassing McGill administration on my behalf, clearing pucks from my crease, writing code, keeping me on track to graduate, or just having a friendly chat. I am forever indebted to her for giving me the opportunity to participate in what has been one of the greatest adventures of my life.

I would like to thank Dr. Malachi Schram for his encouragements, insightful comments, hard questions, and all the coffee breaks and Thomson House lunches. I also thank Dr. Bilge Demirköz for all the help, discussions, and continuous support.

Special thanks to Gabe, Sarah, Eddie, Louise, Frank, and all the others at CERN who helped me feel at home in a distant land. I also thank Gojko, who has been more than a friend throughout my undergraduate and graduate studies. I thank him for all the notes, explanations, support, sleepless nights doing assignments on the phone, but most of all, for his enduring friendship.

Last but not least, I would also like to thank my wife and family for their relentless and unconditional support. This work would simply not have been possible without them.

ABSTRACT

The strong coupling constant α_S is measured in proton-proton collisions at a centre-of-mass energy of 7 TeV using 38 pb⁻¹ of data recorded by the ATLAS detector. An inclusive jet production ratio distribution is used to reduce parton distribution functions dependence and measure the coupling strength at energy scales between 100 GeV and 1.5 TeV. The value of the strong coupling constant $\alpha_S(M_Z)$ is measured to be $0.111^{+0.016}_{-0.012}$, in agreement with similar measurements performed at hadron colliders and the world average value. Results are also consistent with the running of the coupling as predicted by Quantum Chromodynamics, tested for the first time at energy scales greater than 209 GeV.

ABRÉGÉ

La constante de couplage des interactions fortes est mesurée à partir de collisions protons-protons effectuées à une énergie de centre de masse de 7 TeV et enregistrées par le détecteur ATLAS. Un rapport de probabilité de production inclusive de jets est utilisé afin de mesurer la valeur du couplage à différentes énergies allant de 100 GeV à 1.5 TeV, tout en minimisant l'impact des densités de partons. La valeur de la constante de couplage ($\alpha_S(M_Z)$) mesurée est de $0.111_{-0.012}^{+0.016}$, en accord avec les résultats obtenus par des expériences similaires, ainsi qu'avec la moyenne mondiale. Ces résultats sont également compatibles avec l'évolution de la constante de couplage, telle que prédite par la chromodynamique quantique. Ces prédictions de variations sont testées pour la première fois à des échelles d'énergies supérieures à 209 GeV.

TABLE OF CONTENTS

DEDICATION		ii
ACKNOWLEDGEMENTS		iii
ABSTRACT		iv
ABRÉGÉ		v
LIST OF TABLES		viii
LIST OF FIGURES		ix
1	Introduction	1
	1.1 Theory Overview	2
	1.2 Analysis Overview	4
2	Theoretical Foundations	7
	2.1 Theory of Strong Interactions	7
	2.1.1 Colour Confinement	8
	2.1.2 Asymptotic Freedom	9
	2.1.3 Running of the Strong Coupling Constant	9
	2.2 Hard Scattering Processes in Hadron Collisions	10
	2.2.1 Hard Scattering of Partons	10
	2.2.2 Hadron Collisions	14
	2.2.3 Particle Jets	16
	2.3 Observable for the Determination of α_S	18
3	The ATLAS Experiment at the Large Hadron Collider	21
	3.1 LHC Overview	22
	3.2 ATLAS Detector Overview	23
	3.2.1 Nomenclature	24
	3.2.2 Tracking System	26
	3.2.3 Muon Spectrometer	29
	3.2.4 Trigger	32
	3.3 ATLAS Calorimeter System	34
	3.3.1 Basic Concepts of Calorimetry	34
	3.3.2 ATLAS Physics Requirements	36
	3.3.3 ATLAS Calorimeter Details	36

4	Event Simulation and Reconstruction	40
4.1	ATLAS Simulation Process	40
4.1.1	Event Generators	43
4.2	ATLAS Simulated Data Sets	46
4.3	ATLAS Reconstruction	47
4.3.1	Primary Vertex Reconstruction	47
4.3.2	Jet Reconstruction and Calibration	48
5	Theoretical Predictions of $R_{3/2}$	53
5.1	NLO Predictions of $R_{3/2}$	53
5.1.1	Theoretical Uncertainties	56
5.1.2	Hard Scale Parametrization Selection	58
5.2	Non-Perturbative QCD Corrections	60
5.2.1	Uncertainty on Non-Perturbative QCD Correction	62
6	Data Measurement of $R_{3/2}$	70
6.1	Event Selection	70
6.1.1	Event & Jet Selection Criteria	70
6.1.2	Trigger Selection	73
6.2	Unfolding of Detector Effects in Data	78
6.2.1	Uncertainties on Data Unfolding	80
6.3	Uncertainties on $R_{3/2}$ Measurement	83
6.3.1	Statistical Uncertainties	83
6.3.2	Trigger Selection Efficiency	84
6.3.3	Jet Energy Scale Uncertainty	84
6.3.4	Jet Energy and Angular Resolutions	85
6.3.5	Jet Quality Requirements	86
7	Strong Coupling Measurement	89
7.1	Comparison of $R_{3/2}$ Measurement to Theoretical Predictions	89
7.2	Measurement Technique	90
7.3	Results	92
8	Summary, Conclusions and Outlook	99
	Appendix A - Nuisance Parameters in α_S Fit	101
	REFERENCES	103
	KEY TO ABBREVIATIONS	109

LIST OF TABLES

<u>Table</u>	<u>page</u>
2–1 Colour hypercharge and isospin charge values for each colour state.	8
4–1 LO Monte-Carlo simulated data samples used and their configuration.	47
5–1 Detailed uncertainty contributions to theoretical predictions of $R_{3/2}$	63
6–1 Trigger items considered for the analysis, for each data-taking period.	74
6–2 Trigger items used for the analysis, for each data-taking period and Q' bin.	77
6–3 Detailed uncertainty contributions to the measurement of $R_{3/2}$	80
7–1 Correlation of systematic uncertainties	91
7–2 α_S results from the least squares fit	94
7–3 Uncertainty contribution estimates to α_S results	97
A–1 Nuisance parameters used to obtain the best fit of $\alpha_S(M_Z)$ for each Q' bin, as well as all bins combined.	101
A–2 Nuisance parameters used to obtain the best fit of $\alpha_S(M_Z)$ for each Q' bin, as well as all bins combined. (continued)	102

LIST OF FIGURES

<u>Figure</u>	<u>page</u>
1–1 Elementary particles of the Standard Model	3
1–2 Schematic representation of the analysis	6
2–1 Running of the strong coupling constant	11
2–2 Allowed interactions between partons in QCD	12
2–3 Sample $2 \rightarrow 2$ parton Feynman diagrams	12
2–4 Sample $2 \rightarrow 3$ parton Feynman diagrams	13
2–5 Example of next-to-leading order Feynman diagrams	14
2–6 Parton showering example for two primordial quarks	17
3–1 CERN accelerator complex	23
3–2 Layout of the ATLAS subsystems	24
3–3 Particle identification in ATLAS	25
3–4 Layout of the ATLAS tracking system	26
3–5 Layout of the ATLAS muon spectrometer	30
3–6 Geometry of ATLAS magnets systems	31
3–7 Layout of ATLAS calorimeters	37
5–1 Examples of NLOJET++ two- and three-jet differential cross-section predictions as a function of renormalization and factorization scale factors	55
5–2 Optimized renormalization and factorization scale factors for the two-jet differential cross-section predictions from NLOJET++	64
5–3 Optimized renormalization and factorization scale factors for the three-jet differential cross-section predictions from NLOJET++	65
5–4 Sensitivity of $R_{3/2}$ NLOJET++ predictions to α_S variations.	66

5-5	$R_{3/2}$ NLOJET++ predictions with theoretical uncertainty. . .	67
5-6	Non-perturbative QCD correction and final $R_{3/2}$ theoretical prediction.	68
5-7	Non-perturbative QCD correction factors' uncertainty.	69
6-1	Data unfolding and final $R_{3/2}$ data measurement	79
6-2	Systematic uncertainty on $R_{3/2}$ unfolding due to pile-up effects.	82
6-3	Systematic uncertainty on $R_{3/2}$ unfolding due to Monte-Carlo modelling choices.	83
6-4	Systematic uncertainty on $R_{3/2}$ measurement due to jet energy scale uncertainty.	85
6-5	Systematic uncertainty on $R_{3/2}$ measurement due to jet energy resolution and angular resolution.	87
6-6	Systematic uncertainty on $R_{3/2}$ measurement due to jet quality selection criteria.	88
7-1	Comparisons of $R_{3/2}$ measurement to theoretical predictions.	90
7-2	Examples of spline interpolation to obtain a continuous description of $R_{3/2}^{(theory)}(\alpha_S(M_Z))$ in each Q' bin.	93
7-3	Comparison between the measured $R_{3/2}$ distribution and theoretical predictions at the measured α_S value of 0.111	95
7-4	Comparison between past α_S measurements and the result from this analysis	96
7-5	Comparisons α_S measurements and RGE predictions	98

CHAPTER 1

Introduction

Looking at the world around us, it is hard to imagine that everything we see is ultimately composed of elementary particles obeying four fundamental forces. This incredible, yet inevitable conclusion can be drawn from theories and experiments developed and performed by thousands of physicists since the early 20th century. One of the four fundamental forces, known as the strong force, is responsible for binding protons and neutrons together to form the nucleus of atoms, but also for the existence of those protons and neutrons. The work presented in this thesis describes a measurement of the strong force's strength at unprecedented energies, using a new approach, thereby validating our understanding of one of the four fundamental forces of nature.

The remainder of this chapter provides a brief overview of the basic concepts of particle physics, and of the analysis presented in this document. Chapter 2 introduces advanced theoretical concepts relevant for the results presented in this thesis. Chapters 3 and 4 respectively provide descriptions of the physical apparatus and software used to collect, simulate and reconstruct data. Theoretical predictions of distributions used to perform the analysis are described in chapter 5, while the measurement of those distributions from data is described in chapter 6. Chapter 7 compares theoretical predictions to data measurements to obtain the final results of this analysis. The analysis conclusions that can be drawn are summarized in chapter 8.

1.1 Theory Overview

Our current understanding of the universe leads us to believe that the world around us is composed of elementary particles governed by four fundamental forces known as the electromagnetic, weak, strong and gravitational interactions. These four interaction types mediate the dynamics of the subatomic world. The Standard Model theory of particle physics was developed to explain observed phenomena resulting from the presence of electromagnetic, weak and strong forces. The current formulation of the Standard Model does not include gravitational interactions; however, gravitational effects are generally negligible at the subatomic scale [1] and can therefore be safely omitted from all Standard Model calculations. The Standard Model was used to make several predictions, such as the existence of the top quark, which would later be confirmed experimentally. The large body of data agreeing with Standard Model predictions greatly contributed to establishing it as a generally reliable description of particle interactions at all energy scales studied to this date.

Twelve elementary particles known as *fermions* are currently included in the Standard Model. A corresponding antiparticle of equal mass but opposite charges (or quantum numbers) is also postulated to exist for each fermion. Figure 1–1 shows the different types of fermions classified as either *quarks* or *leptons*. There exists six types, also known as flavours, of quarks and six leptons. Quarks are fundamentally different from leptons in that they carry colour¹ charge and therefore interact via the strong force. This leads them to form bound states known as *hadrons*. Quarks also carry electrical charge, as seen in figure 1–1, which allows them to interact through the electromagnetic

¹ Colour charges and the theory of strong interactions are discussed in section 2.1.

force as well. Finally, the only way a quark can change flavour is through the weak interaction. Both electromagnetic and weak interactions are generally negligible when compared to the strong force [1]. Leptons do not carry colour charge, and therefore do not interact via the strong force. Leptons known as neutrinos have very small non-zero masses and do not carry any electrical charge. These particles therefore interact with matter solely through weak interactions. This feature renders neutrinos notoriously difficult to detect. Charged leptons, such as electrons, carry electrical charge and therefore interact mainly via the electromagnetic force.

Leptons (spin 1/2)	up (u) Charge: 2/3 e Mass: 2.4 MeV	charm (c) Charge: 2/3 e Mass: 1.29 GeV	top (t) Charge: 2/3 e Mass: 172.9 GeV	photon (γ) Charge: 0 e Mass: 0 eV	Bosons (spin 1)	
	down (d) Charge: -1/3 e Mass: 4.9 MeV	strange (s) Charge: -1/3 e Mass: 100 MeV	bottom (b) Charge: -1/3 e Mass: 4.2 GeV	gluon (g) Charge: 0 e Mass: 0 eV		
	Leptons (spin 1/2)	electron neutrino (ν_e) Charge: 0 e Mass: < 2.2 eV	muon neutrino (ν_μ) Charge: 0 e Mass: < 0.17 MeV	tau neutrino (ν_τ) Charge: 0 e Mass: < 15.5 MeV		Z-boson (Z) Charge: 0 e Mass: 91.2 GeV
		electron (e) Charge: -1 e Mass: 0.511 MeV	muon (μ) Charge: -1 e Mass: 105.7 MeV	tau (τ) Charge: -1 e Mass: 1.777 GeV		W$^\pm$-boson (W) Charge: ± 1 e Mass: 80.4 GeV

Figure 1–1: Summary figure of elementary particles of the Standard Model and their respective mass, electric charge and spin [2].

Both quarks and leptons can be divided in three pairs of particles known as generations. A quark generation is composed of one quark flavour with electrical charge $2/3$ and one with $-1/3$ in units of electron charge e . A lepton generation on the other hand is composed of one electrically charged lepton

with charge $-1e$, and its corresponding electrically neutral neutrino. Only the first generation of charged fermions, composed of the lightest particles, is stable. Charged particles from both the second and third generations decay into lower generations with short half-lives. The first, second and third generations correspond to the first three columns of figure 1-1 in that order. The *up* and *down* quarks are the basic constituents of protons and neutrons which, along with electrons, are themselves the building blocks from which all atoms currently known to man are built.

Also included in the Standard model are five *bosons*, which act as force carriers or mediators. Photons are electrically neutral, but couple to electric charge in particles and are therefore mediators of the electromagnetic force. Three massive bosons known as the W^+ , W^- and Z , whose masses are given in figure 1-1, mediate the weak interactions. Finally, *gluons* are massless and electrically neutral, but couple to colour charge, and are therefore mediators of the strong force.

1.2 Analysis Overview

Collisions of protons (i.e. hadrons) often result in the production of two or more quarks or gluons. The probability of producing quarks or gluons depends on the number of particles produced, and the strength of the strong force at the energy of the collision. This analysis counts the number of collisions showing indications that three-or-more or two-or-more quarks or gluons were produced at different collision energies. The value of the ratio of these two quantities therefore depends on the strength of the strong force. A measurement of the strength of the strong force as a function of collision energy is obtained by comparing the measured value of this ratio to theoretical calculations. Finally, the energy dependence of the strength of the strong force is measured at energies beyond those of any past measurements. Figure 1-2

gives a schematic overview of the different parts of the analysis and how they lead to the measurement of the strength of the strong force.

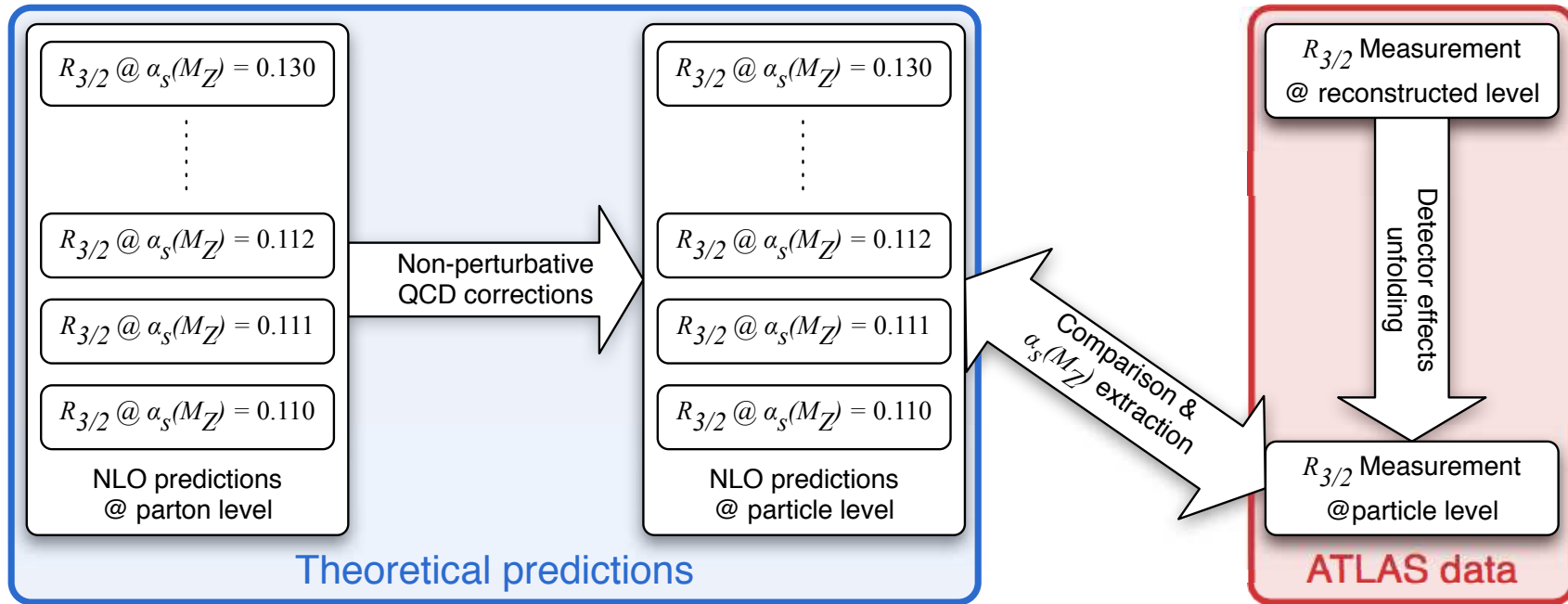


Figure 1–2: Schematic representation of the analysis, where $R_{3/2}$ represents the ratio of the number of collision showing indications that three-or-more quarks or gluons were produced, to that where two-or-more are produced, as explained in chapter 2. Theoretical predictions are described in chapter 5 while the measurement from data is described in chapter 6. Finally the strength of the strong force, measured through the parameter $\alpha_s(M_Z)$, is extracted by comparing theoretical predictions of the ratio $R_{3/2}$ to their measured value, as described in chapter 7.

CHAPTER 2

Theoretical Foundations

According to our current understanding of physical processes, forces can be described by gradients of fields. Field theories are therefore used in the studies of fundamental interactions. The Standard Model of particle physics is a quantum field theory defined by a $SU(3) \times SU(2) \times U(1)$ gauge symmetry. The invariance of the theory under local symmetry transformations is achieved by the introduction of vector fields, which when quantized become gauge bosons, the ‘force carriers’. Quantum Chromodynamics (QCD) is the $SU(3)$ quantum field theory describing strong interactions and is part of the Standard Model of particle physics.

This chapter first describes the theory of strong interactions, followed by practical applications of the theory to describe hadron collisions. The last section describes how the study of these hadron collisions can be used to measure the strong coupling constant α_S , which in the theory of QCD provides a measure of the strong interaction strength.

2.1 Theory of Strong Interactions

According to quantum mechanics, fermions can be described by a probability wavefunction. A quark’s wavefunction is composed of three parts: spatial, spin, and colour. The quark’s colour wavefunction, which allows them to interact via the strong force, can take three different colour states named after the colours *red* (r), *green* (g) and *blue* (b). For antiparticles, these states become the anticolours *anti-red* (\bar{r}), *anti-green* (\bar{g}) and *anti-blue* (\bar{b}). These

colour states correspond to a combination of two conserved and additive quantum numbers: a *colour hypercharge* and a *colour isospin charge*. The values for these quantum numbers for each state are listed in table 2–1.

Table 2–1: Values of the colour hypercharge Y^C and the colour isospin charge I_3^C for quarks and antiquarks

Quarks			Antiquarks		
Colour	Y^C	I_3^C	Colour	Y^C	I_3^C
r	$1/3$	$1/2$	\bar{r}	$-1/3$	$-1/2$
g	$1/3$	$-1/2$	\bar{g}	$-1/3$	$1/2$
b	$-2/3$	0	\bar{b}	$2/3$	0

Gluons, the strong force mediators, couple to colour charge in a very similar way that photons couple to electric charge in electromagnetic interactions. However, gluons are fundamentally different from photons in that they themselves carry colour charge. As a matter of fact, gluons carry a quantum mechanical combination of both colour and anticolour states. Gluons can therefore not only couple to quarks, but also to each other. This property of gluon interactions is at the origin of two properties of strong interactions called *colour confinement* and *asymptotic freedom*.

2.1.1 Colour Confinement

According to the colour confinement hypothesis, only states with total colour hypercharge (Y_C) and colour isospin charge (I_3^C) of zero can be observed. The colour confinement hypothesis therefore precludes us from observing individual *partons*, where a parton is defined as either a quark or a gluon. Quark bound states known as hadrons are required to satisfy the colour confinement requirements. These states are also known as colour singlets or colourless states. Two types of hadrons have been observed: quark-antiquark pairs called mesons, and three-(anti)quark combinations called baryons.

2.1.2 Asymptotic Freedom

Asymptotic freedom is a defining property of the strong force, according to which the strength of interactions weakens with decreasing interaction distances. These short-distance interactions are associated with large energy-momentum transfers (Q) between particles. The strength of strong interactions, and hence the value of the strong coupling constant α_S , therefore decreases as the energy-momentum transfer increases. The dependence of the strong coupling constant on the interaction's energy-momentum transfer, or the *hard scale* of the scattering, is known as the *running* of the coupling.

2.1.3 Running of the Strong Coupling Constant

Due to asymptotic freedom, the strong coupling constant α_S is small enough at high energy momentum transfers Q that perturbation theory [3] can be applied to QCD calculations. In the framework of perturbative QCD (pQCD), the running coupling satisfies the renormalization group equation (RGE) [4]

$$\mu_R^2 \frac{d\alpha_S}{d\mu_R^2} = \beta(\alpha_S) = -(b_0\alpha_S^2 + b_1\alpha_S^3 + \dots), \quad (2.1)$$

where μ_R is an unphysical parameter known as the renormalization scale. To be representative of the interaction strength, the strong coupling is evaluated at $\mu_R = Q$, the energy-momentum transfer of the interaction. In the commonly used modified minimal subtraction ($\overline{\text{MS}}$) renormalization scheme [5], the one-loop [6, 7] and two-loop [8–10] beta-function coefficients introduced in equation (2.1) are

$$b_0 = \frac{33 - 2n_f}{12\pi} \quad (2.2)$$

$$b_1 = \frac{153 - 19n_f}{24\pi^2} \quad (2.3)$$

where n_f is the number of light quark flavours, and a quark flavour is considered light if its mass is smaller than the renormalization scale $\mu_R = Q$. A

two-loop solution to the RGE [11] approximated to $O(t^{-2})$ is given by

$$\alpha_S(Q) \simeq \frac{1}{b_0 t} \left(1 - \frac{b_1 \ln t}{b_0^2 t} \right), \quad t \equiv \ln \frac{Q^2}{\Lambda^2}, \quad (2.4)$$

where the integration constant Λ corresponds to the energy scale below which perturbation theory cannot be applied to QCD, and is dependent upon the renormalization scheme used. The RGE can also be solved exactly using numerical methods; and in such cases there is no integration constant. To avoid the ambiguity associated with the different methods and renormalization schemes used in the determination of the strong coupling constant, the α_S value is usually quoted at a specific scale (typically $Q = M_Z \cdot c$, the mass of the Z boson). The current accepted world average of the strong coupling constant is $\alpha_S(M_Z) = 0.1184 \pm 0.0007$ [12]. The running of the coupling is illustrated in figure 2–1 using the previously described two-loop solution to the RGE.

2.2 Hard Scattering Processes in Hadron Collisions

This section first describes how perturbative QCD can be used to study parton collisions resulting in the creation of outgoing partons. The concept of factorization is then introduced to compute QCD predictions of hadron collisions resulting in the creation of outgoing partons. Finally, the evolution of outgoing partons into particle jets is described.

2.2.1 Hard Scattering of Partons

A hard scatter of partons is defined as a collision in which the energy-momentum transfer between partons is clearly large enough (few GeV/c) to justify the application of perturbation theory to QCD. Some of the most common outcomes of such hard scatterings include two or more partons being produced. Parton collisions leading to the production of two or more outgoing

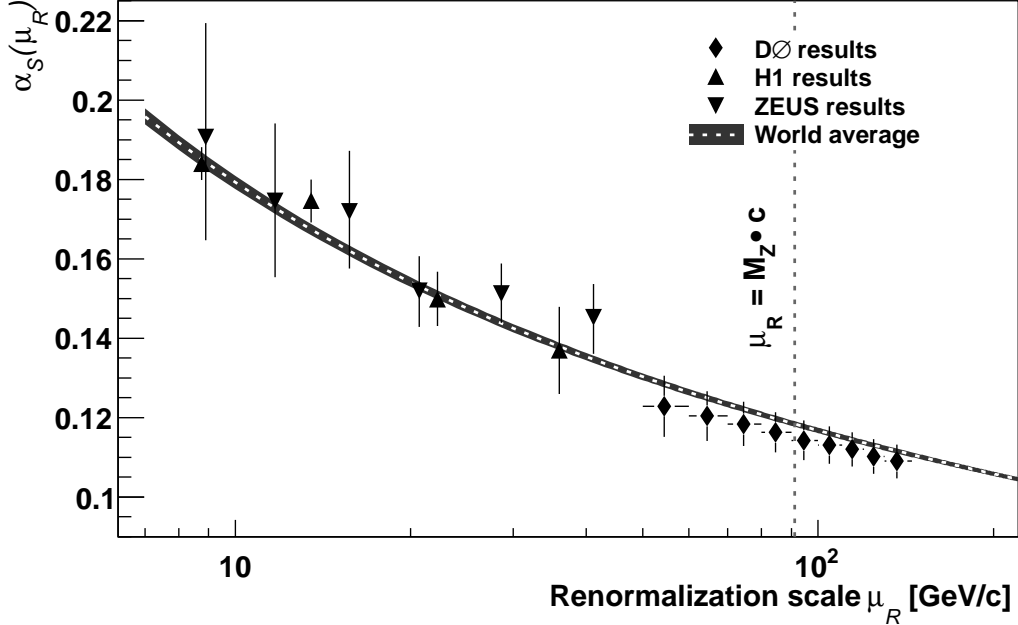


Figure 2–1: Running of the strong coupling constant as a function of renormalization scale μ_R using the two-loop approximate solution to the RGE [11] and the accepted world average of the strong coupling constant $\alpha_S(M_Z) = 0.1184 \pm 0.0007$ [12]. Results from the D0 inclusive jet fit [13], ZEUS [14] and H1 [15] collaborations are also shown.

partons can be studied using Feynman diagrams. These diagrams provide a visual representation of terms from perturbation series in quantum field theory, including QCD [16]. These diagrams can be interpreted as scattering matrix elements using Feynman’s rules [16], which can then be used to compute the cross-section of a specific process.

Figure 2–2 shows Feynman diagrams representing the different types of interactions allowed in QCD between quarks and gluons. Each type of interaction has a certain probability of occurring, which is proportional to powers of the strong coupling constant α_S , as labelled in the figure.

Larger diagrams can be constructed by combining the above three basic interaction diagrams. The probability of the interaction portrayed to occur is proportional to the square of the product of the probabilities of each vertex.

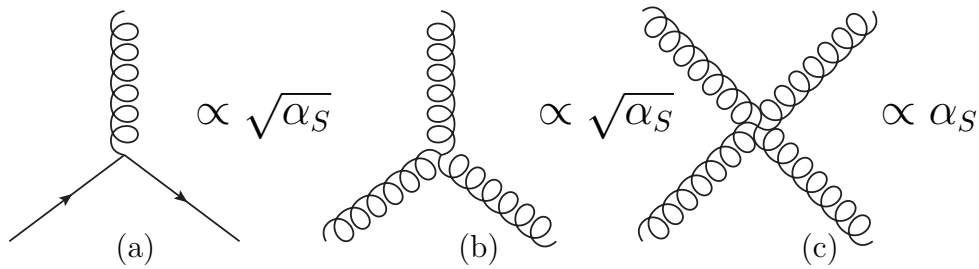


Figure 2–2: The three Feynman diagrams represent the possible interaction vertices between partons. Quarks are represented by lines and gluons by springs. Figure (a) shows a quark-gluon interaction similar to a photon-electron electromagnetic interaction. Figures (b) and (c) show gluon-only interaction vertices which are a direct consequences of gluons carrying a colour charge and for which there are no equivalents in quantum electrodynamics. The probability of each interaction vertex to occur is proportional to powers of the strong coupling constant α_S , as labelled next to each diagram.

The probability of a certain reaction to occur is expressed in terms of a *cross-section* with units known as *barns*¹ (b). Diagrams such as those shown in figure 2–3 therefore have a cross-section, σ , proportional to α_S^2 , while those in figure 2–4 have a cross-section proportional to α_S^3 . These diagrams effectively represent contributions in a pQCD series.

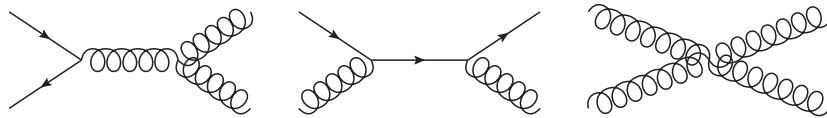


Figure 2–3: Sample Feynman diagrams for the production of two outgoing partons from a hard scattering of two incoming partons. The interactions evolve with time from left to right.

¹ The barn unit is defined as 10^{-28} m^2 .

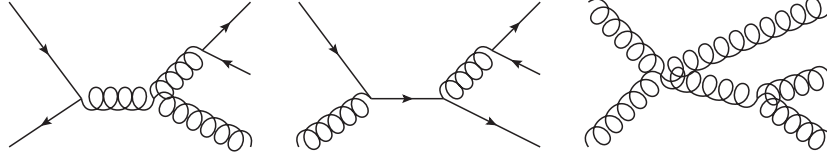


Figure 2–4: Sample Feynman diagrams for the production of three outgoing partons from a hard scattering of two incoming partons. The interactions evolve with time from left to right.

Several more diagrams featuring two initial² and two final state³ partons could be drawn. The diagrams with the highest probabilities of occurrence ($\propto \alpha_S^2$) are called leading order (LO) diagrams. Higher order contributions include diagrams with cross-sections proportional to higher powers of α_S . Summing the contributions from all possible LO diagrams yields the total pQCD LO approximation of the cross-section for the process involving the hard scatter of two incident partons and the creation of two outgoing partons.

Next-to-leading order (NLO) pQCD predictions of N outgoing partons cross-sections account for several additional $O(\alpha_S^{N+1})$ terms in the pQCD expansion. These terms correspond to diagrams similar to figures 2–3 and 2–4 but with an additional parton present. The parton can be emitted and then re-absorbed in the same diagram (figure 2–5(a)), which is known as a *virtual* correction, or it can be emitted resulting in a total of $N + 1$ outgoing partons (figure 2–5(b)), which is known as a *real* correction. Total NLO cross-sections are therefore generally computed for inclusive final state parton multiplicities, e.g. requiring the number of partons $N \geq 2$, so as not to artificially truncate the perturbation series. The total inclusive $2 \rightarrow N$ partons production cross-section $\sigma_{N_{partons}}^{(partons)}$ approximated at N^jLO is calculated as the square of the sum

² Initial state particles are present before the hard scattering takes place.

³ Final state particles are present after the hard scattering took place.

of all contributing diagrams, and can therefore be expressed as the sum

$$\sigma_{N_{partons}}^{(partons)} = \alpha_S^N \sum_{i=0}^j (c_i \alpha_S^i), \quad (2.5)$$

where the c_i coefficients depend on the kinematics of the interaction.



Figure 2–5: Example of NLO Feynman diagrams for virtual (a) and real (b) corrections to pQCD calculation of the inclusive two-parton cross-section from a hard scattering of two incoming partons. The interactions evolve with time from left to right.

Partons are confined within bound states known as hadrons. Theoretical cross-section predictions compared to experimental measurements presented in this thesis therefore need to describe hadron collisions.

2.2.2 Hadron Collisions

As described in section 2.1.1, all known hadrons are composed of two or three quarks known as *valence*⁴ quarks. Quarks within hadrons continuously emit and absorb gluon radiation. Gluons on the other hand continuously and spontaneously create quark-antiquark pairs which then annihilate back into gluons. Thus, at any moment, valence quarks ‘bathe’ in a *sea* of quarks and gluons. The total momentum of the hadron is therefore divided among all its constituents. Moreover, the internal structure dynamics of hadrons belongs to the non-perturbative regime of QCD and therefore cannot be included in

⁴ *Valence* quarks, unlike *sea* quarks, are used to determine a hadron’s quantum numbers.

pQCD calculations. In order to perform QCD calculations involving non-perturbative effects, factorization theorems [17] are used.

Factorization theorems allow to separate (factorize) non-perturbative from perturbative effects contributing to a hadronic collision. Applying factorization theorems therefore allows the computation of perturbative effects such as the hard scatter of quarks and gluons by pQCD, while non-perturbative effects, typically too complicated to be computed directly, are modelled after precise measurements from particle colliders. The separation between non-perturbative and perturbative effects is parametrized by the factorization scale μ_F . In the $\overline{\text{MS}}$ factorization scheme [5], particle emissions with transverse momenta larger than the factorization scale are accounted for in pQCD, while emissions with transverse momenta smaller than the factorization scale are included in non-perturbative modelling of the interaction.

The internal structure dynamics of hadrons is modelled by parton distribution functions (PDFs). The PDFs are measured experimentally as a function of the factorization scale μ_F . These PDFs provide the probability of an incident particle to strike a parton carrying a fraction x of the proton's momentum at a specific energy-momentum transfer value.

Equation (2.5) can therefore be modified to express the N^jLO cross-section $\sigma_{N_{partons}}^{(hadrons)}$ of the production of N outgoing partons from a hadron-hadron collision as

$$\sigma_{N_{partons}}^{(hadrons)} = \left(\alpha_S^N \sum_{i=0}^j (c_i \alpha_S^i) \right) \otimes f_1(x_1) \otimes f_2(x_2), \quad (2.6)$$

where the c_i coefficients depend on the kinematics of the interaction, $f_{1,2}$ are the PDFs of the two initial state hadrons, and the \otimes symbol indicates the convolution over the momentum fractions x_1 and x_2 of the hadrons.

2.2.3 Particle Jets

Outgoing partons resulting from a hadron collision are ejected from the hard scattering interaction point in different directions in accordance with energy and momentum conservation laws. As these partons get further away from each other, the strong interaction strength between them increases rapidly. When the separation distance reaches $\sim 10^{-15}$ m, the strong interaction strength becomes so great that it is energetically preferable for partons to radiate a gluon. Gluons can then also radiate other gluons or produce quark-antiquark pairs, which themselves can radiate gluons as well. This cascading process, as depicted in figure 2–6, repeats itself until it is no longer energetically favourable for new partons to be created. New partons created this way are predominantly collinear with the original primordial partons. This leads to the creation of parton *sprays* in the direction of the primordial partons originating from the hard scattering. The process responsible for the creation of those *sprays* or *showers* is known as *parton showering* or *fragmentation*. Following the showering process is the *hadronization* of partons. During this process, partons merge together into hadrons. These two processes are almost entirely non-perturbative and are described by showering and hadronization models rather than pQCD.

With the exception of top quarks, parton jets are generally created before primordial partons decay into other particles. The sum of all the particles in a jet thus generally reflects very closely the kinematic properties of the parton from which the jet originated.

Factorization theorems, PDFs, showering and hadronization models can be combined with pQCD calculations of the hard scattering of two partons to predict the probability of producing two or more particle jets. Based on equation (2.6), the expression describing the total N^JLO cross-section for the

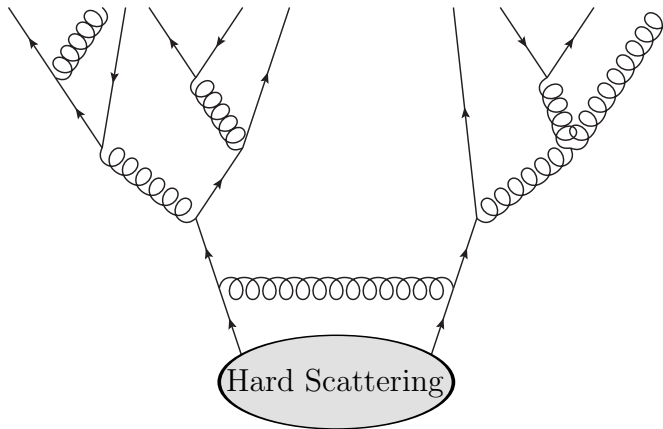


Figure 2–6: Sample parton showering diagram for two primordial quarks emerging from a hard scattering interaction. New partons are created until it is no longer energetically favourable to do so. The interaction evolves with time from bottom to top.

production of N -jets in a hadron collision can be written as

$$\sigma_{N_{jets}} = C_{non-pert} \cdot \left[\left(\alpha_S^N \sum_{i=0}^j (c_i \alpha_S^i) \right) \otimes f_1(x_1) \otimes f_2(x_2) \right], \quad (2.7)$$

where the c_i coefficients depend on the kinematics of the interaction, $f_{1,2}$ are the PDFs of the initial state hadrons, the \otimes symbol indicates the convolution over the momentum fractions of the hadrons, and $C_{non-pert}$ represents the non-perturbative corrections due to showering and hadronization effects.

LO pQCD predictions of collisions resulting in N outgoing partons only include contributions from those N partons. Higher order pQCD calculations, on the other hand, account for the possibility that more than N partons are created. Similarly, non-perturbative effects can also lead to the creation of additional partons. These perturbative and non-perturbative emissions can sometimes lead to divergences in the QCD calculations if the quantity being calculated is too sensitive to those effects. Two conditions are required to avoid these divergences: the quantity being computed should be invariant under low-energy parton emissions, or *infrared* safe, and insensitive to the splitting of a

parton into two collinear ones, or *collinear* safe. For this reason, perturbative QCD predictions can only be compared to experimental observations if the chosen observable is defined such that it is both infrared and collinear safe. In the case where the observable is a jet production cross-section, this is achieved by using a jet reconstruction algorithm (see section 4.3.2) that is both infrared and collinear safe.

2.3 Observable for the Determination of α_S

Several techniques [12] have already been used to measure the value of the strong coupling through tau-lepton (τ) decays, radiative Υ decays, lattice QCD calculations of hadronic mass differences, electroweak measurements, non-singlet structure function measurements, hadronic event shapes, and jet production. Precision α_S measurements from jet production have been performed in electron-positron annihilation, deep-inelastic electron-proton scattering and hadron collisions up to energies of 209 GeV [12]. Due to the overwhelmingly large jet production cross-sections at hadron colliders, the strong coupling constant was also measured at the Tevatron by the CDF [18] and DØ [13] collaborations from the inclusive jet production cross-section. However, neither CDF nor DØ were able to extend the probed energy range beyond approximately 230 GeV due to two effects [19]:

- CDF and DØ results were used in the measurement of PDFs, leading to complicated correlations between experimental and theoretical uncertainties
- PDFs are calculated at different factorization scales using the DGLAP [20] procedure that assumes the validity of the RGE, which has only been experimentally verified up to energies of 209 GeV

Both issues are linked to the observable used to measure α_S , that is, the predictions of the inclusive jet cross-section directly depend on the PDFs.

Measuring the strong coupling at energy ranges beyond 209 GeV at a hadron collider should thus be performed using a quantity largely independent of PDFs, yet still sensitive to α_S . The three- to two-jet production cross-section ratio has been shown to satisfy both requirements [19].

The first step toward a measurement of the strong coupling constant is selecting a physical quantity, or observable, sensitive to changes in α_S . As described in section 2.2.1, the cross-section associated with the production of N partons, and hence N jets, is a function of α_S^N . It follows that in the LO pQCD approximation, the three- to two-jet production cross-section ratio defined as

$$R_{3/2}^{(LO)} = \frac{\sigma_{N_{jets}=3}}{\sigma_{N_{jets}=2}} \propto \alpha_S, \quad (2.8)$$

where $\sigma_{N_{jets}}$ is the N -jet production cross-section, is proportional to the strong coupling constant α_S . NLO pQCD predictions are, on the other hand, computed in such a way that they are by definition inclusive jet multiplicity production cross-sections. The inclusive jet production cross-section ratio at NLO can therefore be defined as

$$R_{3/2}^{(NLO)} = \frac{\sigma_{N_{jets} \geq 3}}{\sigma_{N_{jets} \geq 2}}, \quad (2.9)$$

where N_{jets} is the number of final state jets. The inclusive ratio is still sensitive to the strong coupling constant, although terms with higher orders of α_S are now present due to the inclusion of higher jet multiplicity contributions.

In order to observe the running of the coupling, the analysis is performed over different energy ranges, or energy *bins*, corresponding to different values of the energy-momentum transfer Q . The inclusive three- to two-jet cross-section ratio expressed as a function of a collision's hard scale Q is defined as

$$R_{3/2}(Q) = \left(\frac{d\sigma_{N_{jets} \geq 3}}{dQ} \right) / \left(\frac{d\sigma_{N_{jets} \geq 2}}{dQ} \right), \quad (2.10)$$

where the differential cross-sections $\frac{d\sigma_{N_{jets}\geq 2,3}}{dQ}$ are computed in pQCD at NLO. Experimental measurements of the inclusive three- to two-jet production cross-section, as defined in equation 2.10, can then be matched to NLO pQCD predictions to measure the strong coupling constant at different hard scales, in order to observe the running of the coupling.

CHAPTER 3

The ATLAS Experiment at the Large Hadron Collider

The Large Hadron Collider (LHC) [21] is the largest and highest energy particle collider built in human history. The LHC was designed to collide protons at the unprecedented centre-of-mass energy of 14 TeV approximately forty million times per second. In March 2010, protons were collided for the first time at a centre-of-mass energy of 7 TeV, which marked the beginning of the first large scale data taking campaign. Since then, the LHC has delivered well over 3 fb^{-1} of data and achieved unprecedented instantaneous luminosities¹ at a hadron collider. Section 3.1 provides an overview of the LHC and its operation.

The work presented in this thesis uses data recorded by the ATLAS (A Toroidal LHC ApparatuS) [22–24] detector, one of six particle detector experiments in operation at the LHC. ATLAS is a multipurpose detector designed to detect a broad range of physics signatures, including jets, electron, photons, muons and missing energy. A general description of the ATLAS detector is presented in section 3.2. Section 3.3 provides details about the ATLAS calorimeter system on which much of the work presented in this thesis depends.

¹ The instantaneous luminosity \mathcal{L} indicates the number of interactions N of a specific process generated per second by the LHC according to the equation $N = \mathcal{L}\sigma$, where σ is the cross-section of the studied process.

3.1 LHC Overview

The LHC [21] accelerator ring has a circumference of 26.7 km and is located in a tunnel between 45 m and 170 m underground, straddling the Swiss-French border. Two transfer tunnels of approximately 2.5 km link the LHC to the CERN accelerator complex which acts as injector, as illustrated in figure 3-1. Protons supplied to the LHC are first accelerated by the Linac 2 to an energy of 50 MeV. The protons are grouped together in *bunches* rather than in a continuous stream. These proton bunches are then injected into the Proton Synchrotron Booster which accelerates them to 1.4 GeV before injecting them into the Proton Synchrotron (PS). The PS further accelerates the proton bunches up to an energy of 25 GeV. The protons are then transferred into the Super Proton Synchrotron (SPS) which accelerates them again before injecting them into the LHC with an energy of 450 GeV. The LHC is designed to accelerate two proton beams in opposite directions, each to an energy of 7 TeV, before colliding them at the centre of the particle detectors built around the accelerator ring. The accelerator magnet system *squeezes* the beam size down as much as possible at the collision points in order to increase the likelihood of hard collisions to occur. However, even with nominal 64 μm wide bunches composed of 100,000 million protons, only approximately 20 collisions occur per bunch crossing, which is known as an *event*. Therefore, once the LHC has accelerated beams composed of up to 2808 proton bunches, it can collide them for several hours. When the beam intensities becomes too low, the beams are dumped and the machine is refilled.

In 2010, the LHC was able to collide proton beams at a centre of mass energy of 7 TeV [25], which was unprecedented for man-made particle colliders. Several physics runs were done with up to 9×10^{10} protons per bunch and 25 bunches per beam. The maximal number of bunches used in 2010 was 348.

This configuration resulted in a maximum average number of collisions per bunch crossing of approximately four. The fastest recorded turn-around time to re-fill the LHC from the Linac 2 after a beam dump, and to accelerate the new beam to 3.5 TeV was 3.66 hours, while a stable beam’s lifetime can range from 15 to 30 hours.

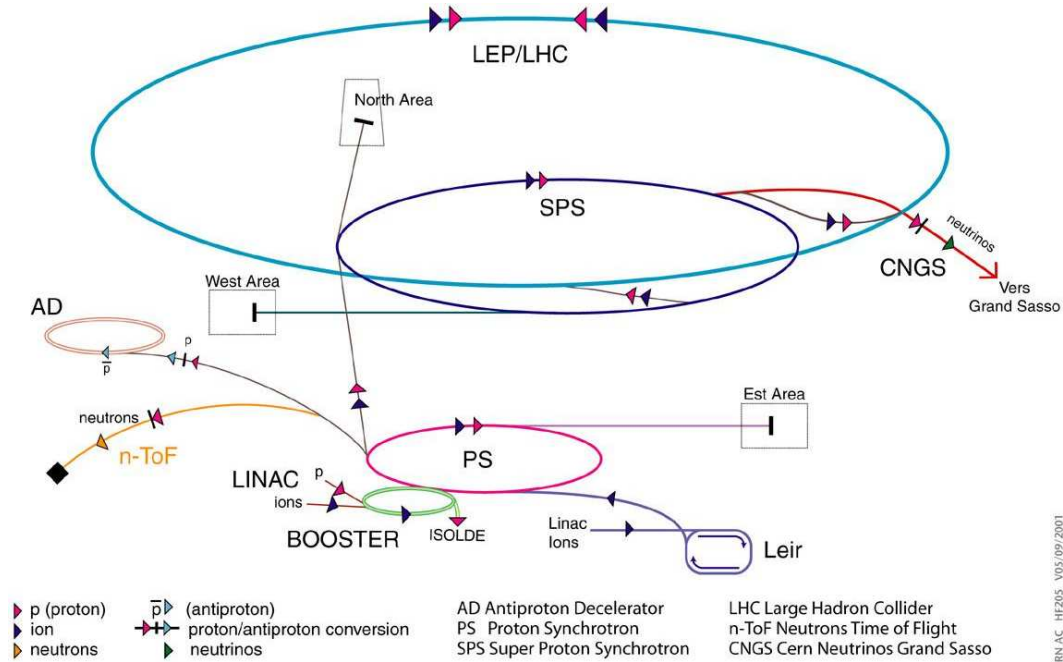


Figure 3–1: Diagram of the CERN accelerator complex. [26]

3.2 ATLAS Detector Overview

The ATLAS detector is designed to study a broad range of physics signatures containing photons, electrons, muons, jets and missing energy. To that end, it features

- a highly efficient tracking system designed to measure the trajectory of charged particles within high particle rate and occupancy level environments typical of the LHC,
- electromagnetic and hadronic calorimeters designed to identify and measure the energy of electrons, photons and jets with extensive angular coverage for accurate missing energy measurements,

- muon detectors capable of high-precision muon momentum measurements,
- and a triggering system designed to select potentially interesting collisions to save to permanent storage for a wide range of physics interests.

The overall layout of the detector and its sub-detector systems is illustrated in figure 3–2. When the LHC collides proton bunches at the centre of the detector, different types of particles emanating from the interaction point travel through the several layers of the detector, each corresponding to a different sub-detector system as illustrated in figure 3–3. Each sub-detector is briefly described in the following subsections with the exception of the ATLAS calorimeters, central to this analysis and described in details in section 3.3.

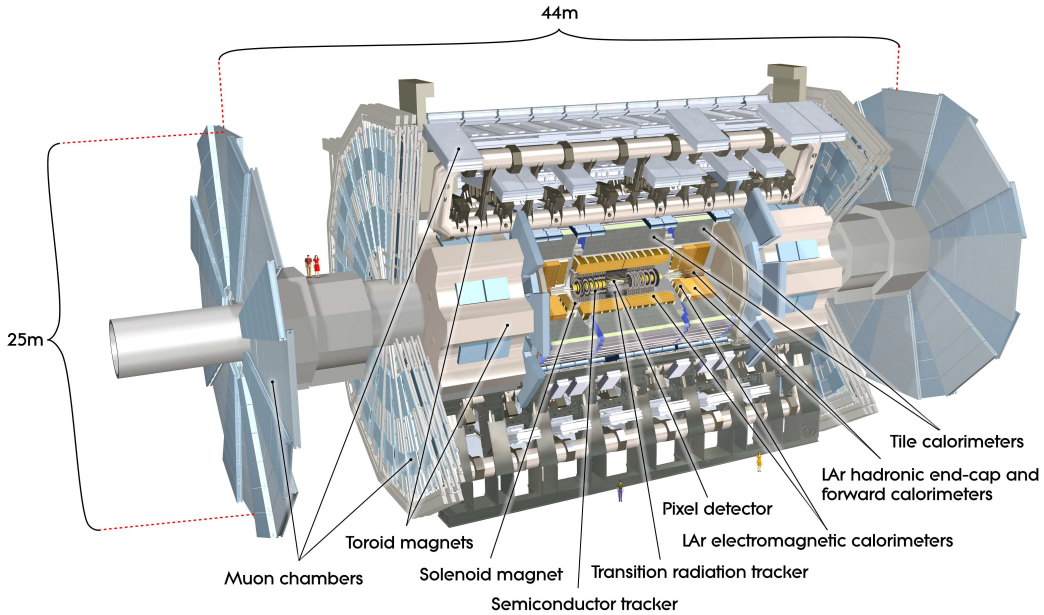


Figure 3–2: Layout of the ATLAS subsystems [24].

3.2.1 Nomenclature

In order to describe both the detector systems and measured physical quantities, Cartesian and cylindrical coordinates are used. The z -axis is defined by the particle beam and the origin is set to be at the nominal collision

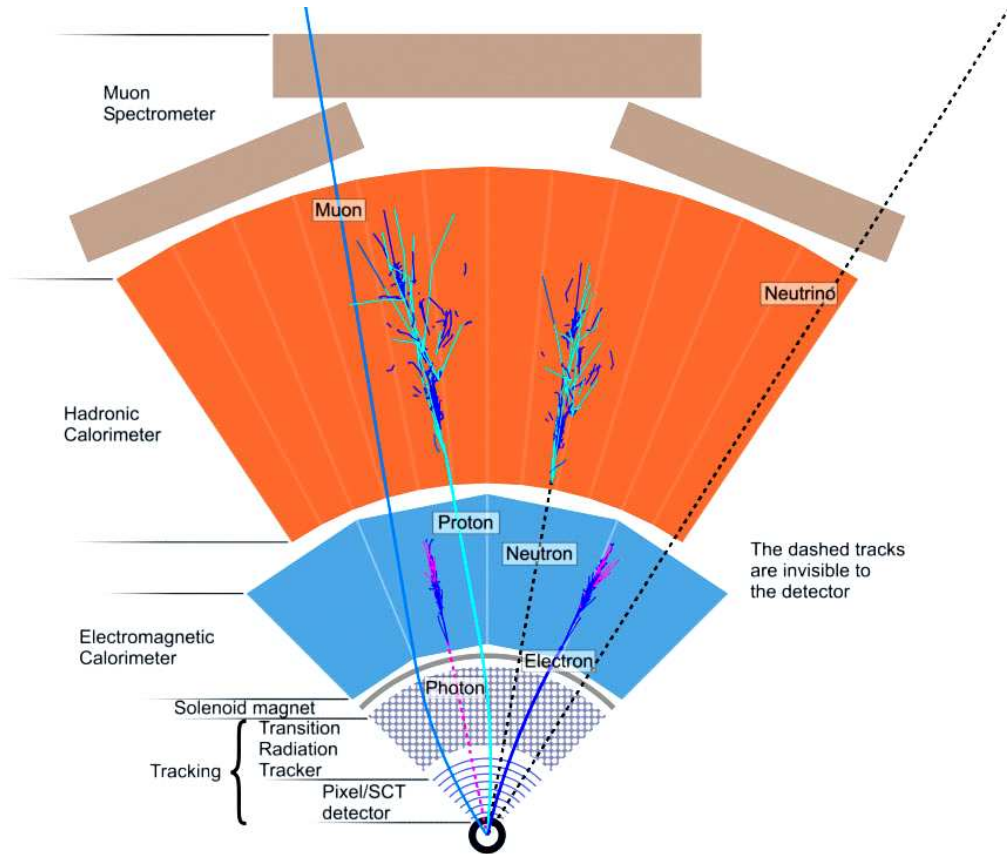


Figure 3–3: Particle identification by various ATLAS subsystems [27].

point. The positive x -axis is chosen to point toward the centre of the LHC ring while the positive y -axis points upward. In polar coordinates, the azimuthal angle ϕ sweeps the $x - y$ or *transverse* plane perpendicular to the beam axis. The polar angle θ is measured from the beam axis in the $r - z$ plane, where $r^2 = x^2 + y^2$. The pseudorapidity² is defined as $\eta = -\ln \tan(\theta/2)$ and the transverse momentum p_T , transverse energy E_T and other transverse variables are thus defined in the $x - y$ or $\eta = 0$ plane. The distance ΔR

² In the limit of massless particles, the pseudorapidity is equivalent to the rapidity $y = \frac{1}{2} \ln (E + p_z)/(E - p_z)$. At hadron colliders, the rapidity is preferred over the polar angle since the difference in rapidity of two particles is independent of Lorentz boosts along the beam axis. Also, it is useful to note that particle flux is constant as function of rapidity.

between two objects in the pseudorapidity-azimuthal angle space is defined as $\Delta R = \sqrt{(\Delta\phi)^2 + (\Delta\eta)^2}$.

3.2.2 Tracking System

As illustrated in figure 3–3, the ATLAS tracking system [22, 24, 28–30] is the closest sub-detector system to the interaction point. The tracking system is primarily tasked with vertex³ measurements, particle identification, and charged particle momentum measurements within the pseudorapidity region $|\eta| < 2.5$. The physics program requires the momentum resolution of charged particles σ_{P_T}/P_T to be better than $0.05\% P_T [\text{GeV}/c] \oplus 1\%$. Moreover, the full tracking system’s size is limited by the surrounding calorimeter systems, and its components must introduce as little material as possible upstream of the calorimeters.

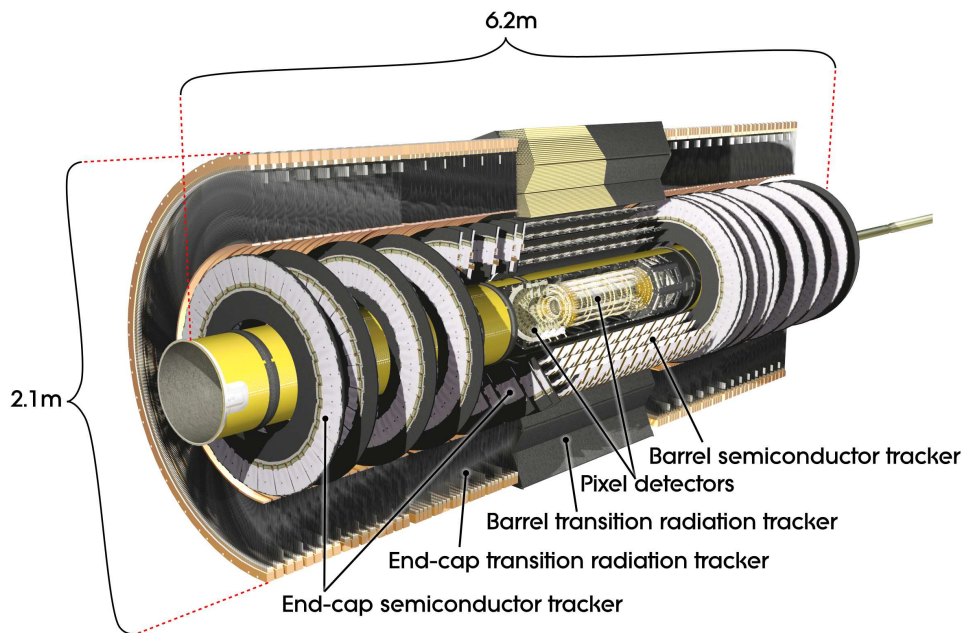


Figure 3–4: Layout of the ATLAS tracking system and its components. [24].

³ An interaction point of particles, for example the location of the hard scatter of the collision, or of a particle decaying in other particles.

In order to fulfill these physics and design requirements, the tracking system is composed of three complementary types of particle detectors arranged in layers: pixel, semiconductor tracker and transition radiation tracker as shown in figure 3–4. Each sub-detector can be divided into three units: the barrel and two identical end-caps. Each time a charged particle is detected while traversing a detector layer, its location along the layer’s surface is recorded. Such an occurrence is known as a hit. By combining several hits together, it is possible to reconstruct the path or *track* that a charged particle followed through the tracking system. Applying a strong magnetic field to the region monitored by the tracking system bends the charged particles’ trajectory. If the magnetic field is well understood, the radius of curvature of a track can then be used to infer a particle’s momentum. For this purpose, the tracking system is contained within a solenoidal magnet with a nominal magnetic field of 2 T. Pixel and semiconductor tracker sensors are located close to the interaction region to provide high-resolution pattern recognition capabilities. Innermost layers of the pixel detector contribute significantly to secondary vertex⁴ position measurements, while the semiconductor tracker is central to impact parameter⁵ measurements [24]. The transition radiation tracker provides continuous tracking information at larger radii, as well as electron identification through the measurement of transition radiation along the particle’s track. The final assembly forms a cylinder 7.02 m in length and 2.3 m in diameter [24].

⁴ A vertex which does not correspond to the hard scatter of the collision, e.g. vertices associated with heavy-flavour and τ -lepton decays.

⁵ The impact parameter of a particle track is the distance between the primary vertex and the track’s point of closest approach.

Pixel detectors [22, 24, 28–30] are placed as close as possible to the interaction region. The barrel unit consists of three concentric barrels located between ~ 5 cm and ~ 13 cm from the beam axis. End-cap units are composed of 3 disks placed on each side, perpendicular to the beam axis between radii ~ 8 cm and ~ 15 cm. Each track therefore crosses an average of three pixel layers. Each silicon pixel’s nominal size is $50 \times 400 \mu\text{m}^2$ and provides a spatial resolution of $10 \mu\text{m}$ and $115 \mu\text{m}$ in the $r - \phi$ and z directions, respectively.

The semiconductor tracker detector [22, 24, 28–30] envelops the pixel systems and covers the intermediate radial range of the tracking system. The semiconductor tracker’s barrel unit is composed of four layers of silicon microstrip detectors at radii between ~ 30 cm and ~ 52 cm. Each layer consists of a set of strips parallel to the beam direction and a set of small-angle (40 mrad) stereo strips glued together to obtain a z measurement. The end-cap units consist of nine disks of various radii to provide angular coverage up to a pseudorapidity of 2.5. Each disk is built from a set of strips running radially and a set of stereo strips at a relative angle of 40 mrad. A particle’s track therefore crosses an average of eight strip layers, providing four space-points. The resulting spatial resolution of the entire semiconductor tracker is $17 \mu\text{m}$ in the $r - \phi$ direction and $580 \mu\text{m}$ in z direction. This allows the pattern recognition algorithms to distinguish tracks that are more than approximately $200 \mu\text{m}$ apart.

The transition radiation tracker [22, 24, 28–30] is the outermost detector sub-system of the tracking system. It uses straw detectors to provide an average of thirty hits per track while maintaining good performance at high occupancy and counting rates. The use of straw detectors therefore allows for a large number of track points while keeping the amount of material upstream of the calorimeter systems within acceptable limits. Straws are aligned

along the beam direction in the barrel unit and radially in the eighteen end-cap wheels on each side. The end-cap wheels' radii and straw densities were adjusted to provide a constant number of crossed straws over the entire acceptance region. Each straw is 4 mm in diameter and filled with a xenon-based gas mixture, providing a spacial resolution of 130 μm per straw. Although transition radiation tracking points are not as precise as those provided by the pixel detector or semiconductor tracker, the large number of available points per track compensates the lack in precision which allows transition radiation tracking points to contribute significantly to momentum measurements.

3.2.3 Muon Spectrometer

The muon spectrometer, represented in figure 3–5, is the outermost detector system of the ATLAS detector. It is designed to measure the muons' momentum based on the magnetic deflection of their tracks within its acceptance range ($|\eta| < 2.7$). The ATLAS physics program requires a measured momentum resolution σ_{p_T}/p_T of at least 10% for a muon with momentum $p_T = 1$ TeV. The deflection of muons is achieved by large superconducting air-core toroid magnets interspersed and surrounded by tracking chambers.

The muon spectrometer's magnet system is composed of a barrel and two end-cap units. The geometry and alignment of these magnets are shown in figures 3–2 and 3–6. Both the barrel and end-cap units are composed of eight racetrack, double-pancake coils. The barrel toroids generate a magnetic field with bending power⁶ ranging from 1.5 to 5.5 Tm in the $|\eta| < 1.4$ region, while the end-cap units create a field with 1.0 to 7.5 Tm of bending power in the

⁶ The bending power is defined as the integral of the field component normal to the muon direction, computed along the infinite-momentum muon trajectory between the innermost and outermost muon chambers.

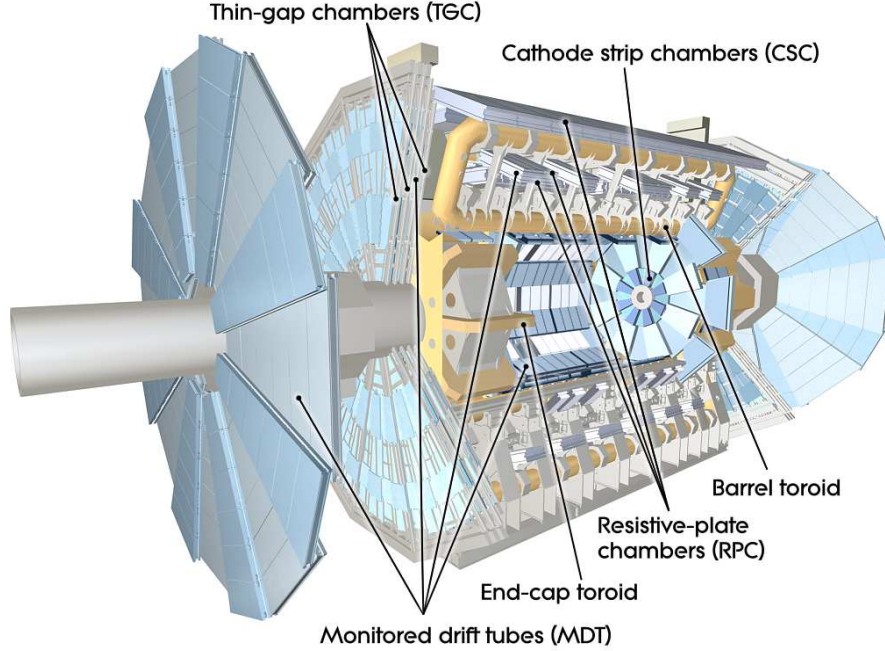


Figure 3–5: Layout of the muon spectrometer and its different tracking chamber types [24].

$1.6 < |\eta| < 2.7$ region. As depicted in figure 3–6, the end-cap toroids are placed within the barrel toroids. Both barrel and end-cap toroidal magnets thus contribute to the field in the $1.4 < |\eta| < 1.6$ pseudorapidity range. Moreover the end-cap units are rotated 22.5° with respect to the barrel unit in order to provide radial overlap of the magnetic fields and optimize the muon deflection in the $1.4 < |\eta| < 1.6$ region. The overall magnetic field is mostly orthogonal to the muon trajectories and is constantly monitored by ~ 1800 Hall sensors distributed throughout the muon spectrometer system.

The muon spectrometer features both high-precision and trigger-specific tracking chambers. Precision muon measurements are performed by three layers of monitored drift tubes throughout the acceptance range except for the forward region ($2.0 < |\eta| < 2.7$) of the innermost layer. Due to the high muon track density and particle flux, this region of the muon spectrometer uses cathode strip chambers. Each monitored drift tube module is equipped with

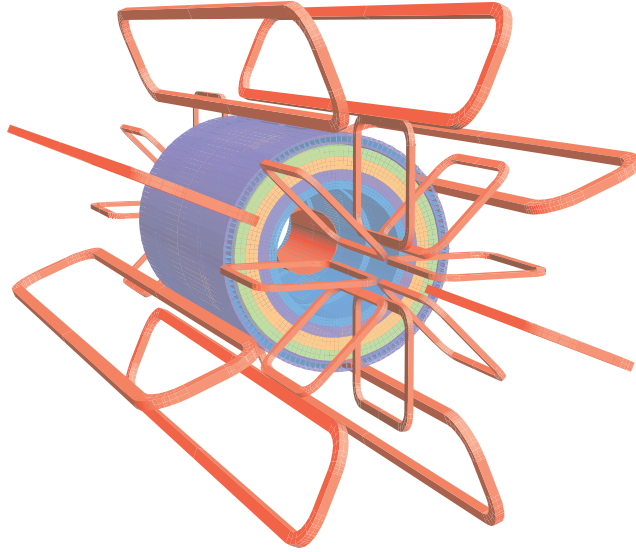


Figure 3–6: Geometry of ATLAS magnet systems and tile calorimeter steel. Both the barrel and end-cap units are composed of eight racetrack, double-pancake coils. The inner cylinder represents the tile calorimeter and its outside return yoke for the inner solenoid magnet. [24]

six or eight layers of drift tubes approximately 30 mm in diameter filled with an Ar/CO₂ gas mixture (93%/7%). Placed concentrically within each tube is a 50 μm tungsten-rhenium wire which collects ionisation electrons. This configuration provides each tube with an approximate resolution of 80 μm. Each cathode strip chamber module is composed of four planes, each one providing an azimuthal and pseudorapidity measurement with a resolution of approximately 60 μm per plane. On average, the monitored drift tubes provide 20 measurements per track over the whole acceptance range while cathode strip chambers provide 4 measurements per track.

The muon spectrometer’s trigger measurements are obtained using resistive plate chambers for the central ($|\eta| < 1.05$) region and thin gap chambers at larger polar angles ($1.05 < |\eta| < 2.7$). These trigger chambers are also used to provide bunch-crossing identification and complement the monitored drift tube measurements by measuring each track’s azimuthal coordinate.

3.2.4 Trigger

The ATLAS trigger system [22, 24] is designed to select in real-time potentially interesting collision events to be recorded for a detailed analysis. This system is optimized for event rejection in order to reduce the amount of data to be recorded to a sustainable rate of ~ 300 Mbytes/sec⁷ [24]. To that end, the system is composed of three sequential steps or levels: Level-1 (L1) , Level-2 (L2) and Event Filter (EF). Each level is designed to apply increasingly stringent requirements on each event. Less than 0.2% of the events satisfy the L1 selection criteria, reducing the event rate from 40 MHz to 75 kHz. The L2 further reduces the rate of selected events to 3.5 kHz. A nominal final average output rate of approximately 200 Hz is obtained by applying the EF trigger selection; however the final event rate can be significantly higher depending on the individual event size.

For an event to be deemed interesting by a specific trigger level, it must satisfy at least one selection criterion. The entire set of trigger selection criteria or trigger *items* form the trigger *menu*. The trigger menu is actually defined as a group of trigger *chains*. The simplest type of chain is composed of one L1, one L2 and one EF item. For more complex sets of criteria combining different types of detected features, chains can include several different trigger items for a single level. For an event to be recorded, it must satisfy all the trigger items of at least one trigger chain. In order to select a wide array of events and not only rare and highly energetic ones, some trigger chains are designed to have loose selection criteria. Since events satisfying these loose selection cuts can be very frequent, those trigger chains can easily saturate the entire available

⁷ Note that the system also has sufficient memory buffer to cope with bandwidth peaks of up to ~ 600 Mbytes/sec

bandwidth. To avoid this, trigger items with loose selections are pre-scaled⁸ to artificially reduce the associated chain(s)' output rate. Pre-scale factors can be set for any trigger item in order to fully optimize the available bandwidth of each level.

Since it must cope with an event input rate of 40 MHz, the L1 trigger is implemented using custom-made electronics. In order to reduce the individual events' processing time to an average of $2.5 \mu\text{s}$, the L1 trigger uses only a subset of the detector data. Resistive plate chambers and thin gap chambers are used to identify muon candidates, while all calorimeter systems with reduced-granularity information are used to detect electromagnetic clusters, jets, τ -lepton candidates, large amounts of missing and total energy. Each time such a feature is detected, the L1 trigger defines a region of interest. This region of interest includes the η and ϕ location of the feature, as well as its type and the satisfied L1 trigger item. The L2 and EF trigger algorithms can then focus on these regions of interest in order to save processing time.

The L2 and EF trigger levels form the high-level trigger (HLT) which is implemented almost exclusively on commercially available computers and networking hardware. HLT reconstruction algorithms have access to all the detector sub-systems and can use the full granularity information of each sub-detector. L2 algorithms are seeded by the L1 regions of interest and typically restrict themselves to the detector region surrounding the feature detected at L1. These algorithms are designed to refine the L1 selection process with advanced reconstruction techniques and more detailed detector information in

⁸ A pre-scale factor is an integer which quantifies the proportion of events satisfying a trigger item's criteria that passes the item's selection process. A pre-scale factor of N thus indicates that only 1 out of N events satisfying the associated item's criteria passes its selection.

an average of 40 ms per event. The EF algorithms on the other hand use reconstruction algorithms almost identical to those used in the ATLAS offline reconstruction software. Events satisfying at least one full trigger chain are then moved to permanent storage, along with a subset of the data generated during the trigger selection process. This information can then be used to seed offline analyzes.

3.3 ATLAS Calorimeter System

This section first introduces basic concepts of calorimetry. Section 3.3.2 uses these concepts to present the physics requirement of ATLAS calorimeter systems, while section 3.3.3 details the construction of the different ATLAS calorimeter modules.

3.3.1 Basic Concepts of Calorimetry

Calorimeter systems [31] are used in particle physics to measure the energy of particles through electromagnetic and strong interactions. To do so, particles are fully absorbed by an instrumented volume known as a calorimeter, which transforms the energy deposited by the particle into a measurable electrical signal. The process begins when an incident particle enters a calorimeter and interacts either electromagnetically or strongly with the material. A shower of secondary particles is then produced with particles of progressively lower energy. Charged particles from the shower deposit energy into the *active* medium of the calorimeter, producing electrical charge carriers or light. Instruments coupled to the active medium measure this activity which can then be used to infer the initial incident particle's energy.

The length and width of electromagnetic showers can be described in terms of *radiation lengths* X_0 , which is equal (proportional) to the average distance an electron (photon) needs to travel in a material to lose all but $1/e$ of its initial energy through bremsstrahlung (pair production). Similarly, the

interaction length λ , the mean distance travelled by a hadron before interacting with a nucleus of the material it's traversing, is used to describe hadronic showers.

Calorimeters can generally be classified as either electromagnetic or hadronic depending on the type of particles they are designed to detect and contain. Electromagnetic calorimeters are primarily used to measure the energy of electrons and photons through electromagnetic interactions such as bremsstrahlung or pair production (for energies greater than 10 MeV). Hadronic calorimeters are designed to measure the energy of hadrons through both electromagnetic and strong interactions. Calorimeters can also be classified as *sampling* or *homogeneous* based on their design. Sampling calorimeters are built using alternating layers of an absorber, a dense material used to produce the particle showers, and an active medium, which provides a sampling measurement of a shower's energy. A homogeneous calorimeter on the other hand is made of a single material that acts as both the absorber and active medium. Because all of a particle's energy would be deposited into its active medium, a homogeneous calorimeter generally features a much better energy resolution than a sampling calorimeter. However, homogeneous calorimeters are not as easily segmented as sampling calorimeters. A fine segmentation or granularity of the calorimeter is essential to measure the location or shape of a shower. The position measurement can, in turn, be used to match a shower to a particle track, helping in the task of particle identification. Homogeneous calorimeters are therefore less suited for experiments requiring strong position measurements and particle identification capabilities. Moreover, suitable materials for active mediums generally feature very large interaction lengths. Homogeneous calorimeters are therefore not generally used in the measurement of hadronic showers.

3.3.2 ATLAS Physics Requirements

The ATLAS calorimeter system [22, 24, 32–34], shown in figure 3–7, is designed to identify and reconstruct electrons, photons and particle jets, as well as measure missing energy. It is composed of electromagnetic and hadronic sampling calorimeters. The ATLAS physics program requires the energy resolution of the electromagnetic calorimeter σ_E/E to be at most $10\%/\sqrt{E [GeV]} \oplus 0.7\%$ for the pseudorapidity region $|\eta| < 3.2$, while the required energy resolution of the hadronic calorimeter for the same region is required to be at most $50\%/\sqrt{E [GeV]} \oplus 3.0\%$. In the forward region ($3.1 < |\eta| < 4.9$), the energy resolution requirements are less stringent at $100\%/\sqrt{E [GeV]} \oplus 10.0\%$. Furthermore, adequate material thickness and density of the calorimeter is required to limit the high energy jet (transverse momentum greater than 500 GeV) punch-throughs in the muon detectors. In order to perform the required measurements, the electromagnetic and hadronic calorimeters were both built with an acceptance range of $|\eta| < 4.9$, using different modules for different pseudorapidity regions. Each module was designed to match the physics requirements and radiation environment of its specific region, as described in section 3.3.3.

3.3.3 ATLAS Calorimeter Details

ATLAS electromagnetic calorimeters surround the tracking system and are composed of a barrel ($|\eta| < 1.475$) and two end-cap ($1.375 < |\eta| < 3.2$) units, residing in their own cryostat. A presampler detector is used to correct for electron and photon energy losses due to interactions with the tracking system, solenoid and cryostat walls. The presampler consists of an active liquid argon layer located in front of the electromagnetic calorimeters and covering the $|\eta| < 1.8$ region. All electromagnetic calorimeter modules are sampling liquid argon detectors with accordion-shaped kapton electrodes and lead absorber

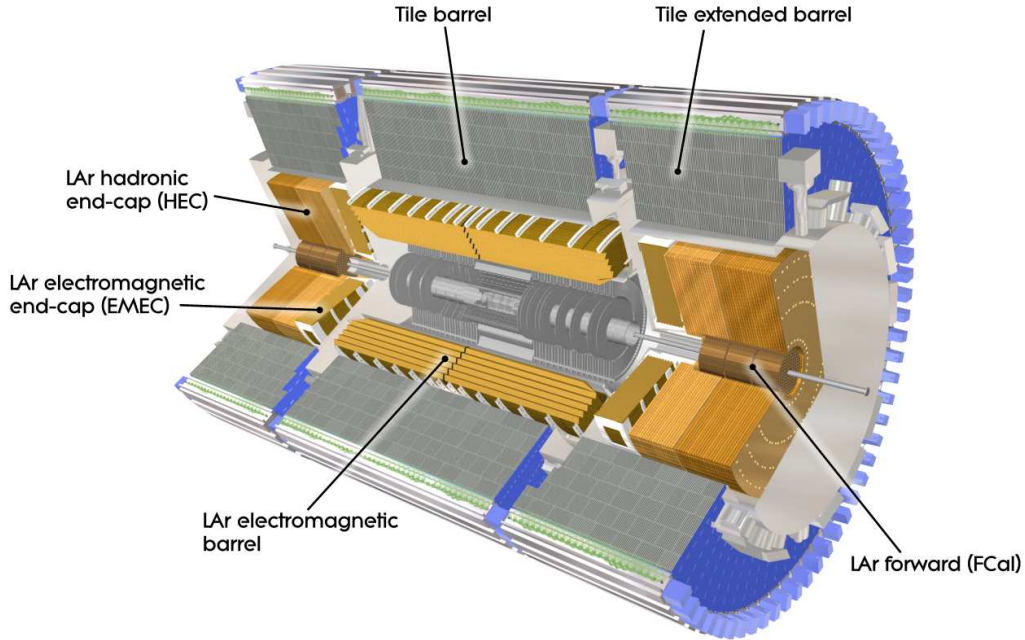


Figure 3–7: Layout of ATLAS electromagnetic and hadronic calorimeter systems. [24].

plates. The lead absorber plates' thickness has been optimized as a function of pseudorapidity to obtain the required energy resolution in each region. The accordion geometry of the electrodes and absorber plates ensures a gap-less azimuthal symmetry over the entire acceptance range. The electromagnetic calorimeters feature a fine granularity and three detector sampling layers in the η region matching the tracking system's acceptance range ($|\eta| < 2.5$) in order to provide precise electron and photon measurements. The more forward region ($|\eta| > 2.5$) is predominantly used to measure jet and missing energy. A coarser granularity and only two detector sampling layers are therefore sufficient to meet the physics requirements in this region of the detector. The total depth of the electromagnetic calorimeter is at least 22 and 24 radiation lengths in the barrel and end-cap units respectively, ensuring the containment of electromagnetic showers.

Enveloping the electromagnetic calorimeters are the hadronic calorimeters. The barrel hadronic calorimeter is composed of three cylindrical units: a central barrel ($|\eta| < 1.0$) and two extended barrels ($0.8 < |\eta| < 1.7$). These sampling calorimeters are divided in three layers and use plastic scintillator plates (or tiles) as active medium and steel plates as absorber. This technology provides the required radial depth and response while minimizing the cost of the detector. At larger rapidities ($1.5 < |\eta| < 3.2$), the hadronic end-cap calorimeter units are required to operate in a much higher radiation environment. The hadronic end-cap modules therefore use the radiation resistant liquid argon sampling technology with parallel copper plate absorbers of various thickness. These modules consist of two wheels, each sub-divided in two layers and sharing the same liquid argon cryostats as the electromagnetic end-cap calorimeters. Also sharing the same cryostats and covering the very forward region ($3.1 < |\eta| < 4.9$) of the detector are three forward calorimeter modules. The module closest to the interaction region is designed to detect electromagnetic particles, while the two other modules at higher z measure hadronic activity. All forward calorimeter modules consist of an array of electrodes embedded in a metal matrix. Each electrode is composed of a rod centred within a tube parallel to the beam axis. A small gap between the rod and tube is filled with liquid argon to be used as active medium. The width of the gap is kept constant by a radiation hard plastic fibre wound around the rod. The electromagnetic module uses copper as absorber material for the matrix, tube and the rod. The hadronic modules however use tungsten for the matrix and rods to provide the required containment and minimize the lateral spread of hadronic showers. Overall, the hadronic calorimeters' depth is greater than 9 interaction lengths throughout the acceptance region

of $|\eta| < 4.9$, ensuring the required jet energy and missing energy resolutions, as well as minimizing punch-throughs in the muon system.

The ATLAS calorimeters were initially calibrated using electron test beams. However, the ATLAS calorimeters are non-compensating, that is the calorimeters' response is different for electrons and hadrons. Reconstructed particle jets must thus be calibrated to account for this effect. These calibration techniques are discussed in section 4.3.2.

CHAPTER 4

Event Simulation and Reconstruction

The work presented in this thesis greatly depends on the ability to reconstruct particle jets from energy deposits in the ATLAS calorimeters. This reconstruction is performed by complex algorithms that account for detector effects to infer the kinematic properties of partons produced during the hard scattering of two protons. In order to compare observed quantities with theoretical predictions, full event simulations are commonly used. These simulations are often generated using a sequence of several computer programs, each configurable to reflect the intended process to be simulated or the detector configuration used.

An overview of the ATLAS simulation process and third-party event generators are presented in section 4.1. Section 4.2 describes official ATLAS simulated data sets used in this analysis. Finally, section 4.3 describes jet reconstruction and calibration procedures, central to the measurements performed in this analysis, as well as the reconstruction of primary vertices.

4.1 ATLAS Simulation Process

The ATLAS Monte-Carlo¹ simulation [35] of events is divided in three steps, the event generation, simulation, and digitization. The output of each step is used as input for the following one. At the end of the digitization process, the format of the simulated data is identical to that coming from the

¹ Monte-Carlo simulations rely on the pseudo-random generation of large quantities of events to study probability distributions of physical quantities.

real detector. The same trigger and reconstruction packages can then be run on both real and simulated data. This section gives a brief overview of each step of the event simulation process.

The event simulation sequence starts with the event *generation*, which produces a set of particles resulting from a single interaction with a vertex located at the geometrical centre of the detector. Events are generated to match a set of basic properties such as the centre-of-mass energy of the collision, energy ranges, and the process intended to be studied (e.g. two protons \rightarrow two jets). All the particles with lifetimes $c\tau < 10$ mm are immediately decayed by the generator, while particles with longer lifetimes are deemed stable.

Stable particles provided by the generator are propagated through a *simulation* of the detector. Interactions between the particles and the detector material are simulated using the GEANT4 [36,37] simulation toolkit. The simulation uses a detailed geometrical model of the ATLAS detector and a set of detector conditions retrieved from a central database. At this point, cuts can be applied to process only a subset of the available particles if needed.

Energy deposited in the sensitive regions of the detector is then *digitized* into voltages and currents, emulating the readout systems of the ATLAS detector. During the digitization process, detector noise is added, and the hard scattering event is superimposed with a configurable number of pile-up², beam

² Additional soft collisions from other protons in the same (in time) or neighbouring (bunch train) proton bunches.

halo³, beam gas⁴, and cavern background⁵ events. Finally the L1 trigger (described in section 3.2.4) algorithms are executed and the decision to record or reject the event is stored, but not applied.

Throughout the simulation process, *truth* information is stored to eventually be used to quantify the success of reconstruction algorithms. During the event generation, the decay history of each particle is stored as *truth* information, as are true tracks and decays of certain particles during the detector simulation process. Simulated data objects are created from the *truth* information during the digitization stage. These objects can be used to map the energy deposits in the detector to generated particles during the event reconstruction process.

The full simulation of events is computationally intensive and therefore requires the commitment of large computing resources. ATLAS uses a distributive computing model known as the World-wide LHC Computing Grid [38]. Tasks submitted to the grid, such as Monte-Carlo simulations, can be separated into many jobs depending on complexity, and executed at different production sites around the world, seamlessly to the user. The output files can easily be retrieved from the computing sites, or stored on the grid to be used by other users. Data and Monte-Carlo analysis jobs can also be performed on the grid, which is highly time-efficient due to the large reduction of

³ Machine-induced particles due to the scattering of beam protons on residual gas in the beam pipe and beam cleaning inefficiency.

⁴ Particles created by the collision of beam protons with residual gas molecules in the ATLAS cavity.

⁵ Particles present in the ATLAS cavern that can deposit energy in the detector.

data to be transferred (i.e. sending a job to the data, rather than retrieving the data locally to run a job).

4.1.1 Event Generators

This analysis relies on three LO event generators: PYTHIA [39], HERWIG/JIMMY [40–43] and ALPGEN [44]. The NLO event generator NLO-JET++, central to this analysis, is also described at the end of this section.

PYTHIA is optimized for processes involving the collision of two particles leading to the production of one or two outgoing particles (i.e. $2 \rightarrow 1$ or $2 \rightarrow 2$), and is generally regarded as very reliable for these processes. For final states consisting of two or more jets, the generator computes matrix element (see section 2.2.1) contributions for two outgoing partons, using the following hard scale parametrization:

$$Q^2 = \frac{m_3^2 \cdot c^2 + p_{T,3}^2 + m_4^2 \cdot c^2 + p_{T,4}^2}{2}, \quad (4.1)$$

where m is the mass, p_T is the transverse momentum, and the indices 3 and 4 refer to the outgoing partons. Using a parton shower and Lund string hadronization model [45], the two partons resulting from the hard scattering can then form two or more jets. The remainder of the partons that were not involved in the hard scattering, called *spectator* partons, also interact softly (i.e. at low energies compared to the hard scattering) and give rise to an *underlying event*. This non-perturbative effect is calculated by PYTHIA using a complex multiple interactions model [46].

The HERWIG event generator features many similarities with PYTHIA, including its optimization for $2 \rightarrow 1$ and $2 \rightarrow 2$ processes. HERWIG uses a different hard scale parametrization of

$$Q^2 = \frac{stu}{s^2 + t^2 + u^2} \quad (4.2)$$

to compute the hard scattering matrix elements, where s , t , and u are the Mandelstam variables⁶. However, the two generators differ mainly in their treatment of non-perturbative processes, especially for the hadronization process for which HERWIG uses a cluster-based model [40,41]. The cluster model is also applied to spectator partons leading to a very different modelling of the underlying event compared to PYTHIA. An additional library of routines called the JIMMY generator [42,43] is linked to the HERWIG generator, which can produce multiple parton scatterings in a single hadron-hadron collision. Since the parton density in hadrons increases as a function of the centre-of-mass energy, the likelihood of multiple scatterings occurring during a hadron-hadron collision also increases. The effects accounted for by the JIMMY generator are therefore potentially significant at the LHC energy regime.

The ALPGEN generator [44] differs from PYTHIA and HERWIG in that it uses full matrix element calculations to model hard scattering processes of two partons resulting in n -parton final states (i.e. $2 \rightarrow n$), where n ranges from two to six. The hard scale parametrization used for such processes is defined in ALPGEN as

$$Q^2 = \sum_{i=1}^{N_{partons}} \left(p_T^{(i)} \right)^2, \quad (4.3)$$

where $p_T^{(i)}$ is the transverse momentum of the i -th final state parton, and $N_{partons}$ is the total number of final state partons. The ALPGEN generator does not model final-state non-perturbative effects. Therefore, the parton-level output needs to be interfaced with a showering and hadronization algorithm, such

⁶ The Mandelstam variables are defined as $s = (p_1 + p_2)^2 = (p_3 + p_4)^2$, $t = (p_1 - p_3)^2 = (p_2 - p_4)^2$ and $u = (p_1 - p_4)^2 = (p_2 - p_3)^2$, where p_1 and p_2 are the four-momenta of the incoming partons, while p_3 and p_4 are the four-momenta of the outgoing partons.

as PYTHIA or HERWIG/JIMMY. Using the prescribed MLM matching procedure [44], matrix element and parton shower calculations can be combined. The procedure rejects events to avoid double-counting similar jet configurations produced by the matrix elements and parton showers. Because of its full matrix element calculations for events containing more than two and up to six jets, ALPGEN is expected to yield better approximations of final states with several well-separated hadronic jets than PYTHIA or HERWIG/JIMMY alone. This hypothesis was confirmed, for example, in the recent detailed study of multi-jet events at ATLAS [47].

Unlike all previously described event generators, NLOJET++ [48, 49] is used to produce NLO pQCD predictions of differential cross-sections. The generator achieves this by applying the Catani-Seymour subtraction scheme [49], which provides an efficient way to compute accurate NLO pQCD differential jet cross-section predictions. Conceptually, the algorithm introduces counter-terms in the NLO calculations to systematically cancel singularities arising from real contributions [49]. Using dimensional regularization techniques, double and single poles arising from the integration process of the counter terms can be made to cancel singularities arising from virtual contributions. With both real and virtual divergences removed, the NLO calculations can be performed numerically to predict jet production cross-sections.

In order to remove infrared and collinear divergences from the calculations, a jet clustering algorithm needs to be applied to the generated partons. To perform this task, we use the FASTJET [50] package, which supports several common clustering algorithms. However, the parton-level output of the tool cannot currently be interfaced with any parton showering or hadronization tool. Non-perturbative corrections therefore have to be *folded* into the NLO parton-level results. These corrections are based on LO calculations performed

with other event generators and parton showering/hadronization algorithms. The procedure to accomplish this is described in section 5.2.

4.2 ATLAS Simulated Data Sets

Various combinations of event generators, showering and hadronization algorithms are used to address the different needs of the analysis. Since the analysis strongly depends on calculations involving more than two jets, the analysis primarily relies on Monte-Carlo simulations computed from full matrix element calculations performed by ALPGEN. The ALPGEN+HERWIG/JIMMY combination has been shown to properly model multi-jet events at the LHC in ATLAS data [47], and is therefore used to compute all the correction factors required for this analysis. The agreement between these simulations and data was verified for all variables used in the analysis. Other simulated data sets are only used to estimate systematic uncertainties on correction factors computed from the ALPGEN+HERWIG/JIMMY sample. The complete list of all LO Monte-Carlo simulated data samples used in this analysis and their configuration is found in table 4-1.

All LO Monte Carlo samples used in this analysis were officially produced and validated by the ATLAS collaboration. Furthermore, all ALPGEN-based Monte-Carlo data sets were generated using the same initial set of stable particles, before showering and hadronization models are applied. The configuration used to generate this initial set of particles includes contributions from two to six final state parton configurations, and the five lightest quark flavours. Parton showering and hadronization algorithms can be *tuned* by adjusting several parameters in the description of underlying events, such that simulations better reflect observations in data. The list of underlying event tunes corresponding to each simulated data set is found in table 4-1.

Table 4–1: LO Monte-Carlo simulated data samples used and their configuration.

Event Generator	Parton Shower & Hadronization	Underlying Event	PDF	Pile-Up
ALPGEN	HERWIG/JIMMY	AUET1 [51]	CTEQ6L1 [52]	none
ALPGEN	HERWIG/JIMMY	AUET1 [51]	CTEQ6L1 [52]	in time
ALPGEN	HERWIG/JIMMY	AUET1 [51]	CTEQ6L1 [52]	bunch train
ALPGEN	PYTHIA	AMBT1 [53]	CTEQ6L1 [52]	none
PYTHIA	PYTHIA	AMBT1 [53]	MRST07 LO [54, 55]	none
PYTHIA	PYTHIA	Perugia2010 [56]	CTEQ5L [57]	none

In order to assess the effects of pile-up on the measurement, ALPGEN+HERWIG/JIMMY Monte-Carlo samples were generated with simulations of two types of pile-up contributions: in time and bunch train. In time pile-up samples include an average of two additional soft collisions per event originating from the same proton bunch crossing as the hard scattering. Bunch train pile-up samples include an average of 2.2 additional soft collisions per event and include effects from overlapping signals of neighbouring bunch crossings in the detector.

4.3 ATLAS Reconstruction

Although several common physics objects such as muons, photons, electrons and missing transverse energy are reconstructed by the default ATLAS reconstruction software, this analysis only relies on jets and primary vertices. The primary vertex of an event represents the ‘real’ interaction point where the hard scattering occurred, and its reconstruction is described in section 4.3.1. Jet reconstruction and energy calibration procedures are described in section 4.3.2.

4.3.1 Primary Vertex Reconstruction

ATLAS software reconstructs primary vertices based on reconstructed particle tracks from the tracking system. Reconstructed tracks satisfying the

following default set of criteria [58] are used in the primary vertex reconstruction:

- $p_T > 150$ MeV
- $|d_0| < 4$ mm
- $\sigma(d_0) < 5$ mm
- $\sigma(z_0) < 10$ mm
- at least four hits in the semiconductor tracker
- a total of at least six hits in the pixel and semiconductor trackers

where d_0 and z_0 represent the transverse and longitudinal impact parameters⁷ of tracks from the centre of the luminous region, while $\sigma(d_0)$ and $\sigma(z_0)$ are their respective uncertainties from the track fit. The vertex is found iteratively by first selecting a vertex seed corresponding to the maximum in the distribution of z coordinates of the tracks. The vertex is then reconstructed by fitting the tracks surrounding the seed. Tracks that are incompatible with the vertex by more than 7 standard deviations are used to seed a new vertex. This procedure is repeated until all the reconstructed tracks have been associated with a vertex.

4.3.2 Jet Reconstruction and Calibration

Jets can be reconstructed from individual particles or calorimeter energy deposits, however a common procedure must be defined to combine them into jet objects. This process is known as jet reconstruction, which can be divided into two tasks. The first task consists of determining a procedure to group nearby jet constituents⁸ into a single jet object. This task is handled by

⁷ The impact parameter is the distance between a reference point and the track's point of closest approach.

⁸ Truth particles or calorimeter energy deposits

the *jet algorithm*. The second task is to combine the four-momenta of all the selected constituents of the jets according to a *recombination scheme*, in order to estimate the energy and direction of the parton that created the jet. The jet definition and the ensuing reconstructed jet calibration used in this analysis are detailed in the following sections.

Jet Definition & Inputs

The jet algorithm used by ATLAS and throughout this analysis is called the *anti- k_t* algorithm [59, 60], as implemented by the FASTJET [50] package. The algorithm uses a clustering technique, whereby it iteratively combines pairs of objects according to their physical distance and transverse momenta. Each iteration, the algorithm computes the quantity $d_{i,j} = \min\left(\frac{1}{p_{T,i}^2}, \frac{1}{p_{T,j}^2}\right) \cdot \frac{\Delta R_{ij}}{R}$ for every object pair and $d_i = \frac{1}{p_{T,i}^2}$ for every object, where $p_{T,i}$ is the i -th object's transverse momentum, ΔR_{ij} is the physical distance between objects i and j as defined in section 3.2.1, and R is the algorithm's *resolution parameter*, set to 0.6 for this analysis. The algorithm then finds the minimum value of all these quantities and takes one of two possible actions: if the minimum value corresponds to a $d_{i,j}$ definition, then objects i and j are merged according to the chosen recombination scheme, otherwise the minimum quantity corresponds to a d_i definition, in which case the corresponding i -th object is declared a jet and removed from the recombination procedure for the next iteration. The algorithm continues this process until all input objects have been merged into jets. Conceptually, this procedure clusters less energetic objects around more energetic ones, resulting in an algorithm both infrared and collinear safe. The recombination scheme used by the jet algorithm is known as the *four-vector recombination scheme* [50], which essentially sums the four-momenta of the objects to be merged, such that energy and momentum are conserved.

Different input objects are used to construct jets throughout this analysis. *Parton jets* are created by applying the *anti- k_t* algorithm to generated partons, while *truth jets* are obtained from Monte-Carlo simulations by applying the same jet algorithm to simulated particles, after accounting for non-perturbative effects such as showering and hadronization. To reconstruct jets from data, topological clusters [61,62] are used as calorimeter input objects to the jet algorithm. Topological clusters are three-dimensional energy clusters built from calorimeter cells, following energy flow patterns in an attempt to reconstruct individual particle showers. This technique is designed to take full advantage of the fine granularity (segmentation) of the ATLAS calorimeters. The energy of a topological cluster is computed as the sum of the energy of the calorimeter cells it groups, while its direction is computed from the geometrical center of the detector, to the energy-weighted centre of the cluster. Both the energy and direction of reconstructed jets are then calibrated, as described in the next section. The ATLAS reconstruction process was found to be fully efficient for jet energies above 40 GeV [63,64].

Jet Calibration

Calorimeter cells used to construct topological clusters are calibrated at the electromagnetic (EM) scale based on test beams [65,66] and $Z \rightarrow ee$ data [67]. Topological clusters are therefore also evaluated at the electromagnetic scale. Reconstructed jets therefore need to be corrected for the different response of the calorimeter to hadrons and electrons. The energy and direction of reconstructed jets is also sensitive to pile-up, the location of primary vertex, energy lost in the detector material, etc. The calibration scheme [64] used to correct for these effects applies corrections to the jets based on their energy and pseudorapidity. The calibration process consists of four sequential steps: pile-up, vertex, jet energy and pseudorapidity corrections.

When additional protons interact during the same bunch crossing as the hard scatter being studied (i.e. pile-up), additional energy can be deposited in calorimeters. This additional energy can subsequently be merged with jets from the hard scattering, altering their energy and direction. In order to correct for this effect, a correction is calculated from minimum bias⁹ data as a function of the number of reconstructed primary vertices and jet pseudorapidity [64]. The calculated average energy due to pile-up is then subtracted from the measured calorimeter energy. This correction is performed first such that other calibrations do not have to account for additional collisions.

After pile-up effects are corrected, the origin of the jets needs to be adjusted. Up to this point, the origin of the jet was assumed to be at the geometrical centre of the detector. The four-vector of the jet is then recomputed using the primary vertex location as the origin of the jets [64]. If multiple primary vertices are found, the vertex with the highest sum of transverse momenta of tracks ($\sum_{tracks} p_T$) associated with it is used as the origin of the hard scatter.

Once the origin of the jets has been corrected to match the primary vertex location, their energy is calibrated to match the energy of Monte Carlo truth jets, thereby restoring the jets to their final hadronic energy scale or *jet energy scale* (JES). In order to compute the JES correction [68], Monte Carlo simulations are used. Isolated reconstructed jets are matched to isolated truth jets and the EM-scale jet energy response is calculated as $\mathcal{R}_{EM}^{jet} = \frac{E_{EM}^{jet}}{E_{truth}^{jet}}$ in bins of truth jet energy and pseudorapidity. The final JES correction is obtained in bins of pseudorapidity by fitting the average jet energy response as a function

⁹ Minimum bias events are randomly selected events showing evidence that a collision occurred.

of the average jet EM-scale energy. The calibration can then be applied to each reconstructed jet individually, and account for

- the difference in calorimeter response between electrons and hadrons
- energy losses in dead material
- energy losses due to particles not contained by the calorimeter
- energy deposits included in truth jets but not in reconstructed jets
- energy losses due to clustering and jet reconstruction

The last correction applied to reconstructed jets is a pseudorapidity correction to account for a bias cause by poorly instrumented regions of the calorimeter. In these regions, the reconstructed energy of topological cluster constituents is smaller than in the better instrumented regions, which can shift the calculated centre of the cluster. The correction factor is calculated taking the difference in pseudorapidity between the truth and calibrated jets. This difference is then parametrized as a function of calibrated jet energy and uncalibrated jet pseudorapidity. This results in a very small ($\Delta\eta < 0.1$) correction to the direction of calibrated jets [64].

CHAPTER 5

Theoretical Predictions of $R_{3/2}$

Theoretical predictions used to measure the strong coupling α_S are computed from pQCD at NLO precision with NLOJET++. However, NLOJET++ predictions cannot presently be interfaced with hadronization and showering algorithms. Hence, LO pQCD Monte Carlo simulation samples are also used to *fold* non-perturbative QCD corrections into NLO predictions. The NLOJET++ predictions are detailed in section 5.1, while section 5.2 details the non-perturbative QCD corrections.

5.1 NLO Predictions of $R_{3/2}$

NLO predictions are generated with NLOJET++, using a hundred million simulated events for each jet multiplicity, as well as five quark flavours so as to be compatible with LO simulations listed in table 4-1. A thorough analysis of NLO predictions obtained from NLOJET++ is performed to determine the optimal parameters to be used for the measurement of the strong coupling using the inclusive three- to two-jet cross-section ratio. To ensure the validity of the results presented in this document, several key observations were compared with results obtained by other members of the ATLAS collaboration using NLOJet++, results obtained by theorists external to the collaboration using different NLO simulation software, results obtained by the author of NLOJET++, and published ATLAS results performed with NLOJET++ [47]. All comparisons were found to agree with results and observations presented in this section.

In order to observe the running of the coupling, the measurement of the strong coupling constant is performed as a function of the hard scale Q of

events. For multi-jet events, the hard scale can be approximated using a quantity computed entirely from the final state jets of an event, i.e. a *jet observable*. Hence, the renormalization and factorization scales used by NLO-JET++ to compute the two- and three-jet differential cross-sections are defined as $\mu_R = \mu_r X$ and $\mu_F = \mu_f X$, where the μ_r and μ_f factors are respectively known as the renormalization and factorization scale factors, and X is the jet observable used to parametrize the hard scale of an event.

The observed cross-section of a QCD process in nature does not depend on the unphysical parameters that are the renormalization and factorization scales. If an infinite number of terms could be computed in the pQCD expansion, any dependence of the results on these scales would disappear. However, since the perturbation expansion used by NLOJET++ is truncated at a finite order, the cross-section predictions it generates exhibit residual dependencies on both the renormalization and factorization scales. A procedure known as the *principle of minimal sensitivity* [69] is therefore applied to minimize this residual dependence on the scales, in order to obtain the most stable and accurate pQCD predictions in each bin of the jet observable X . To that end, differential cross-section predictions are computed for a broad range of renormalization and factorization scale factors.

During the NLOJET++ event generation process, each permutation of renormalization and factorization scales yields a different event weight. The event kinematics remain the same for each scale configuration so as to avoid statistical fluctuations when comparing them. In each X -bin, the resulting NLO two- and three-jet differential cross-section's dependency on μ_r and μ_f typically features a saddle point, as indicated by a white 'X' in figures 5–1 (a) and (b). The saddle point location corresponds to the μ_r and μ_f configuration which minimizes the residual dependencies of the calculation to the

renormalization and factorization scales within the kinematic range of the corresponding bin. The scale factor values μ_r and μ_f at the saddle point location for a particular bin of an observable X are therefore used to compute NLO-Jet++ predictions for the remainder of the analysis for the specific bin and jet observable studied. This procedure is applied independently to both the inclusive two- and three-jet predictions before they are combined to obtain the inclusive ratio according to equation (2.10).

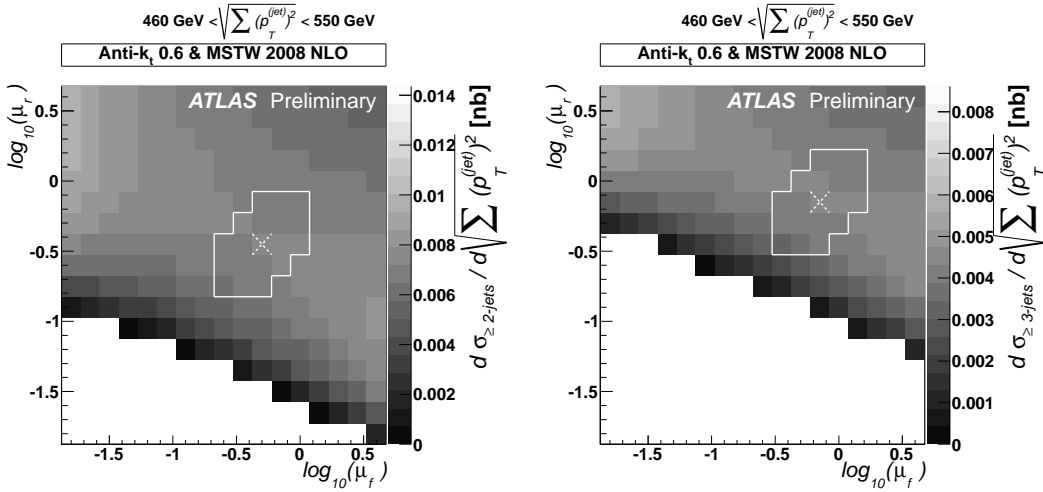


Figure 5–1: Example of two- (a) and three-jet (b) differential cross-section computed using NLOJET++ for several renormalization (μ_r) and factorization (μ_f) scale factors, for events with $\sqrt{\sum_{i=1}^{N_{jets}} \left(p_T^{(i)}\right)^2}$ values between 460 and 550 GeV. The saddle point is indicated by a dashed cross while the solid line defines the $\mu_{r,f}$ region scanned while estimating the scale uncertainty on the cross-section predictions. All jets are built from partons and satisfy $p_T^{(jet)} > 40$ GeV and $|\eta^{(jet)}| < 2.8$; all events satisfy $p_T^{(leading\ jet)} > 60$ GeV.

Several hard scale parametrization options are investigated in section 5.1.2. The merit of each jet observable is based on the resulting inclusive three- to two-jet production ratio's sensitivity to the strong coupling, as well as the size of theoretical uncertainties associated with the PDFs, renormalization and factorization scales' stability. The techniques to compute these theoretical uncertainties are detailed in the following subsection.

5.1.1 Theoretical Uncertainties

Scale Uncertainty

Once renormalization and factorization scale values are found for a jet observable's bin, an uncertainty associated with the scales' stability is estimated. This theoretical scale uncertainty is calculated by varying the renormalization and factorization scales independently by factors between $1/2$ to 2 around the bin's saddle point configuration, or

$$\frac{1}{2}\mu_r^{(saddle)} \leq \mu_r \leq 2\mu_r^{(saddle)} \text{ and} \quad (5.1)$$

$$\frac{1}{2}\mu_f^{(saddle)} \leq \mu_f \leq 2\mu_f^{(saddle)}, \quad (5.2)$$

where $\mu_r^{(saddle)}$ and $\mu_f^{(saddle)}$ are respectively the renormalization and factorization scale factors corresponding to the saddle point location. However, in order to avoid large logarithms of μ_R^2/μ_F^2 in the NLO calculations or accidental cancellations between μ_F and μ_R , we require the additional constraint [70]

$$\frac{1}{2}\mu_r < \mu_f < 2\mu_r. \quad (5.3)$$

to be applied. These requirements are illustrated in figures 5–1(a) and (b) by solid lines delimiting an area in the (μ_f, μ_r) plane. The positive and negative scale uncertainties on the differential cross-section predictions are computed as the maximum difference between the value of the cross-section at the saddle point and the cross-section values within the area delimited by the solid line. This procedure is repeated for each jet observable bin and each jet multiplicity sample. These uncertainties on the two- and three-jet cross-sections are propagated to the calculation of the inclusive three- to two-jet cross-section ratio bin-by-bin, using standard partial derivatives error propagation techniques.

PDF Uncertainty

NLOJet++ is configured to use the MSTW 2008 NLO [55] PDF set with 90% confidence-limit errors. The reason for this choice lies in the PDF sets available for α_S studies. The MSTW 2008 PDF set for α_S studies [71] includes PDFs for $0.110 \leq \alpha_S(M_Z) \leq 0.130$ while the CTEQ6.6 set for α_S studies [72] is limited to the range $0.116 \leq \alpha_S(M_Z) \leq 0.120$. NLOJET++ simulated samples are generated for each $\alpha_S(M_Z)$ value of the MSTW 2008 PDF set. During that process, the $\alpha_S(M_Z)$ value is evolved internally through LHAPDF [73] interfaces for each event using two-loop renormalization group equation approximations in the $\overline{\text{MS}}$ renormalization scheme [5, 11]. The theoretical PDF uncertainty on the calculated cross-sections is obtained by computing event weights with each of the twenty MSTW 2008 eigenvector¹ PDF sets, each set composed of two members corresponding to a positive or negative variation in the default PDF. Cross-section predictions obtained from all PDF variations are computed using the same generated events so that the comparison of results between variations only reflects changes in the PDFs and are independent of statistical fluctuations. The overall asymmetrical uncertainty on the predicted inclusive three- to two-jet production ratio is computed bin-by-bin using equations [74]

$$\Delta R_{3/2}^{+PDF}(X) = \sqrt{\sum_{i=0}^N \left[\max \left(R_{3/2}^{+i}(X) - R_{3/2}^0(X), R_{3/2}^{-i}(X) - R_{3/2}^0(X), 0 \right) \right]^2}, \quad (5.4)$$

¹ The PDFs are fitted to data by diagonalizing a 20x20 matrix, corresponding to the twenty free parameters of the fit. The resulting eigenvectors correspond to a linear combination of PDF parameters that can be used to estimate the success of the fit.

$$\Delta R_{3/2}^{-PDF}(X) = \sqrt{\sum_{i=0}^N \left[\max \left(R_{3/2}^0(X) - R_{3/2}^{+i}(X), R_{3/2}^0(X) - R_{3/2}^{-i}(X), 0 \right) \right]^2}, \quad (5.5)$$

where $R_{3/2}^{\pm i}(X)$ is the three- to two-jet inclusive ratio's prediction for the jet observable X computed from the i -th \pm eigenvector, $R_{3/2,0}(X)$ is the same quantity computed from the PDF set's central value, N is the total number of eigenvector sets, and $\Delta R_{3/2}^{\pm PDF}(X)$ is the $\pm ve$ PDF uncertainty on $R_{3/2}^0(X)$.

5.1.2 Hard Scale Parametrization Selection

For the purpose of measuring a value of α_S , three jet observables are considered to parametrize an event's hard scale: the scalar sum of all jet momenta H_T , the leading jet transverse momentum, and Q' defined as

$$Q' = \sqrt{\sum_{i=1}^{N_{jets}} \left(p_T^{(i)} \right)^2}, \quad (5.6)$$

where $p_T^{(i)}$ is the i -th parton-jet's transverse momentum, and N_{jets} is the total number of parton-jets present in the event. The inclusive three- to two-jet production ratio is also calculated as a function of inclusive jet transverse momentum using the leading jet transverse momentum as hard scale parametrization. For a specific jet multiplicity, the same event kinematics are used to compute predictions of the inclusive three- to two-jet production ratio for all jet observables considered.

The saddle point optimization of the renormalization (μ_r) and factorization (μ_f) scale factors is performed independently for each bin of the jet observable considered, hard scale parametrization candidate, and jet multiplicity. The chosen values of μ_r and μ_f are displayed in figures 5–2 and 5–3 for each jet observable studied, and for the inclusive two-jet and three-jet cross-section predictions, respectively. As results indicate, the saddle point location is fairly constant for all inclusive three-jet cross-section predictions. However, much

larger variations are observed in the inclusive two-jet cross-section predictions when the H_T observable or the leading jet transverse momentum are used as hard scale parametrization. Both the Q' and inclusive jet transverse momentum variables show similar stabilities in the location of the saddle point. As the predicted value of the strong coupling is strongly dependent on the renormalization scale, the renormalization scale factor should be as insensitive as possible to variations of the chosen observable in order to avoid any bias on the measurement of the strong coupling. In that respect, figures 5–2 and 5–3 suggest that both the inclusive jet transverse momentum and the Q' observable are suitable observables for the purpose of this analysis.

Another factor to be considered in the choice of hard scale parametrization is the inclusive three- to two-jet production cross-section ratio's sensitivity to the strong coupling constant's value. This sensitivity is qualitatively evaluated by comparing NLO predictions of the inclusive ratio computed with different values of $\alpha_S(M_Z)$. The results are shown in figure 5–4 for the four jet observables considered for the analysis. Results indicate that both the H_T and leading jet transverse momentum variables are only sensitive to changes in the strong coupling below ~ 400 GeV, making them unsuitable for this analysis. On the other hand, both the inclusive jet transverse momentum and the Q' observables feature very similar sensitivities to the strong coupling. Hence, the inclusive ratio's dependence on the strong coupling's value suggests that both the inclusive jet transverse momentum and Q' observables are suitable candidates to perform this analysis.

The last step in the selection of a hard scale parametrization and independent variable for the inclusive three- to two-jet production cross-section ratio is to investigate the relative size of the inclusive ratio's theoretical uncertainties.

The total theoretical uncertainty is calculated from the statistical uncertainties due to the finite simulated sample sizes, as well as uncertainties associated with variations in PDFs and scales, all of which are added in quadrature in each bin of each jet observable. Theoretical uncertainties are computed as described in section 5.1.1 and the resulting ratio distributions are shown in figure 5–5 with total theoretical uncertainties. According to figure 5–5, the Q' variable features on average the smallest total uncertainty. The relative size of each individual source of uncertainty is displayed in figure 5–5, which reveals that the total NLO theoretical uncertainty is entirely dominated by the scale uncertainty for all observables. The investigation of theoretical uncertainties therefore suggests that the Q' variable would be better suited to perform the intended measurement than other variables investigated.

Although results obtained using the inclusive jet transverse momentum as observable yields very similar results as the Q' observable, additional studies would be required to ensure that cross-section predictions computed using a hard scale parametrization based on an individual jet as opposed to an event’s overall kinematics provides an adequate description of experimental data. Therefore, the Q' jet observable, as defined in equation (5.6), is used as hard scale parametrization in NLO calculations, and as independent or binning variable when computing the inclusive three- to two-jet ratio.

5.2 Non-Perturbative QCD Corrections

NLO predictions do not include showering or hadronization effects; they are generated at the parton-level. To be compared to measurements performed in data, NLO predictions must be evolved to the particle (truth) level. Since NLOJET++ predictions cannot be interfaced with parton shower or hadronization algorithms, a correction factor is applied to the predicted

inclusive three- to two-jet production ratio, which accounts for these non-perturbative QCD effects. This *folding* of non-perturbative effects into NLO predictions relies on LO Monte-Carlo simulations including leading-logarithmic parton showering effects from HERWIG/JIMMY and PYTHIA.

The QCD non-perturbative correction factor is computed for each bin of the inclusive three- to two-jet ratio distribution. To that end, the ratio distribution is computed from parton and truth (i.e. particle) jets. The correction factor corresponding to each Q' bin $C_{non-pert}(Q')$ is then computed as

$$C_{non-pert}(Q') = \frac{R_{3/2}^{particle, UE}(Q')}{R_{3/2}^{parton, no UE}(Q')}, \quad (5.7)$$

where $R_{3/2}^{particle, UE}(Q')$ is the inclusive three- to two-jet ratio computed from particle-jets with underlying event contributions, and $R_{3/2}^{parton, no UE}(Q')$ is the same ratio computed from parton-jets without taking into account any underlying event contribution. Particle-jets are built from truth information available in Monte-Carlo simulations, while parton-jets are built directly from the events' partons, including parton showering but not hadronization effects. NLO predictions of the inclusive ratio are corrected by multiplying each bin's prediction by the corresponding non-perturbative QCD correction factor².

The resulting non-perturbative QCD correction factors are shown in figure 5–6(a) with statistical uncertainties derived from the Monte-Carlo simulated samples involved in the calculations. The larger correction factors observed in the first two to three bins of the distribution are caused by the

² This procedure is mathematically equivalent to folding non-perturbative effects in the inclusive two- and three-jet cross-section distributions individually, then calculating the inclusive three- to two-jet cross-section ratio.

presence of underlying event alone. Removing the underlying event contributions from the folding correction factor reveals a nearly constant factor for all bins.

The ALPGEN+HERWIG/JIMMY Monte-Carlo sample listed in section 4.2 is used to compute the central value of the non-perturbative QCD correction factor due to the availability of parton-level information, as well as for consistency with the rest of the analysis. The denominator, however, is computed from the parton-level information used to generate the ALPGEN+HERWIG/JIMMY Monte-Carlo sample, without any underlying event contributions. Both the numerator and denominator are therefore based on the same set of matrix element calculations from ALPGEN. An uncertainty associated with choosing HERWIG/JIMMY to model hadronization and underlying events is estimated in subsection 5.2.1. The final corrected ratio prediction is shown in figure 5–6(b), and individual Q' bin values are tabulated in table 5–1, providing detailed uncertainty contributions from each source.

5.2.1 Uncertainty on Non-Perturbative QCD Correction

In order to estimate the uncertainty on the non-perturbative correction factors due to different hadronization and underlying event models, referred to as *Monte-Carlo modelling*, the $R_{3/2}^{particle,UE}$ distribution is calculated using an ALPGEN+PYTHIA Monte-Carlo sample. The resulting distribution is found in figure 5–7(a). For each bin of the $R_{3/2}^{particle,UE}$ distribution, the variation in central value between the ALPGEN+PYTHIA and ALPGEN+HERWIG/JIMMY result is used as a symmetric uncertainty on $R_{3/2}^{particle,UE}$ due to the choice of hadronization and underlying event models. This uncertainty is propagated to the unfolded inclusive three- to two-jet ratio, as shown in figure 5–7(b). The overall uncertainty due to non-perturbative effects on the NLO predictions is shown to be approximately 8% for the entire Q' range considered. Values

of the non-perturbative correction uncertainty on the corrected theoretical predictions of the ratio are tabulated in table 5-1.

Table 5-1: Detailed uncertainty contributions to the inclusive ratio computed from NLOJET++ simulations, using $\alpha_S(M_Z) = 0.12018$. All the results are corrected to the particle level. Results are tabulated as a function of Q' and are computed with all analysis cuts described in section 6.1 applied.

Q' bin range (GeV)	Corrected $R_{3/2}$	Sources of uncertainty	
		NLOJET++ statistics	ALPGEN statistics
100- 120	0.171	± 0.004	± 0.005
120- 150	0.296	± 0.004	± 0.007
150- 180	0.391	± 0.007	± 0.008
180- 230	0.442	± 0.007	± 0.008
230- 280	0.519	± 0.006	± 0.009
280- 330	0.545	± 0.005	± 0.009
330- 390	0.571	± 0.006	± 0.009
390- 460	0.602	± 0.007	± 0.008
460- 550	0.617	± 0.012	± 0.009
550- 700	0.631	± 0.005	± 0.010
700-1000	0.659	± 0.005	± 0.016
1000-1500	0.619	± 0.013	± 0.031

Q' bin range (GeV)	Scale	Sources of uncertainty	
		PDF	Monte-Carlo Modelling
100- 120	+0.009 -0.013	± 0.002	± 0.015
120- 150	+0.012 -0.046	± 0.002	± 0.019
150- 180	+0.034 -0.049	± 0.004	± 0.027
180- 230	+0.041 -0.085	± 0.003	± 0.035
230- 280	+0.028 -0.092	± 0.004	± 0.039
280- 330	+0.029 -0.046	± 0.005	± 0.035
330- 390	+0.033 -0.049	± 0.006	± 0.046
390- 460	+0.034 -0.052	± 0.006	± 0.035
460- 550	+0.069 -0.125	± 0.006	± 0.042
550- 700	+0.038 -0.072	± 0.006	± 0.045
700-1000	+0.047 -0.067	± 0.008	± 0.050
1000-1500	+0.049 -0.118	± 0.009	± 0.013

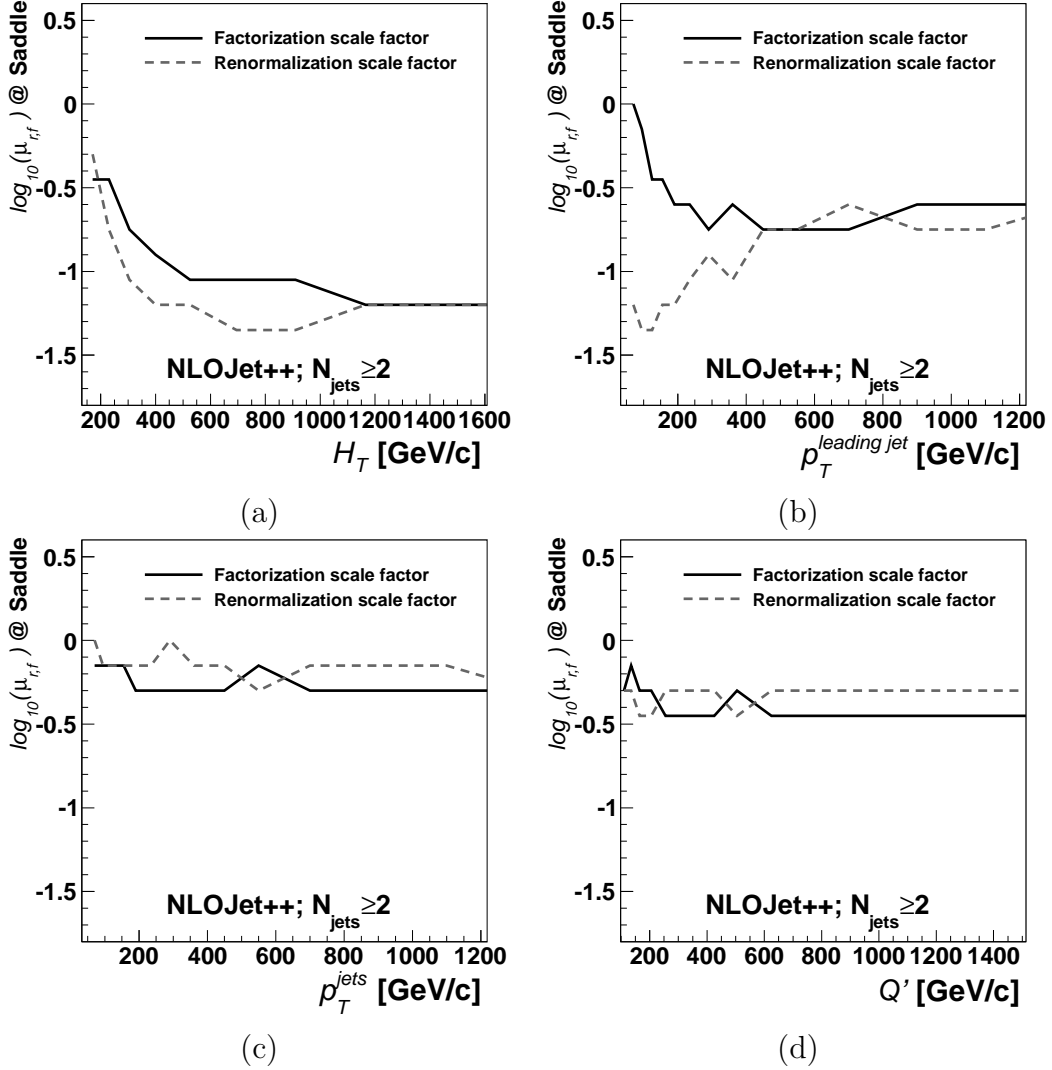


Figure 5–2: The two-jet optimized renormalization (μ_r) and factorization (μ_f) scale factors for the H_T (a), leading jet p_T (b), inclusive jet p_T (c), and Q' (d) observables. The calculations are performed consistently using the jet observable as the hard scale parameterization. All jets are built from partons and satisfy $p_T^{(jet)} > 40$ GeV and $|\eta^{(jet)}| < 2.8$; all events satisfy $p_T^{(leading\ jet)} > 60$ GeV.

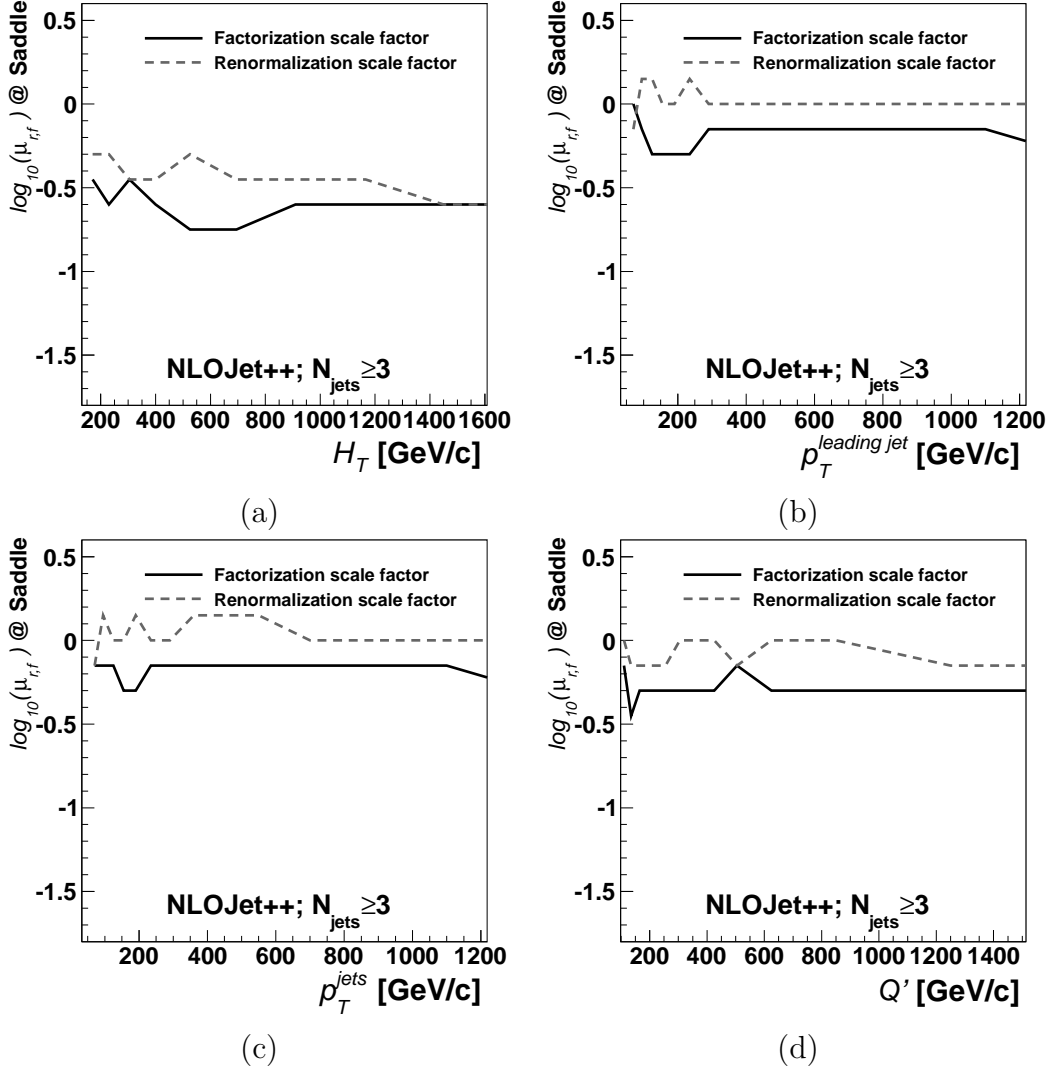


Figure 5-3: The three-jet optimized renormalization (μ_r) and factorization (μ_f) scale factors for the H_T (a), leading jet p_T (b), inclusive jet p_T (c), and Q' (d) observables. The calculations are performed consistently using the jet observable as the hard scale parameterization. All jets are built from partons and satisfy $p_T^{(jet)} > 40$ GeV and $|\eta^{(jet)}| < 2.8$; all events satisfy $p_T^{(leading\ jet)} > 60$ GeV.

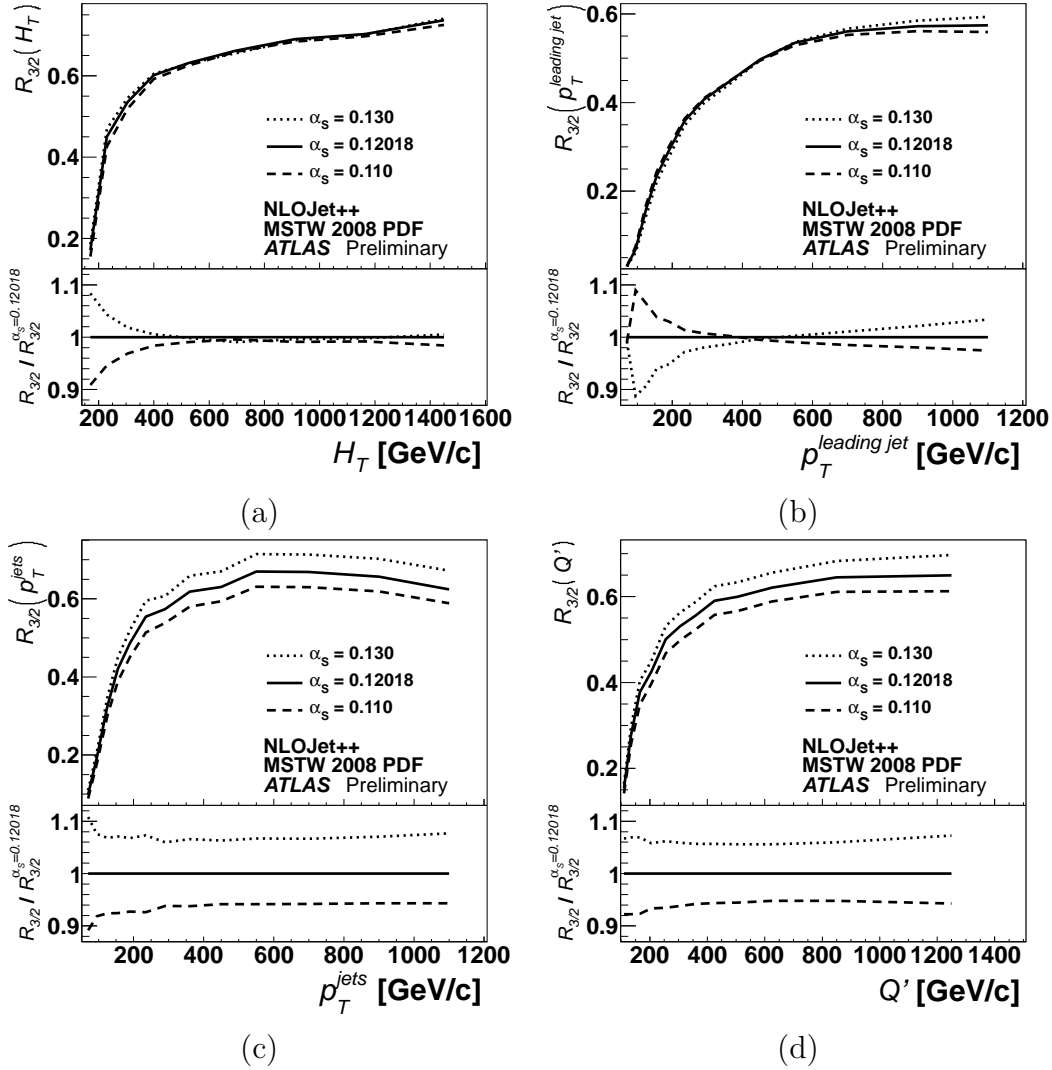


Figure 5–4: Sensitivity of NLO predictions of inclusive three- to two-jet ratio $R_{3/2}$ to variations of the strong coupling constant α_S . Predictions are shown as a function of H_T (a), leading jet p_T (b), inclusive jet p_T (c), and Q' (d) observables. The calculations are performed consistently using the jet observable as the hard scale parameterization. All jets are built from partons and satisfy $p_T^{(jet)} > 40$ GeV and $|\eta^{(jet)}| < 2.8$; all events satisfy $p_T^{(leading\ jet)} > 60$ GeV.

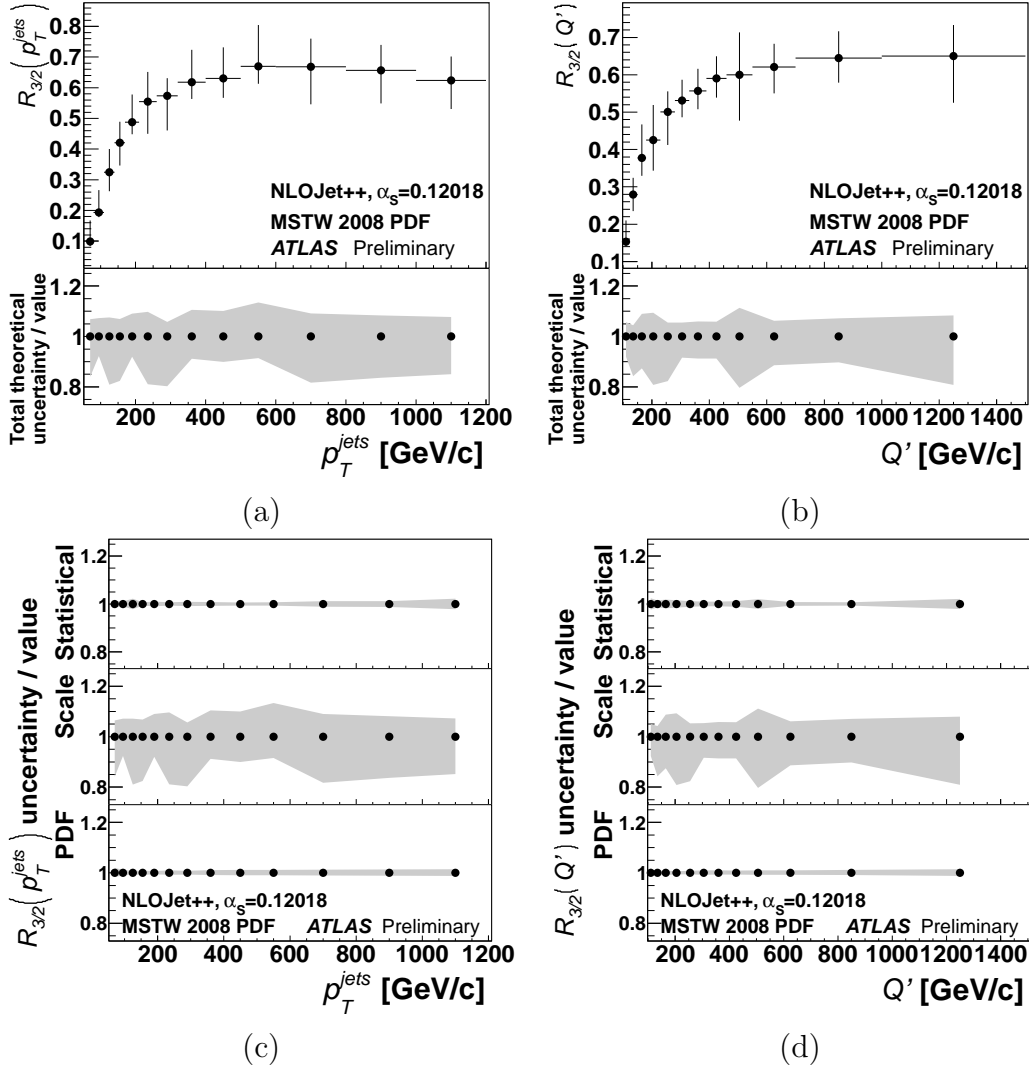


Figure 5-5: NLOJET++ predictions of the three- to two-jet inclusive ratio $R_{3/2}$ and total theoretical uncertainty as a function of inclusive jet p_T (a) and Q' (b) observables. Contributions to the theoretical uncertainties are presented for both observables in figures (c) and (d) respectively. The calculations are performed consistently using the jet observable as the hard scale parameterization. All jets are built from partons and satisfy $p_T^{(jet)} > 40$ GeV and $|\eta^{(jet)}| < 2.8$; all events satisfy $p_T^{(leading\ jet)} > 60$ GeV.

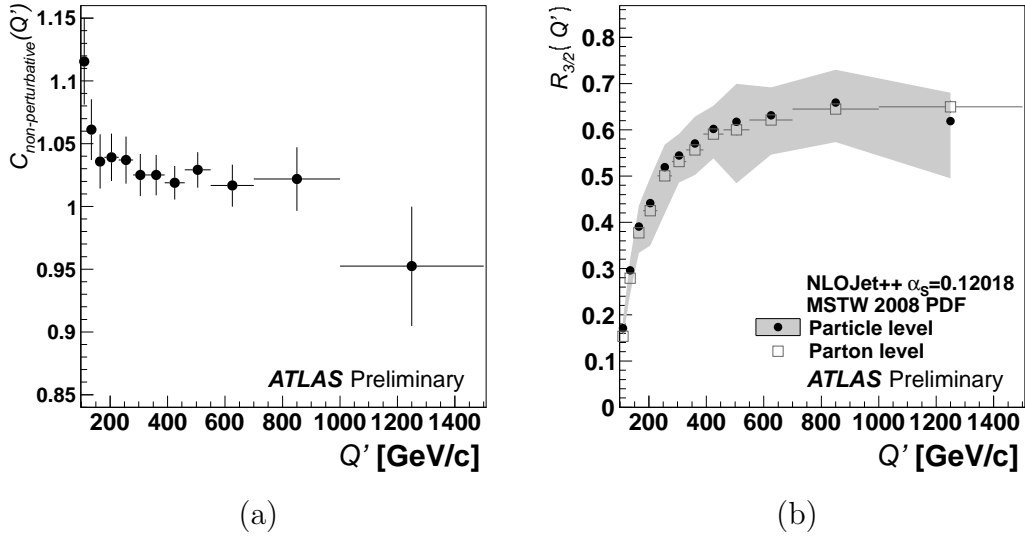


Figure 5–6: (a) Values of the correction factor for non-perturbative effects as a function of Q' . Results are obtained from ALPGEN+HERWIG/JIMMY Monte-Carlo samples and only include statistical uncertainties. (b) Comparison of three- to two-jet production ratio prediction before and after correcting to the particle-level. Predictions are evaluated at $\alpha_S = 0.12018$, and the parton-level results include only NLOJET++ statistical uncertainties (smaller than the marker size) while particle-level results include all uncertainties listed in table 5–1. Results are shown as a function of Q' . Jets are built from partons or truth particles and satisfy $p_T^{(jet)} > 40$ GeV and $|\eta^{(jet)}| < 2.8$; all events satisfy $p_T^{(leading\ jet)} > 60$ GeV.

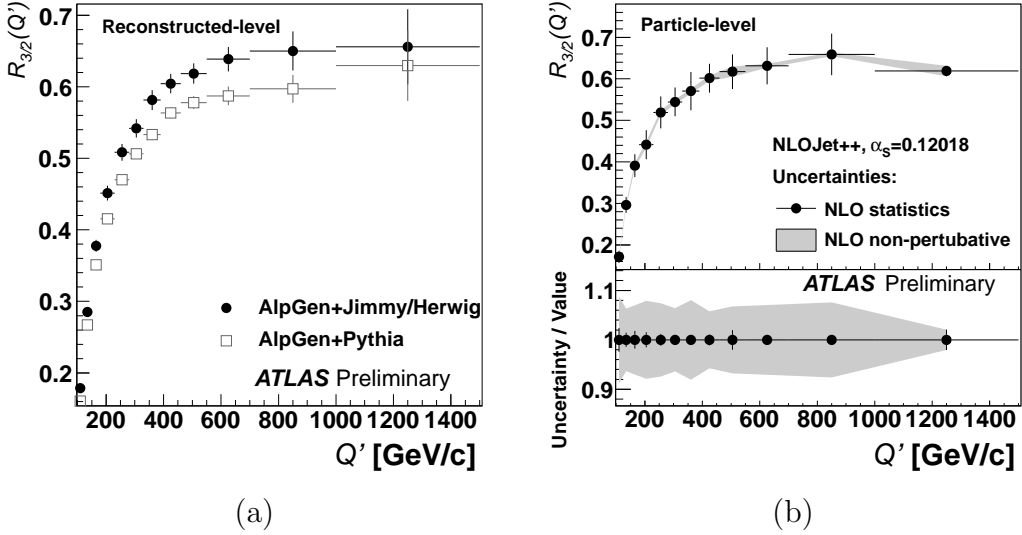


Figure 5–7: (a) Inclusive ratios computed from ALPGEN+PYTHIA and ALPGEN+HERWIG/JIMMY to determine the uncertainty in NLO correction due to showering, hadronization and underlying event models. (b) Three- to two-jet cross-section ratio corrected for non-pQCD effects (particle-level) as function of Q' , showing the size of the uncertainty associated to the non-pQCD correction applied. Results are shown as a function of Q' with $\alpha_S = 0.12018$. Jets are built from partons or truth particles and satisfy $p_T^{(jet)} > 40$ GeV and $|\eta^{(jet)}| < 2.8$; all events satisfy $p_T^{(leading\ jet)} > 60$ GeV.

CHAPTER 6

Data Measurement of $R_{3/2}$

Events used to measure the inclusive three- to two-jet ratio were recorded by the ATLAS detector in 2010 at a centre-of-mass energy of 7 TeV. This data is divided in nine data-taking periods, commonly referred to in alphabetical order as periods A through I. Each period corresponds to slightly different running conditions as the LHC luminosity was increased and the ATLAS systems became better understood.

This chapter first describes the selection criteria for events used in the measurement of the inclusive three- to two-jet production ratio, followed by a description of the unfolding process used to correct the reconstructed results to the particle-level. The last section of this chapter details the different systematic uncertainties affecting the measurement of the ratio from data.

6.1 Event Selection

Events used for the analysis first need to be filtered to remove any data collected while parts of the detector or the collider were not operating under nominal conditions. In order to avoid jet reconstruction inefficiencies and pile-up contamination within these events, primary vertex and jet selection criteria are also applied. These event and jet selection criteria are detailed in section 6.1.1. All events used in this analysis are also required to fulfil the trigger selection requirements described in section 6.1.2.

6.1.1 Event & Jet Selection Criteria

The quality of data recorded by the ATLAS detector is continuously monitored. All of the data used in this analysis has been validated by the ATLAS data quality group, and a standard set of criteria is used to ensure that all

detector subsystems were operating within normal parameters during data-taking. The total integrated luminosity used for this analysis, after the application of all data quality requirements, is approximately 37.6 pb^{-1} .

Events used by the analysis include different amounts of pile-up depending on the data-taking period. Pile-up introduces additional softer collisions in events, which can produce additional low energy jets and change the jet multiplicity of the event. In order to reduce the effect of pile-up, only events containing exactly one primary vertex with at least five associated tracks are analyzed. Furthermore, only events containing at least one reconstructed jet with transverse momentum greater than 60 GeV are used. This requirement ensures that all events used in the analysis have a greater than 99% chance of satisfying the lowest trigger criteria defined in section 6.1.2.

Only jets with transverse momentum of at least 40 GeV are counted in the analysis, which guarantees that the jet reconstruction is fully efficient [63, 64], while avoiding large NLO theoretical uncertainties and minimizing statistical uncertainties on the measurement. Jets are also required to be within the pseudorapidity range $|\eta| < 2.8$ so as to reduce the NLO scale uncertainty, which is the dominant NLO theoretical uncertainty. These requirements also contribute to the reduction of pile-up uncertainty in the final measurement of the strong coupling constant α_S .

In addition to the general selection criteria described above, the following jet quality requirements are only applied in data. They cannot be applied to Monte-Carlo simulations as the jet variables involved are not properly modelled. Reconstructed jets which are likely affected by energy spikes in the hadronic end-cap calorimeter can be identified by either of the following requirements:

- Over 50% of the jet energy is deposited in the hadronic end-cap and the liquid argon jet quality¹ for the hadronic end-cap cells is greater than 0.5.
- The absolute value of the negative energy² contribution is greater than 60 GeV.

These jets are labelled as *bad* and are excluded from the analysis. A jet with over 95% of its energy originating from the electromagnetic calorimeter and a liquid argon jet quality greater than 0.8 is likely affected by coherent noise in the electromagnetic calorimeters, and is therefore also classified as a bad jet. Finally, another class of bad jets, likely resulting from past collisions and cosmic backgrounds, is identified by any of the following criteria

- The jet time, computed from the weighted cells' time, is more than 25 ns away from the event time.
- More than 95% of the jet energy is deposited in the electromagnetic calorimeter, the jet charged fraction³ is less than 0.05 and the jet $|\eta|$ is less than 2.0.
- Less than 5% of the jet energy is deposited in the electromagnetic calorimeter and the jet $|\eta|$ is greater or equal to 2.0.

¹ Liquid argon jet quality variable is the fractional number of liquid argon cells in the jet with *Q-factor* above a specific threshold. The *Q-factor* measures the difference between the predicted and measured pulse shape used to reconstruct the cell energy.

² Anomalies in the analog-to-digital conversion systems can cause the measurement of a calorimeter cell's energy to be negative.

³ The jet charged fraction is defined as the ratio of the sum of the transverse momentum of the tracks associated to the jet divided by the calibrated jet's transverse momentum.

- The fraction of the jet energy deposited in a single calorimeter layer is greater than 0.99 and the jet $|\eta|$ is less than 2.0.

Another category of jets is known as *ugly* jets. Such jets are built from energy deposits in regions where the energy measurement is not accurate. A jet is therefore labelled as *ugly* if more than 50% of its energy (at the electromagnetic scale) comes from the transition region between the tile and end-cap calorimeters, or if more than 50% of its energy comes from dead cells (with cell correction based on neighbouring cells and assuming the same energy density). Ugly jets, like bad jets, are ignored during the analysis; however the event can still be accepted if two or more of the remaining jets satisfy all of the kinematic and quality cuts.

6.1.2 Trigger Selection

As described in section 3.2.4, several trigger chains, representing different sets of criteria, are used during data-taking to select events to be recorded. Trigger chains are designed to record specific types of events and their efficiency can vary depending on the type of event investigated. Not accounting for these inefficiencies can lead to a misrepresentation of the relative probability that different types of processes occur in nature. Only events recorded by single-jet triggers are used in this analysis. The efficiency of each trigger selection is studied, and one single-jet trigger chain is chosen for each Q' bin according to criteria described in the remainder of this section.

During data taking periods A through F, only the first level (L1) of the trigger selection process was rejecting events. During the later periods G through I, rejection based on the second trigger level (L2) was enabled. Table 6–1 lists the single-jet trigger items enabled for each data-taking period. The ATLAS naming scheme for the single-jet trigger items include the item's level (L1 or L2) and the energy threshold of the reconstructed jet in GeV.

A L1_J55 item therefore requires a jet with energy equal to or greater than 55 GeV to be found by the level-1 algorithms. However, the jet reconstruction processes of the first and second levels of the trigger are not as elaborate as the offline⁴ jet reconstruction described in section 4.3.2. Jet energies are therefore commonly underestimated by the ATLAS trigger systems. It is therefore crucial to estimate a trigger item’s efficiency with respect to offline reconstructed jets.

Table 6–1: Trigger items considered for the analysis, for each data-taking period. The ‘&’ symbol represents the logical ‘and’ of two conditions. The **NoAlg** suffix in the last L2 item indicates that no L2 algorithm was used in the corresponding trigger chain.

Data-taking periods	
A-F	G-I
L1_J10	L1_J10 & L2_J25
L1_J15	L1_J15 & L2_J30
L1_J30	L1_J30 & L2_J45
L1_J55	L1_J55 & L2_J70
L1_J75	L1_J75 & L2_J90
L1_J95	L1_J95 & L2_L1J95_NoAlg

Throughout the analysis, only events which have greater than 99% probability of satisfying a trigger chain’s set of criteria are used. To ensure this, the trigger efficiencies are computed from data for each trigger chain listed in table 6–1 and for each data-taking period. These efficiencies are computed using a *bootstrapping* technique. This technique consists in calculating the relative trigger efficiency of each single-jet trigger chain using a reference sample obtained from another single-jet trigger chain with lower transverse jet momentum (p_T) threshold. The L1_J10 and L1_J10 & L2_J25 trigger items are

⁴ Offline, as opposed to online or trigger, algorithms are run on data after it has been recorded to permanent storage.

the ones with the lowest energy thresholds considered in the analysis. The relative trigger efficiency of these two trigger items is therefore computed using events satisfying the L1_J5 and L1_J5 & L2_J15 respectively. The absolute trigger efficiencies of the L1_J5 and L1_J5 & L2_J15 trigger items are measured using events satisfying a minimum bias⁵ trigger item. The absolute trigger efficiency of each trigger item is obtained by multiplying its measured relative efficiency with the absolute trigger efficiency of the trigger item used to produce the reference sample.

In order to compute a trigger item's efficiency, we first apply all data quality, vertex and jet requirements discussed in section 6.1.1 to the reference sample. The trigger efficiency is then defined as the total number of events satisfying the item's criteria, without applying a prescale factor, divided by the total number of events in the reference sample.

The efficiencies are computed for the inclusive two- and three-jet samples as a function of Q' . The threshold beyond which a trigger item is deemed fully efficient is defined as the minimum Q' value above which the absolute trigger efficiency is greater than 99% for all bins. This threshold could be different for the inclusive two- and three-jet samples. The actual threshold used to define a trigger item in both samples is therefore the greater of the two. This ensures that for each bin in Q' , the ratio distribution is obtained using only events that satisfy a trigger chain with a trigger efficiency greater than 99%.

The widths of the Q' bins used in this analysis are chosen to maximize the sensitivity of the inclusive ratio to α_S , while minimizing the statistical uncertainty in each bin. The number of events in each bin depends on the

⁵ Minimum bias trigger items randomly select events showing evidence that a collision occurred.

trigger chosen to select the events, which in turn depends on the measured full-efficiency threshold of each trigger. However, the exact value of Q' for which a particular trigger item is measured to be fully efficient varies as a function of the width of the bins used. Therefore, an iterative approach is used to determine the optimal bin widths used in this analysis.

For each Q' bin, the trigger chain with the lowest prescale which is fully efficient is used to select events in that bin. Therefore, only one trigger is used to select events per bin and per data period. The trigger used to select events in each bin is documented in table 6–2.

Events and jets surviving the selection process described in sections 6.1.1 and 6.1.2 are used to measure the inclusive three- to two-jet production ratio. To do so, the number of events featuring three or more jets ($N_{N_{jets} \geq 3}^{events}$) is divided by the number of events with two or more jet ($N_{N_{jets} \geq 2}^{events}$) for each Q' bin. Since the trigger selection and reconstruction process are fully efficient for all events considered, and since only one trigger is used to select all events per bin and per data-taking period, the inclusive three- to two-jet ratio can be calculated in each bin i as

$$R_{3/2}^i = \frac{\sigma_{N_{jets} \geq 3}^i}{\sigma_{N_{jets} \geq 2}^i} = \frac{\left(N_{N_{jets} \geq 3}^{events, i}\right) / \mathcal{L} \varepsilon}{\left(N_{N_{jets} \geq 2}^{events, i}\right) / \mathcal{L} \varepsilon} = \frac{N_{N_{jets} \geq 3}^{events, i}}{N_{N_{jets} \geq 2}^{events, i}}, \quad (6.1)$$

where \mathcal{L} is the integrated luminosity of all the data, and ε is the efficiency at selecting an event with two or more jets. The calculated luminosity associated with each trigger item is therefore not required to perform this measurement of the inclusive three- to two-jet production ratio.

Table 6–2: Trigger item(s) used to select events in each bin of Q' for each ATLAS data-taking period of 2010.

Period	Q' bin center (GeV)											
	110	135	165	205	255	305	360	425	505	625	850	1250
A	L1_J15											
B	L1_J15											
C	L1_J15											
D	L1_J15											
E	L1_J15		L1_J30									
F	L1_J15		L1_J30			L1_J55						
G	L1_J15 & L2_j30		L1_J30 & L2_j45		L1_J55 & L2_j70		L1_J75 & L2_j90		L1_J95 & L2.L1J95.NoAlg			
H	L1_J15 & L2_j30		L1_J30 & L2_j45		L1_J55 & L2_j70		L1_J75 & L2_j90		L1_J95 & L2.L1J95.NoAlg			
I	L1_J15 & L2_j30		L1_J30 & L2_j45		L1_J55 & L2_j70		L1_J75 & L2_j90		L1_J95 & L2.L1J95.NoAlg			

6.2 Unfolding of Detector Effects in Data

In order to compare the measured inclusive three- to two-jet production ratio to NLO predictions described in chapter 5, detector effects must be *unfolded* from the reconstructed data results to obtain a measurement of the ratio at the particle-level.

The unfolding of reconstructed data measurements attempts to correct for all detector effects, in order to infer a particle-level measurement of the inclusive ratio distribution. However, unlike jet calibration corrections described in section 4.3.2, the process is entirely specific to the present analysis and is applied to the inclusive ratio distribution as opposed to individual jets in each event. Indeed, an unfolding correction factor is computed for each bin of the measured inclusive ratio distribution using the ALPGEN+HERWIG/JIMMY Monte-Carlo data samples listed in section 4.2. The unfolding correction factor for each Q' bin $C_{unfolding}(Q')$ is computed as

$$C_{unfolding}(Q') = \frac{R_{3/2}^{particle}(Q')}{R_{3/2}^{reconstructed}(Q')}, \quad (6.2)$$

where $R_{3/2}^{reconstructed}(Q')$ and $R_{3/2}^{particle}(Q')$ are the inclusive three- to two-jet ratio computed from reconstructed and particle- (or truth-) jets respectively. As described in section 4.3.2, particle-jets are built directly from the Monte-Carlo particle or truth information, ignoring any detector effects. To compute the unfolding factor, all analysis-specific selection criteria described in section 6.1.1 are applied to reconstructed jets, while only momentum and pseudorapidity requirements are imposed on particle-jets. Unfolding factors computed with the previously described procedure are shown in figure 6–1(a) to yield correction factors of less than $\sim 5\%$ in all Q' bins. To unfold the data results

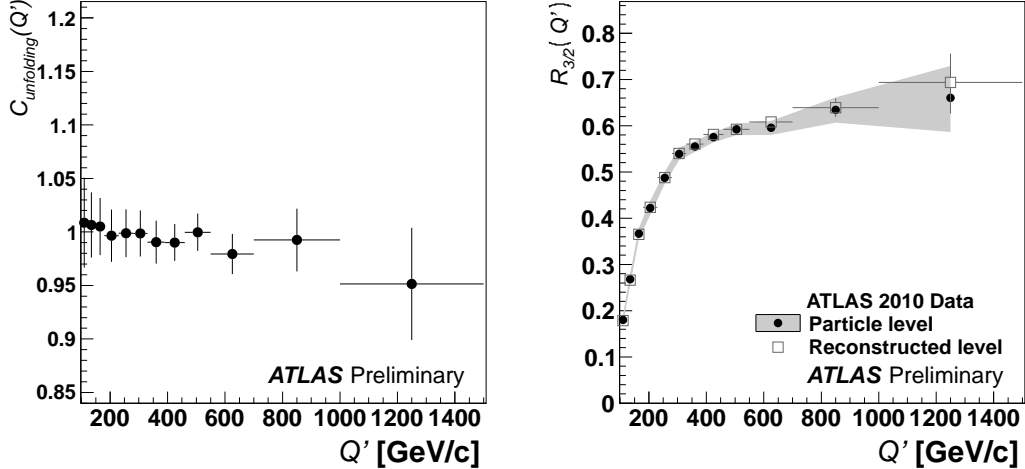


Figure 6–1: (a) Data unfolding correction factor as a function of Q' . Results are obtained from ALPGEN+HERWIG/JIMMY Monte-Carlo samples and only include statistical uncertainties. (b) Comparison of three- to two-jet production ratio measurement before and after unfolding to the particle-level. The reconstructed level distribution only includes statistical uncertainty from the data, while particle-level results also include statistical uncertainty contributions from the unfolding factors. All analysis cuts described in section 6.1 are applied to reconstructed jets, only p_T and η cuts are applied to particle-jets.

to the particle-level, the reconstructed ratio is multiplied bin-by-bin with the corresponding unfolding factors⁶.

The calculations of the unfolding factors do not account for the presence of pile-up effects in the measured quantities. Uncertainties on the unfolding factors due to pile-up effects and Monte-Carlo modelling (i.e. the choice of generator, parton showering and hadronization algorithms), are detailed in section 6.2.1. The final unfolded ratio measurement is shown in figure 6–1(b), and individual Q' bin values are tabulated in table 6–3, providing detailed uncertainty contributions from each source described in sections 6.2.1 and 6.3.

⁶ Note that this approach is mathematically equivalent to unfolding the inclusive two- and three-jet cross-section distributions independently and dividing both to calculate the three- to two-jet cross-section ratio.

Table 6–3: Detailed uncertainty contributions to the inclusive ratio computed from ATLAS 2010 data. All the results are unfolded to the particle-level. Results are tabulated as a function of Q' and are computed with all analysis cuts described in section 6.1 applied.

Q' range (GeV)	Unfolded $R_{3/2}$	Sources of uncertainty			
		Data statistics	ALPGEN statistics	Trigger	Modelling
100-120	0.180	+0.006 –0.006	+0.007 –0.007	± 0.003	± 0.005
120-150	0.268	+0.009 –0.009	+0.008 –0.008	± 0.004	± 0.003
150-180	0.367	+0.008 –0.008	+0.010 –0.010	± 0.005	± 0.001
180-230	0.422	+0.011 –0.011	+0.010 –0.010	± 0.006	± 0.015
230-280	0.487	+0.007 –0.007	+0.011 –0.011	± 0.007	± 0.005
280-330	0.539	+0.007 –0.007	+0.012 –0.012	± 0.008	± 0.005
330-390	0.555	+0.003 –0.003	+0.011 –0.011	± 0.008	± 0.019
390-460	0.575	+0.004 –0.004	+0.010 –0.010	± 0.008	± 0.011
460-550	0.592	+0.006 –0.006	+0.010 –0.010	± 0.008	± 0.005
550-700	0.595	+0.010 –0.010	+0.011 –0.011	± 0.008	± 0.014
700-1000	0.634	+0.020 –0.020	+0.019 –0.019	± 0.009	± 0.007
1000-1500	0.660	+0.064 –0.059	+0.036 –0.036	± 0.009	± 0.046

Q' range (GeV)	Sources of uncertainty				
	JES	JER	η resolution	Pile-up	Jet quality
100-120	± 0.005	± 0.005	± 0.001	± 0.007	± 0.001
120-150	± 0.004	± 0.009	± 0.002	± 0.009	± 0.000
150-180	± 0.005	± 0.006	± 0.002	± 0.016	± 0.000
180-230	± 0.003	± 0.007	± 0.002	± 0.003	± 0.000
230-280	± 0.014	± 0.004	± 0.001	± 0.006	± 0.000
280-330	± 0.003	± 0.011	± 0.001	± 0.004	± 0.000
330-390	± 0.002	± 0.003	± 0.001	± 0.014	± 0.000
390-460	± 0.002	± 0.007	± 0.001	± 0.011	± 0.000
460-550	± 0.007	± 0.009	± 0.001	± 0.010	± 0.000
550-700	± 0.007	± 0.009	± 0.001	± 0.011	± 0.000
700-1000	± 0.011	± 0.012	± 0.004	± 0.044	± 0.001
1000-1500	± 0.021	± 0.051	± 0.001	± 0.078	± 0.026

6.2.1 Uncertainties on Data Unfolding

The previously described unfolding technique relies on the assumption that simulated detector effects closely resemble those found in data. However,

varying pile-up effects present in data are not modelled in the unfolding procedure. This effect is, however, greatly reduced due to the primary vertex and jet selection cuts detailed in section 6.1.1. Therefore, rather than unfolding pile-up effects directly, we estimate an uncertainty on the reconstructed Monte-Carlo sample due to the presence of pile-up in data.

To estimate the uncertainty due to pile-up effects, the inclusive three- to two-jet ratio is computed from both in time and bunch train pile-up Monte-Carlo samples described in section 4.2. We compare results from each pile-up sample with the pile-up-free ALPGEN+HERWIG/JIMMY sample and take the largest fluctuation in each bin as a symmetric uncertainty on the reconstructed ratio. The individual ratio computed for each Monte-Carlo configuration and the resulting uncertainty on the unfolded measurement of the inclusive ratio are shown in figures 6–2(a) and (b) respectively. These figures indicate that the overall uncertainty due to pile-up is at most 2% for $Q' < 700$ GeV and up to $\sim 12\%$ over the last two Q' bins ($700 < Q' < 1500$), in large part due to statistical limitations of Monte-Carlo simulations in that energy range.

The unfolding correction factor described in equation 6.2 is computed entirely from Monte-Carlo simulations. Different event generators, showering and hadronization algorithms can result in different predictions of the inclusive three- to two-jet ratio. An uncertainty on the unfolded data due to the choice of models and parameters used in simulations is therefore estimated. To do so, the data ratio is unfolded using several Monte-Carlo simulated samples generated with different tools and parameters. The ALPGEN+PYTHIA Monte-Carlo simulated sample is used to estimate the difference in unfolding due to the choice of parton shower algorithms, while PYTHIA AMBT1 and PYTHIA Perugia 2010 samples are used to estimate the difference between the full

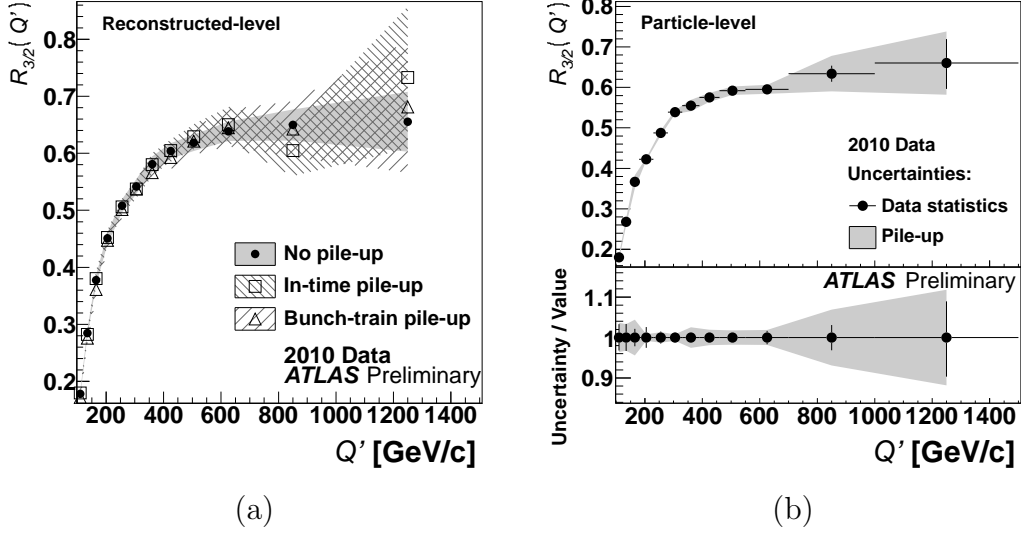


Figure 6-2: (a) Inclusive ratio as a function of Q' computed from ALPGEN+HERWIG/JIMMY Monte-Carlo simulated samples with different pile-up configurations. (b) Unfolded data to particle-level with unfolded pile-up and statistical uncertainties. All analysis cuts described in section 6.1.1 are applied to reconstructed jets.

and partial matrix element calculations with different underlying event contributions. Figure 6-3(a) shows the unfolding correction factors obtained in each case. Results show that unfolding correction factors from all simulations agree within statistical uncertainty. Moreover, unfolding factor corrections are smaller than 5% for the entire Q' range and for all Monte-Carlo simulations. For each Q' bin the maximum difference between the ratio unfolded using the ALPGEN+HERWIG/JIMMY sample and the ratio unfolded with any other simulation is computed and taken as a symmetric uncertainty on the unfolded data ratio. The resulting uncertainty on the unfolded data ratio is generally less than $\sim 4\%$ with the exception of the highest energy bin which features an uncertainty of $\sim 7\%$, as shown in figure 6-3(b).

Since the unfolding correction factor is nearly constant across all bins and within statistical and modelling uncertainty of unity, the unfolding procedure does not bias the data toward a specific $\alpha_S(M_Z)$ value.

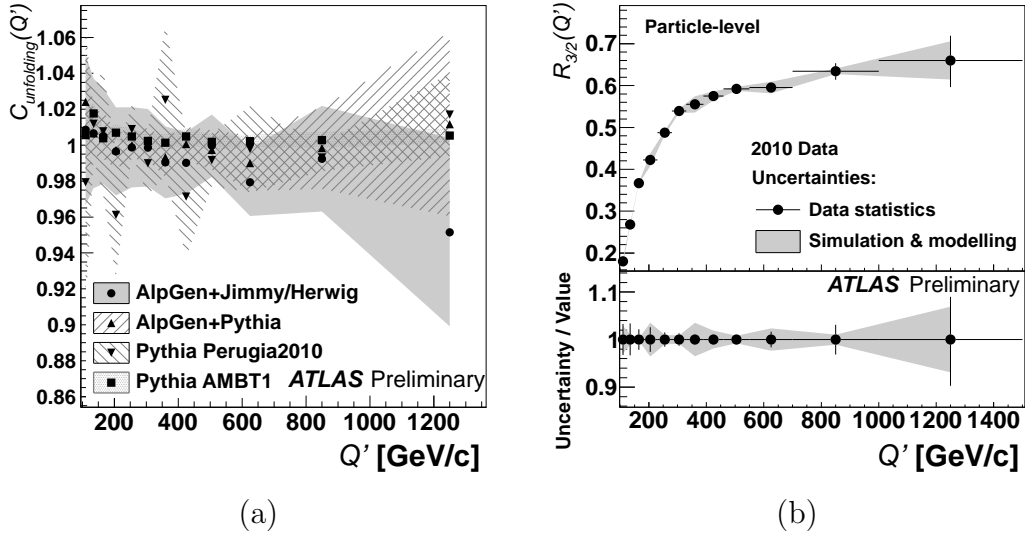


Figure 6-3: (a) Data unfolding factor $C_{unfolding}(Q')$ computed from ALPGEN+HERWIG/JIMMY, ALPGEN+PYTHIA and PYTHIA with two different underlying event tunes. (b) Three- to two-jet cross-section ratio unfolded to the particle-level, showing the size of the uncertainty associated to the choice of Monte-Carlo models to perform the unfolding. Results are shown as a function of Q' and all analysis cuts described in section 6.1 are applied.

6.3 Uncertainties on $R_{3/2}$ Measurement

6.3.1 Statistical Uncertainties

The statistical uncertainty on the measurement of the inclusive ratio is obtained bin-by-bin by combining the statistical uncertainties on the two-jet and three-jet distributions. When the same data or simulation sample is used for both the numerator and denominator of the ratio, the statistical uncertainties are combined using Bayesian statistical methods [75, 76]. Otherwise the samples are assumed to be independent and both uncertainties are propagated to the ratio using standard error propagation techniques based on partial derivatives. Statistical uncertainties arise from both the data, and Monte-Carlo simulations used during the unfolding process. The resulting uncertainties on the unfolded three- to two-jet cross-section ratio are tabulated in table 6-3 for each source of statistical uncertainty.

6.3.2 Trigger Selection Efficiency

As described in section 6.1.2, for a trigger item to be used in a specific Q' bin, it must be more than 99% efficient at selecting events for that specific bin. The statistical uncertainty on each trigger item's full-efficiency threshold was determined to be significantly less than 1%. It follows that since only one trigger item is used to select events per bin per data collection period, the uncertainty due to trigger selection is conservatively estimated to be 1% for each bin of the two- and three-jet distributions computed from data. This uncertainty is propagated through the unfolding process to the unfolded inclusive ratio measurement, as tabulated in table 6-3.

6.3.3 Jet Energy Scale Uncertainty

Jet energy scale corrections described in section 4.3.2 are applied to reconstructed jets in both real and simulated data. Moreover, the same JES correction scheme is used in both cases. The overall uncertainty due to JES effects on the unfolded inclusive three- to two-jet production ratio must therefore account for the correlation between the data and Monte-Carlo samples used. A toy Monte-Carlo approach is used where the transverse momentum of each jet is varied by an amount proportional to the individual jet's JES uncertainty [68]. The same proportionality factor is used for all the jets in both the data and ALPGEN+HERWIG/JIMMY Monte-Carlo sample used during the unfolding process described in section 6.2. The unfolded inclusive three- to two-jet production ratio is computed this way four hundred times, each time generating a random JES proportionality factor according to a standard normal distribution⁷. The resulting inclusive ratio values from all iterations are

⁷ A Gaussian distribution of width equal to one and mean of zero

then fitted to a Gaussian distribution for each Q' bin. The overall JES uncertainty on the unfolded ratio is computed as the sum of the standard deviation of the fit and the difference between the mean of the fit and the unfolded ratio's central value for each Q' bin. The resulting uncertainties on the unfolded ratio are less than 3.5% throughout the energy range studied as shown in figure 6–4. Detailed JES uncertainties on the unfolded ratio are tabulated in table 6–3.

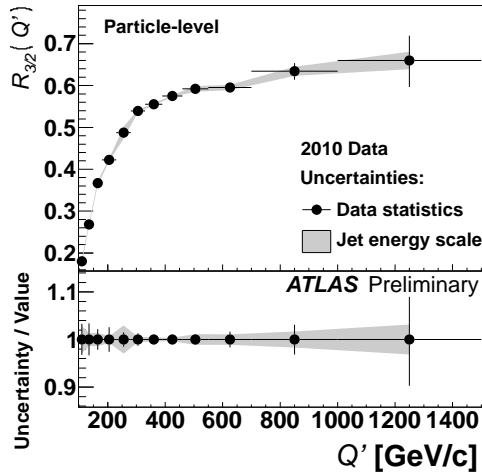


Figure 6–4: Jet energy scale uncertainty propagated to the unfolded inclusive three- to two-jet cross-section ratio. Results are shown as a function of Q' and are obtained from the ATLAS 2010 data set with all analysis cuts described in section 6.1 applied.

6.3.4 Jet Energy and Angular Resolutions

Resolution effects, like JES effects, are present in reconstructed quantities computed from both data and Monte-Carlo samples. However, the resolution effects are not correlated between the data and simulations. Similarly to the JES uncertainty calculations, the jet energy resolution (JER) or angular resolution uncertainties are computed using a toy Monte-Carlo approach. This technique varies the transverse momentum or pseudo-rapidity of each jet by an amount proportional to the corresponding resolution. The variation amount is randomly generated for each jet based on a Gaussian distribution whose standard deviation is equal to the individual jet's resolution. The same technique

is applied to both data and Monte-Carlo samples with different random number generator seeds. The resulting inclusive ratio from the modified data is unfolded using the correspondingly modified Monte-Carlo samples, following the same approach as described in section 6.2. This procedure is repeated two hundred times, each time with unique random numbers. The unfolded ratio values obtained are fitted to a Gaussian distribution for each Q' bin. The overall resolution uncertainties on the unfolded ratio are computed for each bin as the sum of the standard deviation of the fit and the difference between the mean of the fit and the unfolded ratio's central value.

The jet energy resolution [63, 77] is a function of transverse momentum and pseudo-rapidity of the jets. The jet energy resolution varies between 4% and 14%. As the analysis is completely independent of azimuthal coordinates, only pseudo-rapidity resolution effects are considered for angular resolution uncertainty calculations. The conservative value of 0.1 is used as the η resolution, which is the maximum η granularity of the electro-magnetic calorimeter and of the first two layers of the hadronic calorimeter [78, 79]. The resulting uncertainties on the unfolded ratio due to JER effect are generally between $\sim 0.5\%$ and $\sim 4\%$ with the exception of the last bin at $\sim 8\%$, while angular resolution effects result in negligible uncertainties, as shown in figure 6–5. Both detailed JER and angular resolution uncertainties on the unfolded ratio are tabulated in table 6–3.

6.3.5 Jet Quality Requirements

Since jet quality variables are not properly modelled in simulations, the uncertainty due to the jet quality requirements described in section 6.1.1 is directly estimated from data. To do so, the analysis is re-done allowing *bad* and/or *ugly* jets to be used. Figure 6–6(a) shows the relative change in the results obtained with each configuration of jet quality requirements. These

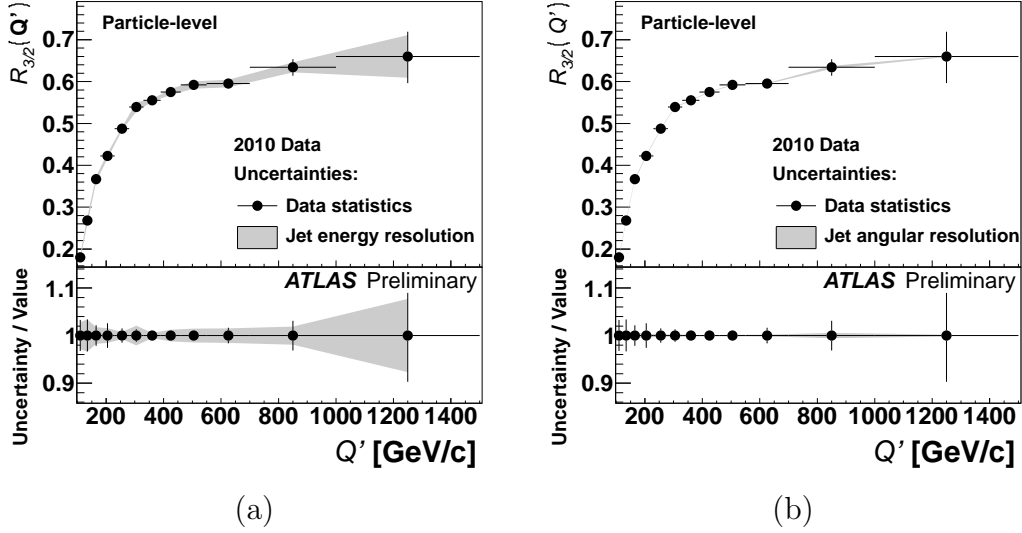


Figure 6–5: Jet energy resolution (a) and angular resolution (b) uncertainties propagated to the unfolded inclusive three- to two-jet cross-section ratio. Results are shown as a function of Q' and are obtained from the ATLAS 2010 data set with all analysis cuts described in section 6.1 applied.

results show that the overall effect of including *bad* and/or *ugly* jets is at most $\sim 4\%$ in the highest energy bin and negligible in all others. The maximum shift in each bin observed in figure 6–6(a) is taken as a symmetric relative uncertainty on the inclusive ratio computed from data due to jet quality requirements. This uncertainty is propagated to the particle-level and the resulting unfolded jet quality uncertainty is shown in figure 6–6(b). These uncertainties on the unfolded ratio are listed in table 6–3.

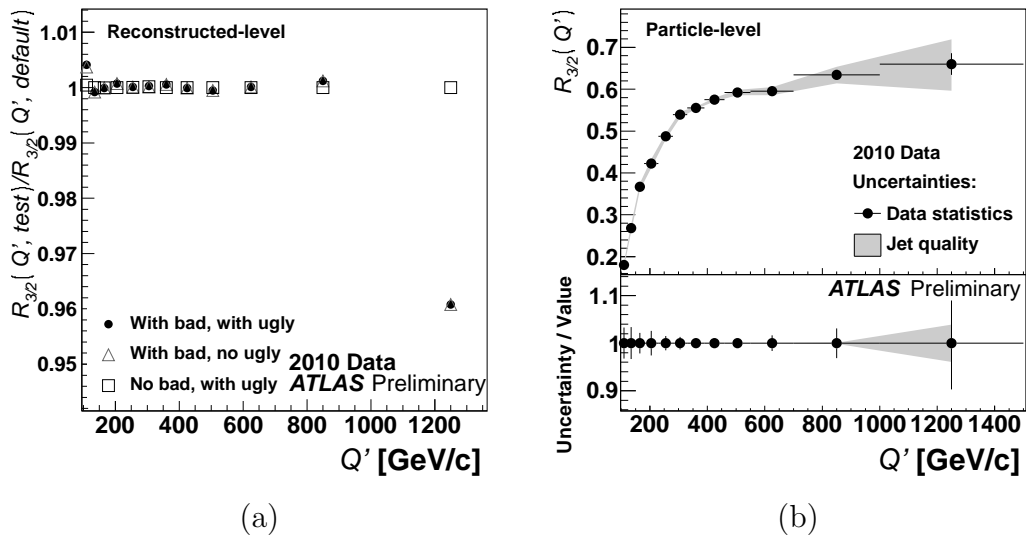


Figure 6–6: (a) Ratio of $R_{3/2}(Q')$ computed with different jet quality criteria over that computed with the default set of criteria, i.e. no *bad* or *ugly* jets allowed. (b) Inclusive three- to two-jet cross-section ratio with statistical and jet quality uncertainties unfolded to particle level. Results are shown as a function of Q' and are obtained from the ATLAS 2010 data set with all analysis cuts described in sections 6.1.1 applied.

CHAPTER 7

Strong Coupling Measurement

This chapter describes the measurement of the strong coupling constant by comparing the theoretical predictions of the inclusive three- to two-jet production cross-section ratio described in chapter 5, to its measurement detailed in chapter 6. Comparisons of the data measurement and theoretical predictions of the ratio are presented in section 7.1, while the fitting technique is described in section 7.2. Finally, the strong coupling measurement results are presented in section 7.3.

7.1 Comparison of $R_{3/2}$ Measurement to Theoretical Predictions

The particle-level inclusive three- to two-jet production cross-section ratio distributions, obtained from the ATLAS 2010 data and NLO calculations, are compared in figure 7–1. The uncertainties presented include all sources listed in table 7–1, whose values are tabulated in tables 5–1 and 6–3. Figures 7–1(a) and (b) respectively display the ratio’s theoretical predictions for $\alpha_S(M_Z) = 0.110$ and $\alpha_S(M_Z) = 0.130$, however similar results are also computed for all the $\alpha_S(M_Z)$ values within that range, in increments of 0.001¹. The ratio measurements are shown to be mostly within the $0.110 \leq \alpha_S(M_Z) \leq 0.130$ range of the theoretical predictions for all Q' bins. Results not within that range are close enough for a fitting technique to extrapolate a strong coupling measurement.

¹ PDF sets matching the $\alpha_S(M_Z)$ values 0.110, 0.111, 0.112, ..., 0.130 are provided by the MSTW group.

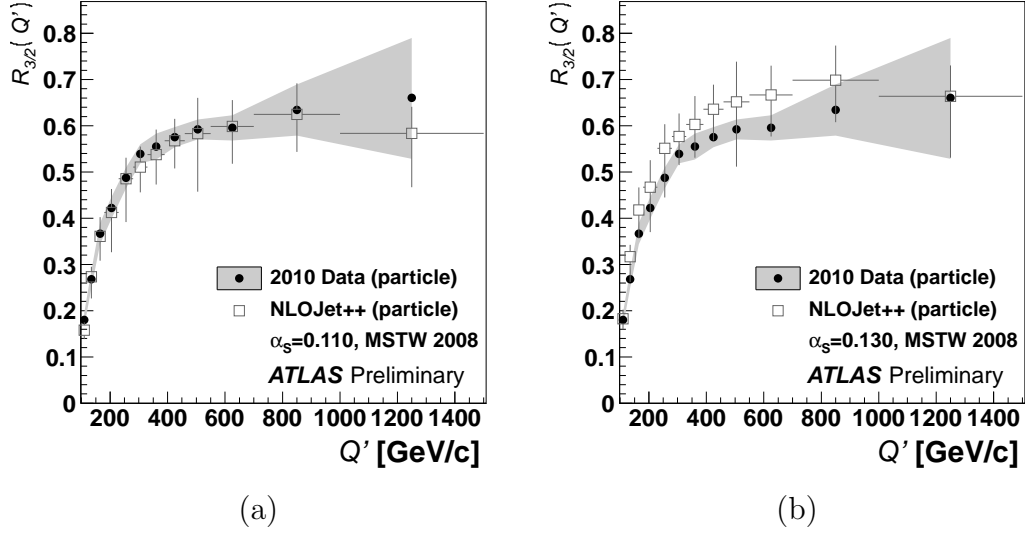


Figure 7–1: Comparison of the inclusive three- to two-jet production cross-section ratio measurement with NLO predictions for (a) $\alpha_S = 0.110$ and (b) $\alpha_S = 0.130$. The error band represents the combination of all statistical and systematic uncertainties on the data measurement, while the error bars represent the combined statistical, theoretical and systematic uncertainties on the theoretical predictions. All results are calculated at the particle-level, and all uncertainties described in chapters 5 and 6 are included. Results are shown as a function of Q' and are obtained from the ATLAS 2010 data set with all analysis cuts described in sections 6.1 applied.

7.2 Measurement Technique

The strong coupling constant is measured by finding the $\alpha_S(M_Z)$ value which would yield the best theoretical description of the measured inclusive three- to two-jet production cross-section ratio. All systematic uncertainties on both predicted and measured ratio distributions, and which are not statistical in nature, exhibit correlation between Q' bins, as indicated in table 7–1. The $\alpha_S(M_Z)$ measurement technique must therefore account for these correlations.

The approach used to measure the strong coupling constant is a Hessian [80] least squares fit. This method, previously used by the ZEUS and H1 collaborations for PDF analyses [80], uses a chi-squared (χ^2) function that takes into account correlated sources of uncertainties. This function is defined

Table 7–1: List of all sources of uncertainties considered in the analysis, and whether they are treated as correlated between Q' bins.

	Type of Uncertainty		Correlated	
Data Measurement	Data Statistics		No	
	Trigger Selection		Yes	
	Jet Energy Scale		Yes	
	Jet Energy Resolution		Yes	
	Angular Resolution		Yes	
	Jet Quality		Yes	
	Unfolding Correction	Jet Energy Scale		Yes
		Jet Energy Resolution		Yes
		Angular resolution		Yes
		Pile-up		Yes
Monte-Carlo Modelling		Yes		
	ALPGEN Statistics		No	
Theoretical Predictions	NLOJET++ Statistics		No	
	Scale		Yes	
	PDF		Yes	
	Non-pQCD correction factor	ALPGEN Statistics		No
Monte-Carlo Modelling		Yes		

as

$$\chi^2 = \sum_i \frac{\left[R_{3/2}^{(theory)}(\alpha_S(M_Z), i) - R_{3/2}^{(measured)}(i) + \sum_\lambda s_\lambda \Delta_{i\lambda}^{(correlated)} \right]^2}{\sum_{\lambda'} \left[\Delta_{i,\lambda'}^{(uncorrelated)} \right]^2} + \sum_\lambda s_\lambda^2, \quad (7.1)$$

where $R_{3/2}^{(measured)}(i)$ is the measured inclusive three- to two-jet production cross-section ratio for the i -th Q' bin, and $R_{3/2}^{(theory)}(\alpha_S(M_Z), i)$ is the theoretical prediction of the ratio in the i -th bin as a function of $\alpha_S(M_Z)$. The symbols $\Delta_{i,\lambda'}^{(uncorrelated)}$ and $\Delta_{i\lambda}^{(correlated)}$ are the i -th bin's uncorrelated and correlated uncertainties from sources λ' and λ , respectively. The s_λ parameters are independent variables (nuisance parameters) associated with each source of correlated uncertainty, and are defined to have a unit variance and a mean of zero. In order to obtain continuous theoretical distributions $R_{3/2}^{(theory)}(\alpha_S(M_Z), i)$ as a function of $\alpha_S(M_Z)$ in each Q' bin, a spline interpolation is used. Figure 7–2

shows examples of such interpolations and the resulting continuous functions for different Q' bins.

The least squares fit is performed by minimizing the chi-squared value with respect to $\alpha_s(M_Z)$ and the free parameters s_λ . Allowing the s_λ parameters to fluctuate effectively allows both the data and theoretical predictions to vary, collectively, within the bounds of their correlated systematic uncertainties. The $\alpha_s(M_Z)$ and s_λ configuration corresponding to the minimal chi-squared value yields the most consistent fit in all Q' bins. An uncertainty of one standard deviation on the resulting best-fit's $\alpha_s(M_Z)$ is defined as an increase of one unit in the chi-squared function, with respect to its minimum value.

Since the theoretical scale uncertainty can be highly asymmetric in most Q' bins, it cannot be included in the previously described procedure. To estimate the scale uncertainty on the best-fit's $\alpha_s(M_Z)$ value, the least squares fit is recomputed while shifting the theoretical predictions of each bin by its positive and negative theoretical scale uncertainties. The difference between the resulting $\alpha_s(M_Z)$ value and the best-fit's $\alpha_s(M_Z)$ value is used as scale uncertainty on the final result.

7.3 Results

The least squares method was applied to each individual bin of the inclusive three- to two-jet production cross-section ratio, as well as to all bins simultaneously. The resulting measurements of the strong coupling are tabulated in table 7-2. The simultaneous fit of all Q' bins yields an $\alpha_s(M_Z)$ measurement of $0.111_{-0.008}^{+0.009}$, with a $\chi^2/\text{d.o.f.}$ of 5.3/10. Taking into account the contribution from the scale uncertainty, the final result of this analysis is $0.111_{-0.012}^{+0.016}$. The nuisance parameters s_λ obtained from the fitting procedure are tabulated in appendix A, and are all within statistical uncertainty of zero,

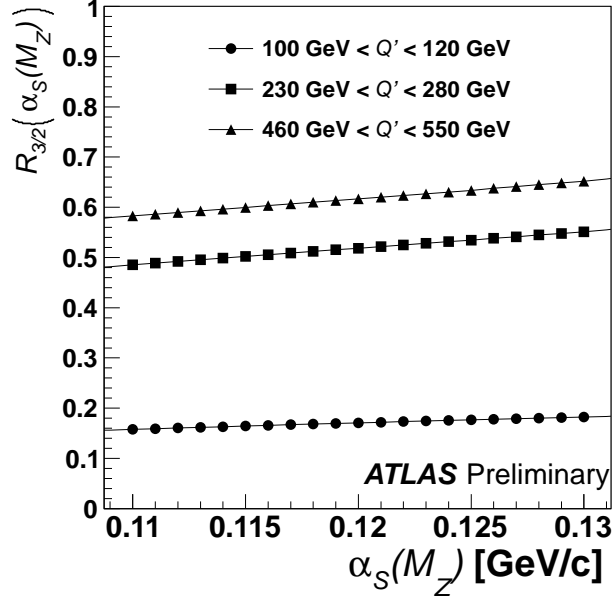


Figure 7–2: Inclusive ratio of three- to two-jet differential cross-sections as a function of $\alpha_s(M_Z)$ calculated at NLO and corrected for non-perturbative effects, for three bins of Q' . The points represent the results of the calculations and the solid line shows the spline interpolation used in the least squares fit. Note that the statistical uncertainty is smaller than the size of the markers.

indicating a good agreement between theoretical predictions and measurements of the ratio. Estimates of uncertainty contributions from each source of uncertainty are provided in table 7–3. These estimates are computed as the square root of the quadratic difference between the total uncertainty calculated while letting all nuisance parameters vary and the uncertainty obtained while fixing a specific nuisance parameter to its best fitted value. Results indicate that the largest sources of uncertainty are the NLO scale and non-perturbative corrections of theoretical predictions, while all measurement uncertainties are comparatively much smaller. Moreover, all non-negligible measurement uncertainties are similar in magnitude due to the use of a ratio of jet production cross-sections.

Figure 7–3 compares the ATLAS 2010 data measurements at particle-level of the inclusive three- to two-jet production cross-section ratio to the

Table 7–2: Best fitted $\alpha_s(M_Z)$ values and uncertainties obtained from the least squares fit of each Q' bin, as well as for all bins simultaneously.

Q' range (GeV)	$\alpha_s(M_Z)$	Total uncertainty	Fit uncertainty	Scale uncertainty
100-120	0.128	+0.023 -0.019	+0.020 -0.017	+0.011 -0.007
120-150	0.108	+0.029 -0.011	+0.018 -0.010	+0.023 -0.004
150-180	0.112	+0.027 -0.013	+0.020 -0.010	+0.018 -0.009
180-230	0.113	+0.035 -0.018	+0.022 -0.013	+0.027 -0.012
230-280	0.111	+0.033 -0.013	+0.021 -0.011	+0.025 -0.007
280-330	0.119	+0.021 -0.015	+0.016 -0.012	+0.014 -0.008
330-390	0.115	+0.025 -0.021	+0.020 -0.019	+0.016 -0.009
390-460	0.112	+0.024 -0.030	+0.018 -0.028	+0.016 -0.012
460-550	0.113	+0.032 -0.018	+0.020 -0.011	+0.024 -0.014
550-700	0.109	+0.032 -0.014	+0.023 -0.011	+0.022 -0.008
700-1000	0.113	+0.028 -0.019	+0.022 -0.016	+0.019 -0.011
1000-1500	0.129	+0.011 -0.040	+0.008 -0.038	+0.007 -0.011
100-1500	0.111	+0.016 -0.012	+0.009 -0.008	+0.013 -0.009

NLOJET++ predictions computed using the MSTW 2008 NLO PDF set at the best fitted value of $\alpha_s(M_Z) = 0.111$. Both distributions agree within uncertainty for the entire kinematic range. The final result of this analysis and the individual $\alpha_S(M_Z)$ measurements in each bin are in statistical agreement with the accepted world average of $\alpha_S(M_Z) = 0.1184 \pm 0.0007$ [12]. Moreover, all results are found to be in statistical agreement with similar CDF [18] and DØ [13] measurements of $\alpha_S(M_Z) = 0.1178_{-0.0095}^{+0.0081}(sys.) \pm 0.0001(stat.)$ and $\alpha_S(M_Z) = 0.1161_{-0.0048}^{+0.0041}$ respectively. Figure 7–4 compares the strong coupling measurement from this analysis with past measurements used in the calculation of the world average α_S value, and results from CDF and DØ.

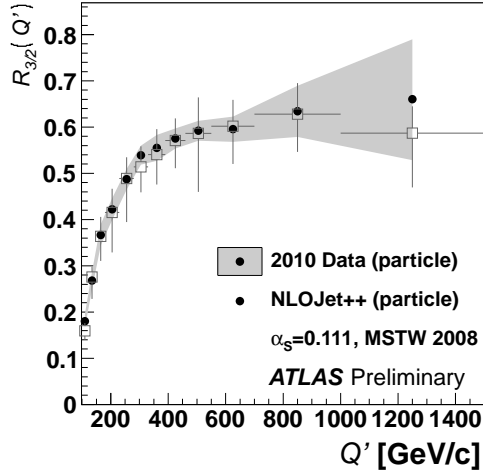


Figure 7–3: Inclusive jet ratio computed as a function of Q' from ATLAS 2010 data and NLOJET++ simulations with the MSTW 2008 NLO PDF set at the $\alpha_S(M_Z)$ values of 0.111, corresponding to the best fit measurement of the strong coupling constant. Both distributions are shown at the particle-level and include all uncertainties previously discussed. All analysis cuts described in section 6.1 are applied.

The $\alpha_S(M_Z)$ results showed in Table 7–2 can be evolved to $\alpha_S(Q')$ for each Q' bin using the two-loop approximate solution to the RGE² [11]. The resulting distribution is shown in figure 7–5. Results show good agreement between the $D\bar{O}$ inclusive jet fit [13], ZEUS [14] and H1 [15] α_S measurements, and the RGE predictions evaluated at this analysis' measured $\alpha_S(M_Z)$ value of $0.111^{+0.016}_{-0.012}$. Results from this analysis are therefore consistent with the RGE predictions up to a renormalization scale of 1.5 TeV.

² This two-loop approximation is described in section 2.1.3. It is the same approximation used internally by LHAPDF and NLOJET++.

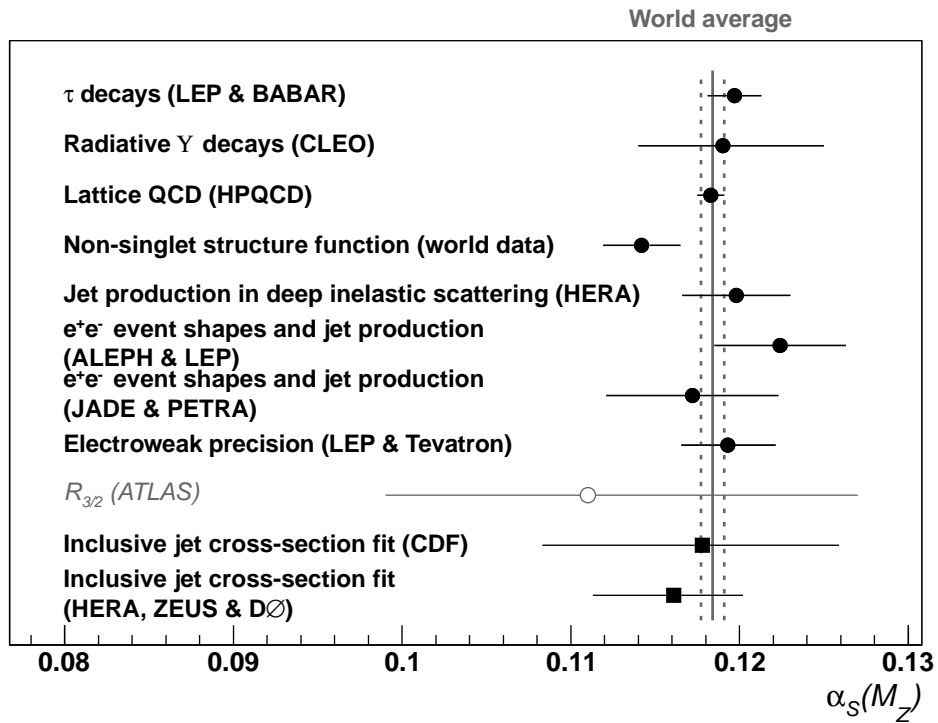


Figure 7–4: Comparison of past measurements of $\alpha_S(M_Z)$ used in the computation of the world average (solid dots) [12], the result from this analysis $\alpha_S(M_Z) = 0.111^{+0.016}_{-0.012}$ (empty dot), the latest CDF [18] and DØ results [13] (solid squares).

Table 7–3: Uncertainty contribution estimates on best fitted $\alpha_s(M_Z)$ values for each Q' bin, as well as for all bins simultaneously.

Q' range (GeV)	$\alpha_s(M_Z)$	Total	Total uncorrelated	Total correlated	Trigger	JES	JER
100-120	0.128	+0.023 -0.019	± 0.010	+0.017 -0.014	+0.002 -0.001	+0.005 -0.005	+0.001 -0.004
120-150	0.108	+0.029 -0.011	± 0.006	+0.017 -0.008	+0.002 -0.001	+0.003 -0.002	+0.004 -0.002
150-180	0.112	+0.027 -0.013	± 0.005	+0.019 -0.008	+0.002 -0.001	+0.002 -0.000	+0.003 -0.002
180-230	0.113	+0.035 -0.018	± 0.006	+0.022 -0.012	+0.003 -0.002	+0.004 -0.005	+0.002 -0.002
230-280	0.111	+0.033 -0.013	± 0.005	+0.020 -0.010	+0.002 -0.001	+0.000 -0.002	+0.006 -0.004
280-330	0.119	+0.021 -0.015	± 0.005	+0.015 -0.011	+0.002 -0.002	+0.003 -0.002	+0.001 -0.002
330-390	0.115	+0.025 -0.021	± 0.005	+0.019 -0.018	+0.002 -0.005	+0.006 -0.033	+0.002 -0.000
390-460	0.112	+0.024 -0.030	± 0.004	+0.018 -0.028	+0.003 -0.000	+0.005 -0.009	+0.000 -0.003
460-550	0.113	+0.032 -0.018	± 0.006	+0.019 -0.010	+0.002 -0.002	+0.003 -0.002	+0.001 -0.002
550-700	0.109	+0.032 -0.014	± 0.005	+0.022 -0.009	+0.003 -0.002	+0.002 -0.005	+0.002 -0.002
700-1000	0.113	+0.028 -0.019	± 0.010	+0.019 -0.012	+0.001 -0.000	+0.005 -0.003	+0.003 -0.003
1000-1500	0.129	+0.011 -0.040	± 0.022	+0.021 -0.031	+0.001 -0.003	+0.007 -0.011	+0.004 -0.011
100-1500	0.111	+0.016 -0.012	± 0.002	+0.009 -0.008	+0.002 -0.001	+0.000 -0.001	+0.002 -0.002
Q' range (GeV)	η Res	Pile-up	Monte-Carlo modelling	Jet quality	PDF	Non-pert. correction	Scale
100-120	+0.007 -0.006	+0.000 -0.000	+0.004 -0.005	+0.002 -0.000	+0.002 -0.000	+0.012 -0.011	+0.011 -0.007
120-150	+0.007 -0.004	+0.000 -0.000	+0.006 -0.003	+0.000 -0.000	+0.001 -0.000	+0.013 -0.006	+0.023 -0.004
150-180	+0.004 -0.004	+0.000 -0.000	+0.008 -0.004	+0.000 -0.000	+0.000 -0.000	+0.015 -0.006	+0.018 -0.009
180-230	+0.003 -0.004	+0.002 -0.002	+0.002 -0.002	+0.000 -0.000	+0.002 -0.002	+0.018 -0.010	+0.027 -0.012
230-280	+0.000 -0.002	+0.000 -0.000	+0.002 -0.001	+0.000 -0.000	+0.000 -0.000	+0.017 -0.008	+0.025 -0.007
280-330	+0.006 -0.004	+0.000 -0.000	+0.001 -0.002	+0.000 -0.000	+0.001 -0.002	+0.011 -0.009	+0.014 -0.008
330-390	+0.004 -0.036	+0.001 -0.000	+0.003 -0.008	+0.001 -0.000	+0.001 -0.004	+0.014 -0.017	+0.016 -0.009
390-460	+0.003 -0.009	+0.000 -0.000	+0.004 -0.001	+0.000 -0.000	+0.002 -0.001	+0.015 -0.027	+0.016 -0.012
460-550	+0.005 -0.004	+0.000 -0.000	+0.003 -0.002	+0.001 -0.000	+0.002 -0.001	+0.016 -0.009	+0.024 -0.014
550-700	+0.003 -0.004	+0.000 -0.000	+0.004 -0.002	+0.000 -0.000	+0.002 -0.001	+0.019 -0.008	+0.022 -0.008
700-1000	+0.009 -0.006	+0.002 -0.000	+0.007 -0.007	+0.002 -0.000	+0.000 -0.000	+0.009 -0.007	+0.019 -0.011
1000-1500	+0.012 -0.018	+0.002 -0.004	+0.004 -0.018	+0.004 -0.008	+0.000 -0.000	+0.002 -0.000	+0.007 -0.011
100-1500	+0.009 -0.003	+0.000 -0.000	+0.000 -0.000	+0.000 -0.000	+0.000 -0.000	+0.008 -0.007	+0.013 -0.009

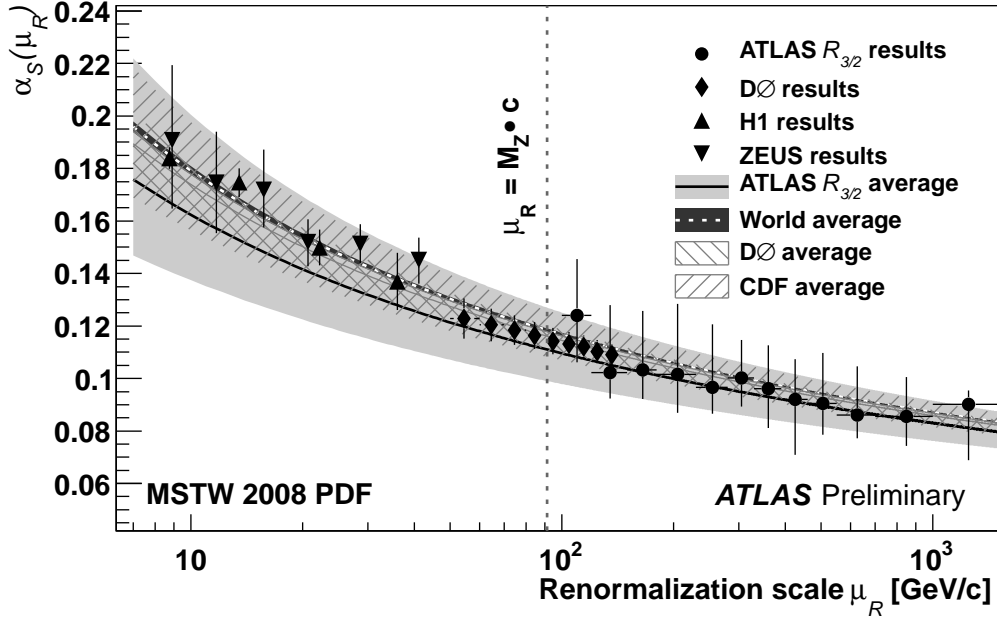


Figure 7–5: Strong coupling α_S measurements from jet production at DØ, H1 and ZEUS, as well as ATLAS $R_{3/2}$. Results are shown as a function of renormalization scale μ_R . The renormalization scale is parametrized as the leading jet p_T for DØ, ZEUS and H1, and by Q' (see eq. (5.6)) for ATLAS. Results show good agreement between both sets of measurements and predictions obtained from the RGE two-loop solution [11] evaluated at this analysis' measured average $\alpha_S(M_Z)$ value of $0.111^{+0.016}_{-0.012}$ and the predicted running at the world average value of 0.1184 ± 0.0007 . The plot also compares the agreement between predictions of the RGE evaluated at this analysis' measured $\alpha_S(M_Z)$ value, CDF and DØ measured values of $0.1178^{+0.0081}_{-0.0095}$ and $\alpha_S(M_Z) = 0.1161^{+0.0041}_{-0.0048}$ respectively.

CHAPTER 8

Summary, Conclusions and Outlook

A first measurement of the QCD strong coupling $\alpha_S(M_Z)$ was performed at a centre-of-mass energy of 7 TeV using data collected by the ATLAS detector in 2010. This data set represents an integrated luminosity of 37.6 pb^{-1} . This also constitutes the first measurement of the strong coupling constant using a ratio of jet multiplicity cross-sections at a hadron collider. Good agreement was found between NLO predictions and data measurements of the inclusive three- to two-jet differential cross-section ratio as a function of the Q' observable.

The strong coupling $\alpha_S(M_Z)$ was measured at NLO pQCD precision for several Q' values and the results were found to agree with the world average, as well as with past measurements performed at hadron colliders and based on jet final states. The overall uncertainty on the measurement is dominated by NLO theoretical scale uncertainties, as well as Monte-Carlo modelling uncertainties arising in data unfolding and non-perturbative QCD corrections. As a result, the overall uncertainty is significantly larger than measurements made by the CDF and DØ collaborations. Due to the reduced dependence of the ratio on PDFs, this analysis is able to extend for the first time the renormalization scale range studied from 209 GeV to 1.5 TeV. This analysis therefore provides a test of pQCD and of the energy dependence of the strong coupling as predicted by the RGE. Results are shown to be consistent with the theory of pQCD, including its description of the running of the coupling, at this unprecedented energy regime.

Further tuning of the Monte-Carlo simulations to the LHC conditions and the constant improvements to NLO prediction tools will reduce uncertainties associated with data unfolding and non-perturbative effects corrections to NLO predictions. Larger data samples are also becoming available and will allow for much smaller binning of the hard scale, improving the resolution on the shape of the three- to two-jet cross-section ratio and of the running of the coupling. The increased statistics will also lead to improvements on the jet energy scale and resolution determination. All of these improvements will in turn contribute to the overall reduction of uncertainty on the strong coupling measurement. NLO calculations of inclusive four-jet cross-sections, soon available, will allow the calculation of the four- to three-jet cross-section ratio, which could also be used to investigate the running of the strong coupling constant. This continued effort to improve our measurement of the strong coupling constant at higher energies is essential to understand and validate the theory QCD at the new energy frontier achieved by the LHC.

Appendix A - Nuisance Parameters in α_S Fit

Table A-1: Nuisance parameters used to obtain the best fit of $\alpha_S(M_Z)$ for each Q' bin, as well as all bins combined.

Q' bin range (GeV)	Fit parameters		
	$s_{trigger}$	$s_{pile-up}$	$s_{jet\ quality}$
100-120	$1.05 \times 10^{-4} \pm 1.00$	$-2.06 \times 10^{-4} \pm 1.00$	$-1.27 \times 10^{-4} \pm 1.00$
120-150	$2.81 \times 10^{-5} \pm 1.00$	$3.03 \times 10^{-5} \pm 1.00$	$6.58 \times 10^{-6} \pm 1.00$
150-180	$-9.38 \times 10^{-5} \pm 1.00$	$-2.44 \times 10^{-5} \pm 1.00$	$-5.72 \times 10^{-7} \pm 1.00$
180-230	$-2.59 \times 10^{-5} \pm 1.00$	$-9.09 \times 10^{-6} \pm 1.00$	$-1.31 \times 10^{-6} \pm 1.00$
230-280	$4.86 \times 10^{-6} \pm 1.00$	$5.97 \times 10^{-7} \pm 1.00$	$3.48 \times 10^{-7} \pm 1.00$
280-330	$-5.49 \times 10^{-6} \pm 1.00$	$-4.70 \times 10^{-5} \pm 1.00$	$-7.67 \times 10^{-6} \pm 1.00$
330-390	$-4.45 \times 10^{-7} \pm 1.41$	$-5.98 \times 10^{-8} \pm 0.79$	$-1.70 \times 10^{-8} \pm 1.41$
390-460	$-4.42 \times 10^{-5} \pm 1.00$	$-3.01 \times 10^{-5} \pm 1.00$	$6.95 \times 10^{-7} \pm 1.00$
460-550	$-7.53 \times 10^{-5} \pm 1.00$	$1.29 \times 10^{-6} \pm 1.00$	$4.74 \times 10^{-7} \pm 1.00$
550-700	$1.16 \times 10^{-5} \pm 1.00$	$6.92 \times 10^{-5} \pm 1.00$	$4.06 \times 10^{-6} \pm 1.00$
700-1000	$2.14 \times 10^{-5} \pm 1.00$	$-2.18 \times 10^{-4} \pm 1.00$	$-8.36 \times 10^{-5} \pm 1.00$
1000-1500	$2.34 \times 10^{-5} \pm 1.00$	$2.86 \times 10^{-5} \pm 1.00$	$-3.41 \times 10^{-6} \pm 1.00$
100-1500	$1.55 \times 10^{-2} \pm 0.98$	$-4.57 \times 10^{-2} \pm 0.99$	$-1.41 \times 10^{-1} \pm 0.98$

Table A–2: Nuisance parameters used to obtain the best fit of $\alpha_S(M_Z)$ for each Q' bin, as well as all bins combined. (continued)

Q' bin range (GeV)	Fit parameters		
	s_{JES}	s_{JER}	$s_{\eta Res.}$
100-120	$1.25 \times 10^{-4} \pm 1.00$	$4.99 \times 10^{-5} \pm 1.00$	$7.44 \times 10^{-5} \pm 1.00$
120-150	$-9.53 \times 10^{-7} \pm 1.00$	$-5.99 \times 10^{-5} \pm 1.00$	$5.63 \times 10^{-5} \pm 1.00$
150-180	$-1.71 \times 10^{-5} \pm 1.00$	$-1.25 \times 10^{-4} \pm 1.00$	$-1.40 \times 10^{-4} \pm 1.00$
180-230	$-1.25 \times 10^{-4} \pm 1.00$	$-5.86 \times 10^{-5} \pm 1.00$	$-2.03 \times 10^{-4} \pm 1.00$
230-280	$3.55 \times 10^{-6} \pm 1.00$	$-5.58 \times 10^{-6} \pm 1.00$	$3.09 \times 10^{-6} \pm 1.00$
280-330	$-3.99 \times 10^{-5} \pm 1.00$	$-5.49 \times 10^{-6} \pm 1.00$	$1.25 \times 10^{-5} \pm 1.00$
330-390	$-1.10 \times 10^{-6} \pm 0.78$	$-1.74 \times 10^{-7} \pm 1.41$	$-2.27 \times 10^{-7} \pm 0.79$
390-460	$1.82 \times 10^{-4} \pm 1.00$	$3.07 \times 10^{-5} \pm 1.00$	$2.37 \times 10^{-4} \pm 1.00$
460-550	$7.48 \times 10^{-6} \pm 1.00$	$1.14 \times 10^{-5} \pm 1.00$	$1.50 \times 10^{-5} \pm 1.00$
550-700	$-1.73 \times 10^{-5} \pm 1.00$	$-1.27 \times 10^{-5} \pm 1.00$	$-1.43 \times 10^{-5} \pm 1.00$
700-1000	$1.24 \times 10^{-4} \pm 1.00$	$3.85 \times 10^{-4} \pm 1.00$	$-3.91 \times 10^{-4} \pm 1.00$
1000-1500	$-2.25 \times 10^{-5} \pm 1.00$	$-1.56 \times 10^{-5} \pm 1.00$	$-6.63 \times 10^{-5} \pm 1.00$
100-1500	$-3.37 \times 10^{-1} \pm 0.69$	$-9.51 \times 10^{-2} \pm 0.81$	$-5.22 \times 10^{-1} \pm 0.81$

Q' bin range (GeV)	Fit parameters		
	$s_{Monte-Carlo\ model}$	s_{PDF}	$s_{non-pert\ model}$
100-120	$-2.22 \times 10^{-4} \pm 1.00$	$5.46 \times 10^{-5} \pm 1.00$	$-8.06 \times 10^{-5} \pm 1.00$
120-150	$-4.02 \times 10^{-5} \pm 1.00$	$-2.95 \times 10^{-5} \pm 1.00$	$-7.57 \times 10^{-7} \pm 1.00$
150-180	$-2.94 \times 10^{-4} \pm 1.00$	$5.92 \times 10^{-5} \pm 1.00$	$4.62 \times 10^{-4} \pm 1.00$
180-230	$-8.68 \times 10^{-5} \pm 1.00$	$1.48 \times 10^{-5} \pm 1.00$	$1.54 \times 10^{-4} \pm 1.00$
230-280	$4.70 \times 10^{-6} \pm 1.00$	$2.84 \times 10^{-5} \pm 1.00$	$6.28 \times 10^{-6} \pm 1.00$
280-330	$1.46 \times 10^{-4} \pm 1.00$	$3.65 \times 10^{-5} \pm 1.00$	$-2.59 \times 10^{-5} \pm 1.00$
330-390	$-8.00 \times 10^{-7} \pm 0.79$	$2.58 \times 10^{-7} \pm 1.41$	$2.47 \times 10^{-6} \pm 0.75$
390-460	$-2.47 \times 10^{-4} \pm 1.00$	$1.83 \times 10^{-4} \pm 1.00$	$8.30 \times 10^{-6} \pm 1.00$
460-550	$1.65 \times 10^{-5} \pm 1.00$	$3.15 \times 10^{-6} \pm 1.00$	$2.33 \times 10^{-5} \pm 1.00$
550-700	$1.51 \times 10^{-5} \pm 1.00$	$1.18 \times 10^{-5} \pm 1.00$	$2.00 \times 10^{-5} \pm 1.00$
700-1000	$2.17 \times 10^{-5} \pm 1.00$	$-9.07 \times 10^{-5} \pm 1.00$	$3.75 \times 10^{-4} \pm 1.00$
1000-1500	$2.35 \times 10^{-4} \pm 1.00$	$1.09 \times 10^{-4} \pm 1.00$	$1.53 \times 10^{-4} \pm 1.00$
100-1500	$1.87 \times 10^{-2} \pm 0.59$	$9.25 \times 10^{-3} \pm 0.99$	$-3.56 \times 10^{-2} \pm 0.71$

REFERENCES

- [1] B. R. Martin and G. Shaw, *Particle Physics*, Second ed. (John Wiley and Sons, 2004).
- [2] The Particle Data Group, *2010 Review of Particle Physics*, *J. Phys. G* **37**, 075021 (2010).
- [3] J. J. Sakurai, *Modern Quantum Mechanics*, Revised ed. (Addison-Wesley Publishing Company, 1994).
- [4] M. Gell-Mann and F. E. Low, *Quantum Electrodynamics at Small Distances*, *Phys. Rev.* **95**, 1300 (1954).
- [5] W. A. Bardeen, A. J. Buras, D. W. Duke, and T. Muta, *Deep-inelastic scattering beyond the leading order in asymptotically free gauge theories*, *Phys. Rev. D* **18**, 3998 (1978).
- [6] D. J. Gross and F. Wilczek, *Ultraviolet Behavior of Non-Abelian Gauge Theories*, *Phys. Rev. Lett.* **30**, 1343 (1973).
- [7] H. D. Politzer, *Reliable Perturbative Results for Strong Interactions?*, *Phys. Rev. Lett.* **30**, 1346 (1973).
- [8] W. E. Caswell, *Asymptotic Behavior of Non-Abelian Gauge Theories to Two-Loop Order*, *Phys. Rev. Lett.* **33**, 244 (1974).
- [9] D. R. T. Jones, *Two-loop diagrams in Yang-Mills theory*, *Nucl. Phys. B* **75**, 531 (1974).
- [10] E. Egorian and O. V. Tarasov, *Two Loop Renormalization Of The QCD In An Arbitrary Gauge*, *Theor. Math. Phys.* **41**, 863 (1979), [*Teor. Mat. fiz.* 41 (1979) 26].
- [11] A. Vogt, *Efficient evolution of unpolarized and polarized parton distributions with QCD-PEGASUS*, *Comput. Phys. Commun.* **170**, 65 (2005).
- [12] S. Bethke, *The 2009 World Average of α_S* , *Eur. Phys. J. C* **64**, 689 (2009).
- [13] The D0 Collaboration, *Determination of the strong coupling constant from the inclusive jet cross section in ppbar collisions at sqrt(s)=1.96 TeV*, *Phys. Rev. D* **80**, 111107 (2009).

- [14] The ZEUS Collaboration, *Jet-radius dependence of inclusive-jet cross sections in deep inelastic scattering at HERA*, Phys. Lett. B **649**, 12 (2007).
- [15] The H1 Collaboration, *Measurement of Inclusive Jet Production in Deep-Inelastic Scattering at High Q^2 and Determination of the Strong Coupling*, Phys. Lett. B **653**, 134 (2007).
- [16] M. E. Peskin and D. V. Schroeder, *An Introduction to Quantum Field Theory* (Westview Press, 1995).
- [17] J. C. Collins, D. E. Soper, and G. Sterman, *Perturbative Quantum Chromodynamics*, Advanced Series on Directions in High Energy Physics Vol. 5 (World Scientific Pub Co Inc, 1989), chap. ‘Factorization of Hard Processes in QCD’.
- [18] The CDF Collaboration, *Measurement of the Strong Coupling Constant from Inclusive Jet Production at the Tevatron $\bar{p}p$ Collider*, Phys. Lett. **88**, 042001 (2002).
- [19] M. Wobisch, *Determination of the Strong Coupling Constant and Multijet Cross Section Ratio Measurements*, Fermilab Report No. FERMILAB-CONF-11-285-E, 2011 (unpublished), arXiv:1106.5132.
- [20] G. Altarelli and G. Parisi, *Asymptotic freedom in parton language*, Nucl. Phys. B **126**, 298 (1977).
- [21] L. R. Evans and P. Bryant, *LHC Machine*, J. Instrum. **3**, S08001. 164 p (2008), This report is an abridged version of the LHC Design Report (CERN-2004-003).
- [22] The ATLAS Collaboration, *ATLAS detector and physics performance: Technical Design Report, 1*, CERN Report No. ATLAS-TDR-014, 1999 (unpublished).
- [23] The ATLAS Collaboration, *ATLAS detector and physics performance: Technical Design Report, 2*, CERN Report No. ATLAS-TDR-015, 1999 (unpublished).
- [24] The ATLAS Collaboration, *The ATLAS Experiment at the CERN Large Hadron Collider*, JINST **3**, S08003 (2008).
- [25] M. Lamont, Lhc beam operations: Past, present and future, in *Proceedings of the Rencontres de Moriond QCD and High Energy Interactions*, 2011.
- [26] J.-L. Caron, Accelerators chain of cern : operating and approved projects, <http://cdsweb.cern.ch/record/43487/>, 2001.

- [27] The ATLAS Collaboration, How atlas detects particles, <http://www.atlas.ch/detector-overview/detects-particles.html>, ATLAS Experiment 2011 CERN.
- [28] The ATLAS Collaboration, *ATLAS inner detector: Technical Design Report, 1*, CERN Report No. ATLAS-TDR-004, 1997 (unpublished).
- [29] The ATLAS Collaboration, *ATLAS inner detector: Technical Design Report, 2*, CERN Report No. ATLAS-TDR-005, 1997 (unpublished).
- [30] The ATLAS Collaboration, *The Expected Performance of the ATLAS Inner Detector*, CERN Report No. ATL-PHYS-PUB-2009-002, 2008 (unpublished).
- [31] C. W. Fabjan and F. Gianotti, *Calorimetry for particle physics*, Rev. Mod. Phys. **75**, 1243 (2003).
- [32] The ATLAS Collaboration, *ATLAS calorimeter performance: Technical Design Report*, CERN Report No. ATLAS-TDR-001, 1996 (unpublished).
- [33] The ATLAS Collaboration, *ATLAS liquid-argon calorimeter: Technical Design Report*, CERN Report No. ATLAS-TDR-002, 1996 (unpublished).
- [34] The ATLAS Collaboration, *ATLAS tile calorimeter: Technical Design Report*, CERN Report No. ATLAS-TDR-003, 1996 (unpublished).
- [35] The ATLAS Collaboration, *The ATLAS Simulation Infrastructure*, Eur. Phys. J. C **70**, 823 (2010).
- [36] S. Agostinelli *et al.*, *Geant4 – a simulation toolkit*, Nucl. Instr. Methods Phys. Res. A **506**, 250 (2003).
- [37] J. Allison *et al.*, *Geant4 Developments and Applications*, IEEE Transactions on Nuclear Science **53**, 270 (2006).
- [38] C. Eck *et al.*, *LHC computing Grid: Technical Design Report*, Report No. CERN-LHCC-2005-024, 2005 (unpublished).
- [39] T. Sjostrand, S. Mrenna, and P. Z. Skands, *PYTHIA 6.4 Physics and Manual*, JHEP **0605**, 026 (2006).
- [40] G. Corcella *et al.*, *HERWIG 6.5: an event generator for Hadron Emission Reactions With Interfering Gluons (including supersymmetric processes)*, JHEP **0101**, 010 (2001).
- [41] G. Corcella *et al.*, *HERWIG 6.5 Release Note*, 2005, arXiv:hep-ph/0210213v2.

- [42] J. M. Butterworth and J. R. Forshaw, *Photoproduction of Multi-Jet Events at HERA - A Monte Carlo Simulation*, J. Phys. G **19**, 1657 (1993).
- [43] J. M. Butterworth, J. R. Forshaw, and M. H. Seymour, *Multiparton Interactions in Photoproduction at HERA*, Z. Phys. C **72**, 637 (1996).
- [44] M. L. Mangano, M. Moretti, F. Piccinini, R. Pittau, and A. Polosa, *ALP-GEN, a generator for hard multiparton processes in hadronic collisions*, JHEP **0307**, 001 (2003).
- [45] T. Sjöstrand, *Jet fragmentation of multiparton configurations in a string framework*, Nucl. Phys. B **248**, 469 (1984).
- [46] T. Sjöstrand and M. van Zijl, *A multiple-interaction model for the event structure in hadron collisions*, Phys. Rev. D **36**, 2019 (1987).
- [47] The ATLAS Collaboration, *Measurement of multi-jet cross sections in proton-proton collisions at a 7 TeV center-of-mass energy*, Eur. Phys. J. C **71**, 1763 (2011).
- [48] Z. Nagy, *Next-to-leading order calculation of three-jet observables in hadron-hadron collision*, Phys. Rev. D **68**, 094002 (2003).
- [49] S. Catani and M. H. Seymour, *A General Algorithm for Calculating Jet Cross Sections in NLO QCD*, Nucl. Phys. B **485**, 291 (1997).
- [50] M. Cacciari, G. P. Salam, and G. Soyez, *FastJet user manual*, CERN Report No. CERN-PH-TH/2011-297, 2011 (unpublished), arXiv:1111.6097.
- [51] The ATLAS Collaboration, *First tuning of HERWIG/JIMMY to ATLAS data*, CERN Report No. ATL-PHYS-PUB-2010-014, 2010 (unpublished).
- [52] CTEQ, J. Pumplin *et al.*, *New generation of parton distributions with uncertainties from global QCD analysis*, JHEP **07**, 012 (2002).
- [53] The ATLAS Collaboration, *Charged particle multiplicities in $p p$ interactions at $\sqrt{s} = 0.9$ and 7 TeV in a diffractive limited phase-space measured with the ATLAS detector at the LHC and new PYTHIA6 tune*, CERN Report No. ATLAS-CONF-2010-031, 2010 (unpublished).
- [54] A. Sherstnev and R. S. Thorne, *Parton Distributions for LO Generators*, Eur. Phys. J. C **55**, 553 (2008).
- [55] A. D. Martin, W. J. Stirling, R. S. Thorne, and G. Watt, *Parton distributions for the LHC*, Eur. Phys. J. C **63**, 189 (2009).
- [56] P. Z. Skands, *Tuning Monte Carlo Generators: The Perugia Tunes*, Phys. Rev. D **82**, 074018 (2010).

- [57] CTEQ, H. L. Lai *et al.*, *Global QCD analysis of parton structure of the nucleon: CTEQ5 parton distributions*, Eur. Phys. J. C **12**, 375 (2000).
- [58] The ATLAS Collaboration, *Performance of primary vertex reconstruction in proton-proton collisions at $\sqrt{s} = 7$ TeV in the ATLAS experiment*, CERN Report No. ATLAS-CONF-2010-069, 2010 (unpublished).
- [59] M. Cacciari, G. P. Salam, and G. Soyez, *The anti- k_t jet clustering algorithm*, JHEP **04**, 063 (2008).
- [60] M. Cacciari and G. P. Salam, *Dispelling the N^3 myth for the k_t jet-finder*, Phys. Lett. B **641**, 57 (2006).
- [61] W. Lampl *et al.*, *Calorimeter Clustering Algorithms: Description and Performance*, CERN Report No. ATL-LARG-PUB-2008-002, 2008 (unpublished).
- [62] The ATLAS Collaboration, *Properties of Jets and Inputs to Jet Reconstruction and Calibration with the ATLAS Detector Using Proton-Proton Collisions at $\sqrt{s} = 7$ TeV*, CERN Report No. ATLAS-CONF-2010-053, 2010 (unpublished).
- [63] K. Perez, G. Romeo, and A. Schwartzman, *Jet energy resolution and reconstruction efficiencies from in-situ techniques with the ATLAS Detector Using Proton-Proton Collisions at a Center of Mass Energy $\sqrt{s} = 7$ TeV*, CERN Report No. ATLAS-CONF-2010-054, 2010 (unpublished).
- [64] The ATLAS Collaboration, *Jet energy measurement with the ATLAS detector in proton-proton collisions at $\sqrt{s} = 7$ TeV in 2010*, CERN Report No. ATLAS-PERF-2011-03-001, 2011 (unpublished).
- [65] The ATLAS Collaboration, *Readiness of the ATLAS liquid argon calorimeter for LHC collisions*, Eur. Phys. J. C **70**, 723 (2010).
- [66] The ATLAS Collaboration, *Readiness of the ATLAS Tile Calorimeter for LHC collisions*, Eur. Phys. J. C **70**, 1193 (2010).
- [67] The ATLAS Collaboration, *Measurement of the $W \rightarrow l\nu$ and $Z/\gamma^* \rightarrow ll$ production cross sections in proton-proton collisions at $\sqrt{s} = 7$ TeV with the ATLAS detector*, JHEP **12**, 1 (2010).
- [68] The ATLAS Collaboration, *Jet energy scale and its systematic uncertainty in proton-proton collisions at $\sqrt{s} = 7$ TeV in ATLAS 2010 data*, CERN Report No. ATLAS-CONF-2011-032, 2011 (unpublished).
- [69] P. M. Stevenson, *Optimized perturbation theory*, Phys. Rev. D **23**, 2916 (1981).

- [70] M. Cacciari, S. Frixione, M. L. Mangano, P. Nason, and G. Ridolfi, *The t - \bar{t} cross-section at 1.8 and 1.96 TeV: a study of the systematics due to parton densities and scale dependence*, JHEP **0404**, 068 (2004).
- [71] A. D. Martin, W. J. Stirling, R. S. Thorne, and G. Watt, *Uncertainties on α_S in global PDF analyses and implications for predicted hadronic cross sections*, Eur. Phys. J. C **64**, 653 (2009).
- [72] H.-L. Lai *et al.*, *Uncertainty induced by QCD coupling in the CTEQ global analysis of parton distributions*, 2010, arXiv:1004.4624.
- [73] M. R. Whalley, D. Bourilkov, and G. R. C., The ‘les houches’ accord pdfs (lhpdf) and lhaglu, Contribution to the HERALHC workshop, 2005, arXiv:hep-ph/0508110.
- [74] W. J. S. J. M. Campbell, J. W. Huston, *Hard Interactions of Quarks and Gluons: a Primer for LHC Physics*, Rept. Prog. Phys. **70**, 89 (2007).
- [75] D. A. Berry, *Statistics: A Bayesian Perspective* (Duxbury Press, 1995).
- [76] J. O. Berger, *Statistical Decision Theory and Bayesian Analysis*, Second ed. (Springer, 1985).
- [77] G. Romeo, A. Schwartzman, R. Piegaia, T. Carli, and R. Teuscher, *Jet Energy Resolution from In-situ Techniques with the ATLAS Detector Using Proton-Proton Collisions at a Center of Mass Energy $\sqrt{s} = 7$ TeV*, CERN Report No. ATL-COM-PHYS-2011-240, 2011 (unpublished).
- [78] The ATLAS Collaboration, *ATLAS liquid-argon calorimeter: Technical Design Report*, Report No. ATLAS-TDR-002, 1996 (unpublished).
- [79] The ATLAS Collaboration, *ATLAS tile calorimeter: Technical Design Report*, Report No. ATLAS-TDR-003, 1996 (unpublished).
- [80] A. Cooper-Sarkar and C. Gwenlan, Experimental determination of parton distributions, in *Proceedings of the HERA and the LHC Workshop Part A*, p. 78, Geneva, 2005, arXiv:hep-ph/0601012.

KEY TO ABBREVIATIONS

ATLAS: A Toroidal LHC ApparatuS

EF: Event Filter (third) level of ATLAS trigger system

EM: Electromagnetic

HLT: High Level Trigger

JES: Jet Energy Scale

L1: Level-1 of ATLAS trigger system

L2: Level-2 of ATLAS trigger system

LHC: Large Hadron Collider

LO: Leading Order

NLO: Next-to-Leading Order

PDF: Parton Distribution Function

pQCD: Perturbative Quantum Chromodynamics

QCD: Quantum Chromodynamics

RGE: Renormalization Group Equation